**The Dissertation Committee for German Diego Merletti Certifies that this is the approved version of the following dissertation:**

# Stratigraphy, Sedimentology and Petrophysics of Transgressive Tight Gas Sandstones, Almond Formation, Wyoming

**Committee:**

Ronald J. Steel, Supervisor

Carlos Torres-Verdin, Co-Supervisor

William L. Fisher

Cornel Olariu

Richard A. Ketcham

Jesse J. Melick

# Stratigraphy, Sedimentology and Petrophysics of Transgressive Tight Gas Sandstones, Almond Formation, Wyoming

**by**

**German Diego Merletti**

**Dissertation**

Presented to the Faculty of the Graduate School of

The University of Texas at Austin

in Partial Fulfillment

of the Requirements

for the Degree of

**Doctor of Philosophy**

**The University of Texas at Austin**

**August, 2017**

# Dedication

To my wife Maria Marta and sons, Matteo and Lucas, who patiently tolerated my many moods the last years; to my mothers Mercedes and Aurora, my father Jorge, and my brothers Adrian and Martin.

# Acknowledgements

I would like to express my sincerest gratitude to Drs. Ron Steel and Carlos Torres-Verdin for their technical instruction and constant advice while supervising my research.

My deepest thanks to Drs. Jesse J. Melick and Cornel Olariu for their continuous support and guidance over the last year. I also thank to my Masters of Science supervisor, Bill Fisher, and Professor Richard A. Ketcham for their critical view on this dissertation.

My gratitude extends to BP and its onshore business L48 for providing the data set used in my research and for funding my studies. Special thanks to BP managers, Jeff Lelek, Peter Evans, Phil Smith, Kjetil Jansen and Andy Cunningham, who supported my research over the last six years. I also thank BP Technical Advisors, Dave Spain and Jeff Hamman, for their honest and continuous advice in the field of Petrophysics.

Finally I am most thankful to my parents Mercedes and Jorge who taught me through their example to be honest, persevere and work hard to achieve my goals in life.

# Stratigraphy, Sedimentology and Petrophysics of Transgressive Tight Gas Sandstones, Almond Formation, Wyoming

German Diego Merletti, Ph.D.
The University of Texas at Austin, 2017

Supervisor: Ronald J. Steel
Co-Supervisor: Carlos Torres-Verdin

With the recent increase in development of unconventional reservoirs, the ability to predict rock quality from sedimentary and petrophysical models has become paramount to the development of tight gas sandstones. In this way, a refined understanding of the primary sedimentary, stratigraphic and diagenetic controls on rock quality permits more reliable hydrocarbon distribution prediction and more economical drilling programs.

The Almond Formation in southwest Wyoming is characterized by three depositional facies associations (DFA); shoreface, delta and fluvial/coastal plain, which present three distinctive porosity-permeability trends. Differences between petrophysical facies are primarily driven by diagenetic (cementation and grain dissolution) effects on different framework grain compositions. Depositional textural variation, such as grain size and sorting is minimal in all DFAs.

This research focuses on building an understanding of the transgressive deposits by studying the variability of sandbody types, comparing and contrasting their reservoir architecture in a setting with a well-documented back-stepping stacking pattern. Construction of a high-resolution chronostratigraphic framework, in 1,450 wells over 6,200 km$^2$, revealed the evolution of fundamental fine-scale architectural elements.

Detailed analysis and integration of cores and well logs along a spectrum of sandbodies document stratigraphic evolution from longshore accretion to seaward progradation associated with progressively increased infill of a shrinking lagoon. End members sandstone geometries include: 1) narrow, finger-like sandstone morphologies with well-developed lagoonal facies and; 2) broad, strandplain-type sandbodies with coastal plain-dominated back-barrier.

This research also addresses a problematic aspect of tight gas reservoirs: the prediction of rock-quality-dependent water saturation (SW) models with depth. Primary drainage and imbibition saturation-height models (SHM) were developed from special core analysis and integrated with porosity and permeability logs to verify the SW state of reservoirs. Assuming that reservoirs were fully charged with hydrocarbons, the drainage SHM is key for flagging departures from the expected rock-quality-dependent water saturation. Observations in tens of wells show that the reference resistivity-derived saturation can be predominantly fitted by primary drainage SHM. However, some upper Almond shoreface bars that have anomalously high SW can be fitted with primary imbibition saturation functions. These fitting exercises indicate that some Upper Almond reservoirs imbibed due to trap tilting or leaking through outcrops.

# Table of Contents

# List of Tables

# List of Figures

# CHAPTER 1 INTRODUCTON

## 1.1 PROBLEM AND SIGNIFICANCE

Transgressive deposits are commonly thin because of the rapid landward migration that transgressive shorelines make over low-lying coastal plains. In a number of well-documented cases, however, transgressive sands can reach up to a few tens of meters in thickness (Tye at al., 1993; Steel et al., 2000). The variability of transgressive deposits is large due to the numerous factors influencing the shoreline retrogradation (Heward, 1981). These factors, which include the rate of transgression and coastal morphology, yield different types of sand bodies over relatively short distances within the same sedimentary basin. Subtle changes in one or a combination of the controlling factors can substantially modify the characteristics of transgressive deposits (Cattaneo and Steel, 2002).

Several models have been proposed to explain the stratigraphic response to transgression, of which continuous and punctuated transgressions represent end members. Continuous landward migration of the shoreline during sea-level rise leads to barrier shoreface retreat, whereas punctuated transgressions occur by alternation of coastal retrogradation and short progradational (regression) shoreline transits despite the overall landward-stepping of the shoreline.

The Campannian-Maastrichian Almond Formation represents latest-stage Western Interior Seaway sediments deposited in fluvial, coastal plain and shallow marine depositional environments (Roehler, 1990). The Formation is commonly divided into three members, the lower, the middle and the upper Almond (Banfield, 2007; Tobin et al, 2010). The "lower Almond" was deposited in an east-to-west transgressive regime and its deposits exhibit common characteristics of backstepping shorelines. The "middle Almond" displays typical features of regressive deposits with thicker strandplains formed in the coast sections between wave-dominated deltas. However, the "upper Almond" poses a problem because it does not resemble the most commonly documented transgressive deposits. Some of its sandstones, which exhibit a wide range of variation in all petrophysical properties, can reach up to few tens of meters in thickness and have a regressive character.

Some current interpretations of the Upper Almond reservoir sandstone bodies have been that the Almond transgression generated exclusively barrier island complexes (Jacka, 1965; Roehler, 1988), whereas others interpret them as mostly regressive shoreface bodies (e.g., Hendricks, 1994; Kieft et al, 2011). The majority of these interpretations are made on the basis of either Rock Springs outcrops or specific reservoirs in the subsurface of Washakie and Great Divide basins (i.e., Lawrence, 2007). The upper Almond sandbodies have not yet been characterized in a sub-regional basis in a context of varying accommodation (subsidence and eustatic sea-level rise) and sediment supply.

The Almond sandstones display a complex pore and pore-throat geometry where a single porosity value can lead to four orders of magnitude permeability. The derivation of permeability from well logs remains a challenge in uncored wells because commonly acquired logs only respond to porosity, relative fluid volume, and lithology. Some authors interpret such a variation in rock quality either based on petrophysics (i.e., Lieber and Miller, 2009) or the petrographic studies (i.e., Tobin et al., 2010); however, there is no rigorous analysis of depositional facies and petrographic information in porosity-permeability space.

Another problematic aspect of tight gas reservoirs is the prediction of reliable rock quality-dependent water saturation (SW) models with depth. These models are commonly well-constrained in conventional reservoirs for simple drainage conditions, but when reservoirs are tight and imbibition or more complex re-drainage and re-imbibition occur, the concept of a current Free Water Level (FWL) as a datum from which saturations can be predicted is lost. Understanding of the primary sedimentary, stratigraphic and diagenetic controls on rock quality permits more reliable hydrocarbon distribution prediction and more economical drilling programs in unconventional reservoirs.

## 1.2 OBJECTIVES

The objectives of this research are:

- Improve knowledge of transgressive deposits by documenting the variability of sandbody types, comparing and contrasting their reservoir architecture and evaluating the mechanisms that control the architecture.
- Test the hypothesis that Almond reservoirs were deposited during a long-term punctuated transgression (i.e., transgression with intermittent regressions) which generated three possible types of sandbody, namely (1) sub-ravinement shorefaces that were sheetlike and as extensive as the prior shoreface progradation, (2) isolate (drowned in place) or ravinement-tip barrier bars at the T-R turnaround, both of which would generate narrow and elongated sandbodies parallel with the prior shoreline, and (3) supra-ravinement tidal sand ridges that were also narrow and elongate but with more variable orientation.
- Understand the linkages between grain mineralogy, and diagenetic (cementation and grain dissolution) and sedimentary processes (grain size and sorting) enhance predictions on reservoir quality across the Almond Formation. Corroborate the robustness of permeability models against dynamic data (i.e., production logs and initial production indices).

- Develop rock quality-dependent drainage and imbibition saturation-height models from special core analysis having resistivity-derived water saturation model as reference. Similarities and discrepancies between alternative models will help understanding the water saturation state of reservoirs.

## 1.3 METHODOLOGY

The backbone of the methodology is the construction of a high-resolution chronostratigraphic framework using 1,450 representative wells over an area of 6,600 km$^2$, within a time framework of ammonite zones calibrated to absolute dates. This level of detail permits evaluating the evolution of the Wamsutter embayment and the sandbody morphology changes during the terminal transgression of the late Campanian - early Maastrichtian period. Each well has a petrophysical and facies model calibrated to conventional rock core data.

The characterization of depositional facies associations (DFA) was performed in three conventional cores that cover the entire Almond Formation. Three additional cores in specific upper Almond sandbodies were described and sedimentary observations tied to sandbody morphology. The understanding of rock frame mineralogy and diagenetic processes is interpreted from thin-section petrographic observations in six cored wells. The analysis of textural features (grain size and sorting) and diagenetic overprint (grain dissolution, primary vs. secondary porosity, etc.) provides valuable clues on the determination of rock quality drivers.

The construction of saturation-height models required the acquisition of a comprehensive special core analysis program designed to characterize each of the DFA. The program included ambient high-pressure mercury injection and centrifuge capillary pressure, stressed multi-cycle mercury injection and extrusion, and determination of maximum trapped gas. A robust resistivity-derived water saturation model is used as a reference for saturation-height modelling. The match or discrepancy between alternative drainage and imbibition models against the reference model will help understanding the water saturation state of various Almond reservoirs.

## 1.4 OVERVIEW OF CHAPTERS

### 1.4.1 Chapter 2

This chapter describes the conventional and special core analysis used as "ground truth" in the log-derived petrophysical evaluation of 1,450 wells. Reservoir-quality Almond rocks have a relative low clay content (<10%) and total porosity varying between 8 and 16%. Absolute permeability at reservoirs conditions ranges between 0.0001 and 1 mD and total water saturation, in reservoirs above the fluids transition zone, varies between 15 and 40%.

Four petrophysical rock types are defined at (cored) discrete depths and extrapolated to uncored intervals making use of deterministic and stochastic approaches. These continuous rock type models allow the derivation of two alternative absolute permeability models. These models are converted to gas effective permeability and integrated over depth in order to compare them to individual post-hydraulic fracture reservoir performance from production logs.

### 1.4.2 Chapter 3

Chapter 3 is a manuscript already published (Merletti et al., 2017). It addresses the integration of depositional, diagenetical and petrophysical facies to derive a third absolute permeability model. The Almond Formation is characterized by three depositional facies associations; shoreface, deltaic and fluvial/coastal plain, which present three distinctive porosity-permeability (Ø-K) trends. Textural features resulting from depositional processes, such as grain size and sorting, vary little between facies associations. However, diagenetic (cementation and grain dissolution) effects on different framework grain compositions are the main drivers for different Ø-K trends. Since depositional and diagenetic controls are related to each other, one can interpret depositional facies from log pattern recognition and apply specific trends to reduce the uncertainty in absolute permeability prediction.

The three permeability models are challenged to predict post-hydraulic fracture initial reservoir performance in 44 wells. This validation exercise, informally called static-to-dynamic calibration, is absolute necessary to determine the most robust permeability model for saturation-height modelling (chapter 4).

### 1.4.3 Chapter 4

Chapter 4 is another manuscript already published (Merletti et al., 2016). It discusses a problematic aspect of tight gas sandstones: the prediction of rock quality-dependent water saturation models vs. depth. Many authors (i.e., Spain et al., 2013) believe that these models don't work in tight sandstones because many of these rocks went through complex saturation histories (drainage, imbibition, re-drainage, re-imbibition, etc.) and the concept of common free-water level is lost.

In some aspects, such as "same structural configuration since reservoir charge" and "strong stratigraphic component of trap", the Almond formation resembles conventional reservoirs. This encouraged me to derive primary drainage and imbibition water saturation vs. depth functions from special core analysis. The comparison between these functions and the resistivity-derived water saturation model (reference) provides some clues on the saturation state of different reservoirs.

This comparison exercise shows that the majority of the Almond can be fitted with primary drainage model with variable free-water level and some Upper Almond bars went through imbibition at some point in their burial history.

### 1.4.4 Chapter 5

This chapter describes the high-resolution chronostratigraphic model of the Upper Almond using 1,450 wells in southwest Wyoming. The mapping of individual sandstone bodies allowed evaluating the evolution of the Wamsutter embayment during the long-term transgression of the late Campanian - early Maastrichtian period.

The stratigraphic correlation and sandstone mapping allowed the definition of the fundamental genetic unit: the barrier spit unit (BSU). The BSU is a 6 to 12 meters thick, elongated, southward narrowing sandbody generated by the accretion long-shore drift-sourced reworked sediments. BSUs change their morphology and facies associations as the shoreline migrates westward into the embayment.  Sandstone morphology along with the description of conventional cores allowed the interpretation of the most likely transgression mechanism operating in Upper Almond times.

# CHAPTER 2 PETROPHYSICAL ANALYSIS

## 2.1 ABSTRACT

Tight-gas rock core measurements and log petrophysical evaluation are challenging due to the reduced pore space and complex pore to pore throat morphologies of reservoirs. Extensive routine and special core analysis was performed in three whole rock cores that cover the entire Almond thickness. These lab measurements are considered “ground truth” for the log-derived petrophysical evaluation. A set of 1,300 wells was selected over an area of 6,600 $Km^2$ to construct a petrophysical model that characterizes a wide range of reservoir qualities.

Almond reservoirs are tight sandstones interbedded with shales and coals. Tight gas reservoir is a term commonly used to refer to natural gas locked in low-permeability (i.e., less than 0.1 mD) reservoirs. Reservoir-quality sandstones are relatively clean (clay-free) and the total clay content can be as high as 10%. Clay types include kaolinite, mixed layer illite-mica and illite-smectite. Total porosity at reservoir conditions varies between 1 and 16% and absolute permeability between 0.0001 to 1 mD. Reservoirs above the fluids transition zone exhibit water saturation values between 15 and 40%.

Four petrophysics rock types were defined in capillary pressure space and extrapolated to wireline logs using stochastic and deterministic approaches. Such models provide equations to derive absolute permeability from rock types and total porosity. Absolute permeability models were converted to effective permeability using rock type-dependent relative permeability functions which fit experimental data.

The robustness of the core calibrated, log-derived petrophysical model was validated by comparing the (static) gas effective permeability model against production logs. The largest zonal contribution in the production log coincides with the reservoirs exhibiting the largest gas permeability thickness. This type of static-to-dynamic

comparison is a must-do exercise before more sophisticated modelling, such as saturation-height modelling, is planned and executed.

## 2.2 INTRODUCTION

Petrophysics of tight sandstone is complex, owing in part to their low overall pore volume and complex pore geometry (Rushing et al., 2008). Permeability (less than 10 uD) is often dominated by slot-like pore throats that connect the larger primary and secondary pore bodies. The slot-like pores make permeability particularly sensitive to stress (Miller and Shanley, 2010).

Many of these unconventional reservoirs display a large variability of rock quality in rock core measurements taken at inch-scale core plugs. Measurements in plugs are commonly used to calibrate foot-scale wireline log measurements. Differences in scales can make the core-to-log calibration a challenging exercise with imprecise petrophysical model prediction.

In order to mitigate these challenges, lab measurements are taken in closely spaced plugging depths targeting the entire spectrum of rock qualities (i.e., 0.0001 to 10 mD permeability). An effective core-to-log calibration is the one where sources of inconsistencies have been understood and minimized as much as possible.

In this study, the log-derived petrophysical evaluation was ground-truthed in the special and routine core analysis obtained in three conventional cores of Almond reservoirs. The Almond Formation is approximately 500 feet of gross reservoir thickness, and the average net-to-gross ration is 20% (Tobin et al. 2010). The core-calibrated, log-derived (static) petrophysical model built in cored wells was compared to (dynamic) production log data before its implementation in hundreds of uncored wells as a further calibration to the reservoir.

## 2.3 DATABASE

The Wamsutter field is located in the southwest corner of Wyoming State in the United States (Figure 2.1). Out of the 8,500 densely spaced vertical wells drilled in the Wamsutter field over the last 50 years, this study incorporates a subset of 1,300 representative wells selected for petrophysical analysis. An additional set of 150 wells was selected in West Desert Springs, Desert Springs and Patrick Draw fields for correlating the Wamsutter field with the Rock Springs Uplift outcrops.

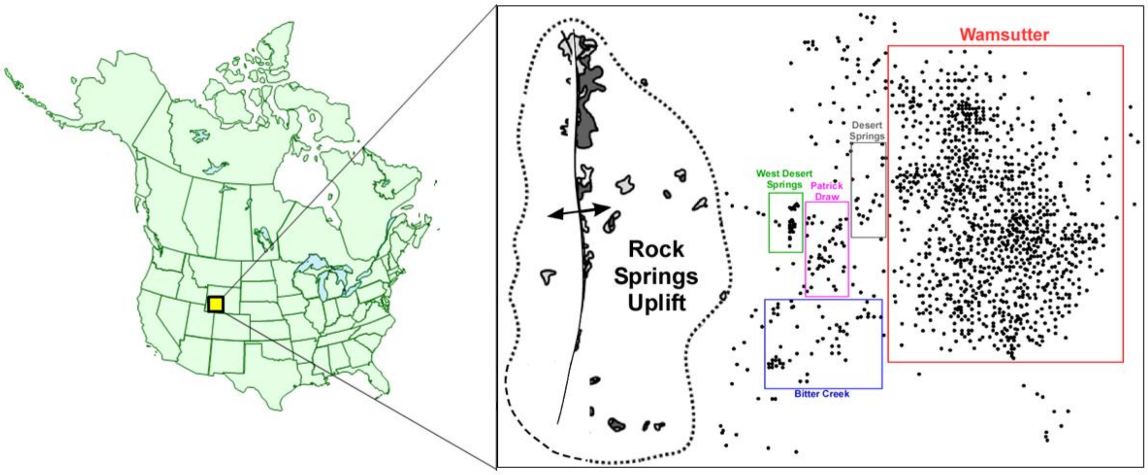

Figure 2.1: Location of the Wamsutter Field and selected wells for the petrophysical evaluation.

The wells selected for this study have acquired caliper (CALI), gamma ray (GR), shallow and deep resistivity (RSHALLOW and RDEEP), neutron porosity (NPHI) and bulk density (RHOB) logs. Figure 2.2 shows these logs in the first three tracks. There are dozens of whole cores that recovered several tens of feet of Almond interval in the 70s and 80s. As expected, available core measurements in such cores were taken using 40-year old technology. Over the last 10-15 years, a new generation of lab equipment arrived and yields more accurate petrophysical measurements. One example is the replacement of nitrogen by helium as a standard gas for porosity measurements. Helium has a smaller molecule size than nitrogen so it can access tighter pore structures; therefore, helium porosity can be larger than the one reported by equipment using nitrogen.

Three conventional cores, covering almost the entire Almond interval, were analyzed with routine and special core analyses within the last 10 years. This provides confidence that all the reported lab equipment delivered results with the same degree of accuracy. Results in these three cores are utilized as the "ground truth" for the log-derived petrophysical interpretation. Lab measurements include helium porosity, grain density, pulsed-decay absolute permeability at ambient and in-situ confining stress, Dean-Stark water saturation (Dean and Stark, 1920), X-Ray diffraction, Stationary-Liquid gas relative permeability.

## 2.4 PETROPHYSICAL PROPERTIES

### 2.4.1 Shale Concentration

Two alternative approaches were tested when computing the shale concentration (Csh) from wireline logs. The first method is called "density-neutron crossplot" and is based on the separation between these two porosity logs with a specific track range; the larger the difference, the bigger the shale concentration. The analytical solution of this approach states that:

$$m_1 = \frac{(X_w - X_o)}{(RHO_{fl} - RHO_{ss})}$$

$$X_1 = NPHI + m_1 \times (RHO_{ss} - RHOB)$$

$$X_2 = X_{sh} + m_1 \times (RHO_{ss} - RHO_{sh})$$

$$C_{sh} = \frac{(X_1 - X_o)}{(X_2 - X_o)}$$

where Xo is the neutron matrix density, Xsh is the neutron reading in shales, Xw is neutron reading in water, RHOsh is the matrix density in shales, RHOss is the matrix density in sands and RHOfl is the fluid density.

The second approach uses linear and nonlinear Csh estimators from the GR log. This approach requires determining the baseline GR response at the depth of interest and determining the response associated with a clean reservoir having no shale (GRcl) and a zone of 100% shale (GRsh). The linear method is the simplest, but it tends to overestimate shale in the intermediate ranges of shale concentration. The linear response is called Index Gamma Ray (IGR) and states that:

$$IGR = \frac{(GR_{sh} - GR)}{(GR_{sh} - GR_{cl})}$$

The nonlinear method begins by estimating the Csh from the linear equation and then correcting that estimation using different correction factors. The largest correction is applied by the Larionov model for Tertiary rocks whereas the smallest correction is applied by the Larionov model for Older rocks (Larionov, 1969). Since the Almond is Upper Cretaceous age, the Clavier model is a good compromise between the Tertiary and older rocks models (Clavier et al., 1977). This model states that:

$$C_{sh} = 1.7 - [3.38 - (IGR + 0.7)^2]^{0.5}$$

The both approaches listed above have pros and cons. The GR methods are preferred in the majority of cases for their simplicity. However, the feldspar content of Upper Almond sands can lead to artificially higher GR readings and therefore higher Csh values. The crossplot approach assumes that the neutron porosity to density porosity difference has a linear response with rock clay content. If reservoirs contain gas, such difference is not a reliable indication of Csh.

Neutron logs display a variable distribution of responses, even in lithologies used as references for normalization. The variability of neutron responses by vendor type, tool generation and perhaps log environmental corrections was another factor considered in the selection of the Csh model. The majority of NPHI logs older than 15 years required log normalization. Such normalization is implicit in GR-derived Csh logs because the IGR is linearly scaled between GRcl and GRsh values. Therefore, the Clavier model is selected as the preferred model for computing Csh. Figure 2.2 displays in track 4 the Csh model calibrated to XRD-derived total clay content. The reported XRD total clay includes around 50 % kaolinite and Illite-mica and 50% of mixed-layer illite-smectite. The percentage of expandable clay in the mixed-layer is less than 15%.

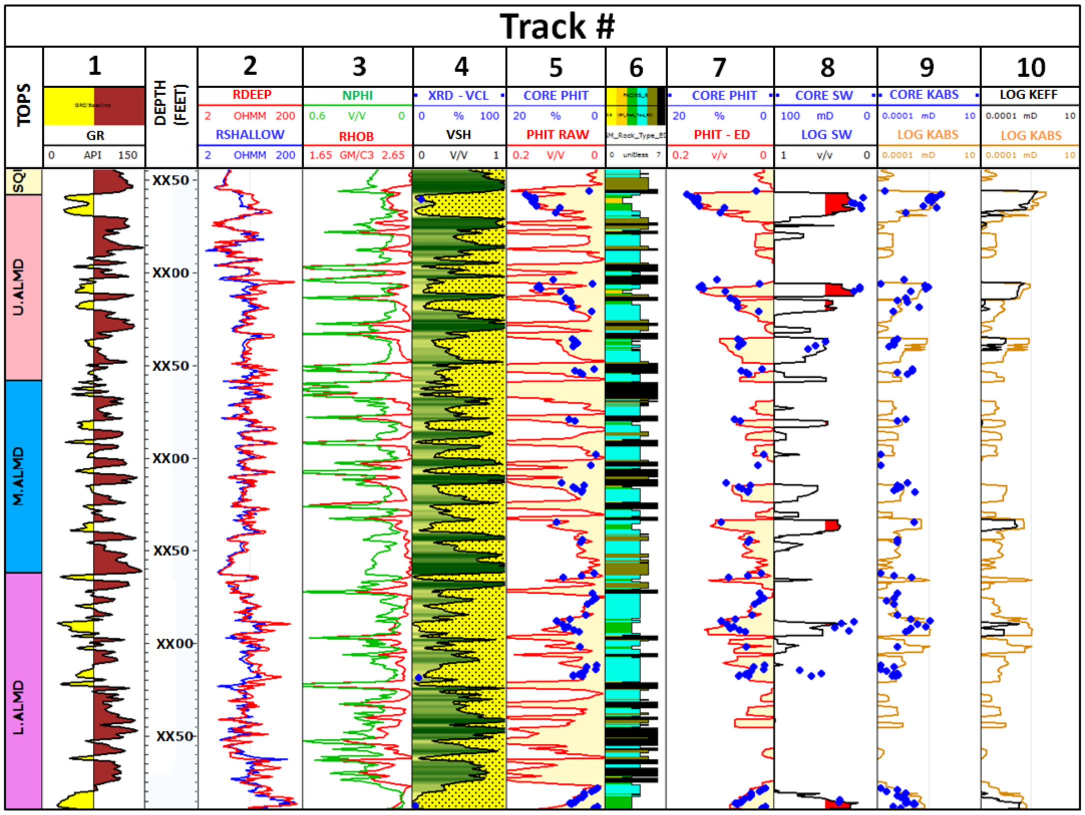

Figure 2.2: Basic well logs (1: Gamma Ray, 2: Resistivities, 3: Neutron Porosity and Bulk Density) and petrophysical logs calibrated to core data (4: Shale Concentration, 5: Raw Total Porosity, 6: Rock Type, 7: Edited Total Porosity, 8: Water Saturation, 9: Absolute Permeability and 10: Absolute and Effective Permeability).

### 2.4.2 Total porosity

Having discarded the NPHI log for quantitative evaluation, the total porosity (PHIT) is determined directly from the RHOB log. The interpretation model is:

$$RHOB = PHIT \times RHO_{fl} + (1 - PHIT) \times RHO_{ma}$$

where RHO_fl and RHO_ma are densities of fluid and rock matrix respectively. Solved for porosity, this yields:

$$PHIT = \frac{(RHO_{ma} - RHOB)}{(RHO_{ma} - RHO_{fl})}$$

This porosity is considered a total porosity because it draws no distinction between pore fluid and fluid possibly bound in shales. The rock matrix density RHO_ma is obtained by analysing the distribution of available core measurements. This distribution has mean and standard deviation values of 2.682 and 0.015 g/cc respectively. Considering the mean as a representative RHO_ma value, the RHO_fl is interactively changed in 0.05 g/cc steps until the modelled and the (measured) core porosity difference is minimized. Figure 2.3 summarizes this optimization process for three wells. Notice that the smallest difference with core porosity is achieved when RHO_fl ranges between 0.8 and 0.9 g/cc. These values are consistent with the water-based mud filtrate process on tight gas reservoirs. Depending on the rock quality, the mud invasion does not sweep variable amounts of residual gas in the flushed zone. Residual gas saturation for Almond rocks ranges between 15 and 40%..

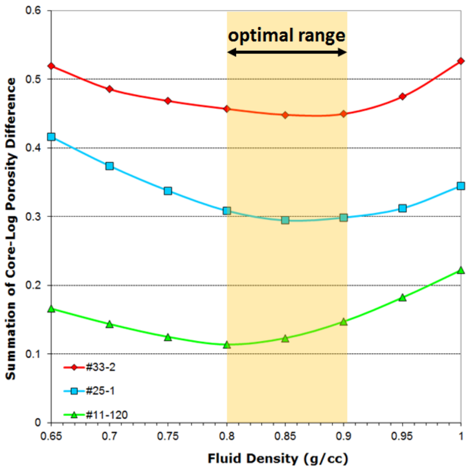

Figure 2.3: Optimization of fluid density for total density porosity estimation.

Figure 2.2 displays in track 3 the effect that coal layers produce on porosity logs; this is pronounced RHOB and NPHI spikes toward low and high values respectively. Coal, by its chemical composition, has one of the highest hydrogen index values of common minerals encountered in sedimentary deposits. Thus, the NPHI log reads a very highly apparent porosity in coals.

Most coals have low density values (about 1 to 1.8 g/cc) due to their composition which includes kerogen with varying carbon, oxygen and hydrogen content. When the RHOB log is combined with RHOma and RHOfl values derived for sandstones, the resulting PHIT log displays high total porosity values which exceed 20% (Figure 2.2, track 5). This artifact is fixed by 1) flagging coaly beds using both NPHI and RHOB logs; and 2) applying a very low PHIT values in such flagged intervals. Threshold values for flagging coals were obtained in three cored wells; they are 2.0g/cc and 0.43v/v for RHOB and NPHI respectively. Figure 2.2, track 7 shows the total porosity log with no coal effect. This log is used for further computations of water saturation and absolute permeability.

### 2.4.3 Total Water Saturation

The Archie's model (1957) is used for computing water saturation in an uninvaded formation next to the borehole. The Archie equation can be expressed as follows:

$$S_w{}^n = \frac{R_w}{(PHIT^m \times R_t)}$$

where Sw is water saturation, n is the saturation exponent, Rw is the connate water resistivity at formation temperature, PHIT is total porosity, m is cementation exponent and Rt is the true resistivity of the formation.

Electrical properties, namely m and n, were measured in plugs using 50,000 ppm NaCl brine at confining stresses representative of reservoirs. Rather than using constant values, the cementation and saturation exponents were plotted against PHIT to find suitable correlations. The cementation exponent, for Almond porosities, ranges between 1.85 and 2.05, whereas the saturation exponent varies between 1.30 and 1.55.

The resistivity of connate water was measured in samples of produced formation water. Wells producing either from the Upper or the Lower Almond were considered for this analysis; in other words, wells with comingled production were excluded from the water sampling. The salinity profile displays 38,000 ppm of equivalent NaCl for Upper Almond and 8,000 ppm for Lower Almond. Such salinities are equivalent to 0.20 ohm.m and 0.70 ohm.m at 68°F respectively. In general, nonmarine facies produce fresher, more bicarbonate-rich water and saline chloride-dominated waters that characterize marine facies, reflecting more extensively the original depositional environment of the water (Smith, 1998). Figure 2.2 track 8 displays the final water saturation log model along with a few direct measurements of water recovered from core plugs by Dean-Stark distillation extraction.

### 2.4.4 Petrophysical Rock Types

#### *2.4.4.1 Definition of rock types in core data*

Rock types are used in this study to define rock intervals with similar flow characteristics, related to pore throat size or hydraulic radius. Rock types are commonly defined through laboratory core plug measurements of porosity, permeability and capillary pressure.

Several authors published regression-based, experimental models that relate effective pore throat radius (PTR), total porosity, and absolute permeability to air (Pittman, 1992; Gunter at al., 1997; 2014). Winland (1976) developed a general equation based on a mixture of carbonate and siliciclastic core measurements, pore geometry descriptions and over 300 mercury injection samples (Gunter et al., 2014). They found that the best correlation among variables was obtained when the pore throat radius is computed at 35% mercury saturation. Winland's equation states that:

$$R_{35} = 10^{\left(0.732+0.588\times log(K)-0.864\times log(\emptyset)\right)}$$

where R35 is the PTR predicted at 35% mercury saturation, K is absolute permeability and Ø is total porosity.

Pittman (1992) expanded Winland's approach and reported correlations from 10% to 75% mercury saturation at five percent increments. The Pittman's models evaluated in this study predict PTR at 35%, 45% and 55% mercury saturation; these are:

$$R_{35} = 10^{\left(0.255+0.565\times log(K)-0.523\times log(\emptyset)\right)}$$

$$R_{45} = 10^{\left(0.609+0.608\times log(K)-0.974\times log(\emptyset)\right)}$$

$$R_{55} = 10^{\left(0.948+0.632\times log(K)-1.426\times log(\emptyset)\right)}$$

The rock typing starts by interpreting mercury injection capillary pressure (MICP) tests and their associated porosity and permeability values. The first analysis included the derivation of pore throat radii and their analysis in frequency plots for obtaining the dominant PTR per sample. Figure 2.4 displays a MICP tests in the left-hand side and a PTR distribution in the right-hand side; the mean value of the peak is taken as the "measured dominant PTR" value.

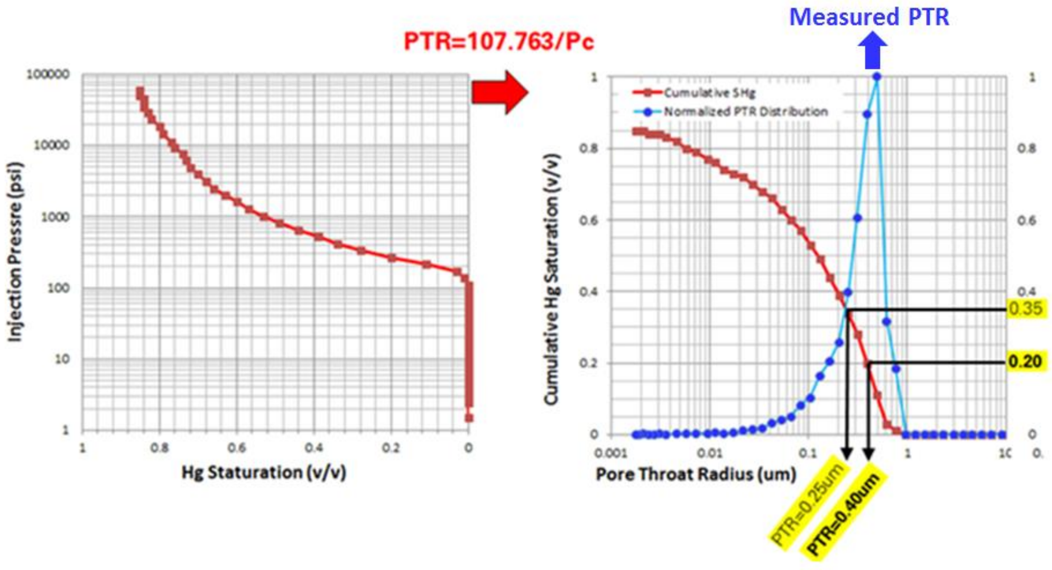

Figure 2.4: Interpretation of measured dominant pore-throat radius (PTR) from a mercury injection test.

Measured PTR are compared to the predicted PTR from alternative regression-based models. Figure 2.5 shows cross plots between measured (x-axis) and predicted (y-axis) dominant PTR for the Almond Formation. Values predicted by the Winland R-35 equation lay close to the 45° slope line, indicating that this model is the best predictor of PTR for this reservoir.

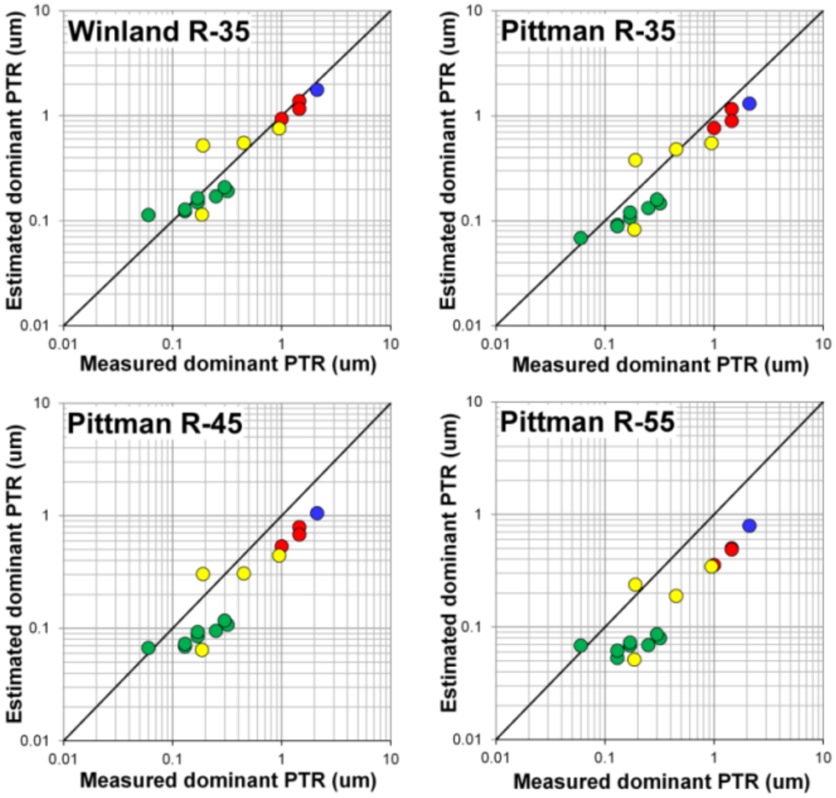

Figure 2.5: Measured vs. predicted pore throat radius (PTR) by alternative regression-based models. Colors represent samples from different wells.

Once the rock type model is defined, the Winland plot (Kolodzie, 1980; Gunter et al., 1997) was used for identifying a discrete number of rock types in mercury injection capillary pressure (MICP) samples. Figure 2.6 (left plot) shows the four rock types in Almond samples, for which boundaries are picked at PTR of 0.45, 0.15 and 0.045 microns. These boundaries were interactively moved until tests, in capillary pressure and mercury saturation space, were properly grouped by similar equivalent entry pressure, irreducible water saturation and geometric factor (Figure 2.7, right plot).

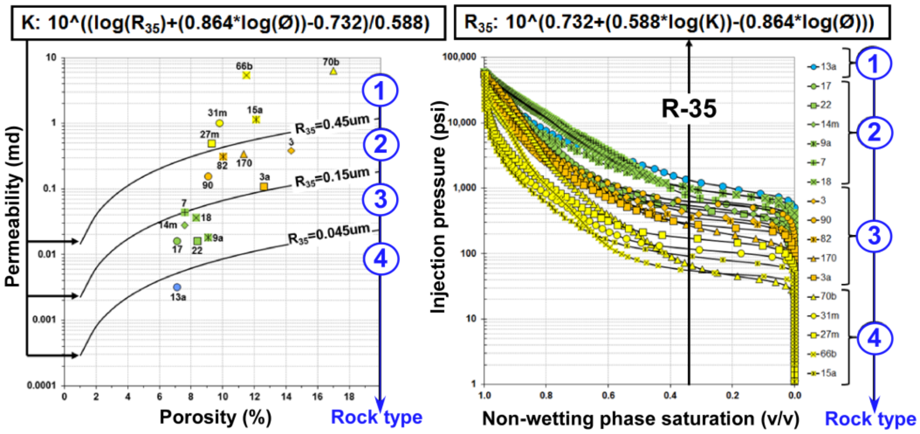

Figure 2.6: Definition of rock types in porosity vs. permeability (left) and non-wetting phase saturation vs. injection pressure (right) space. Rock types 1, 2, 3 and 4 are represented by samples colored in yellow, orange, green and blue respectively.

Once the rock type boundaries were defined, equations allowed the prediction of PTR (R35) from samples with only routine core analysis tests, namely porosity and absolute permeability.

### *2.4.4.2 Rock types in log data*

Once the petrophysical rock types are defined at depths where mercury injection capillary pressure and stress-corrected routine core analysis measurements are available, well logs are calibrated to this and used to extrapolate the rock types throughout uncored intervals. Algorithms for finding correlations between rock types and corresponding well log values are based on stochastic and deterministic principles. In this study, stochastic techniques include: 1) the use of a Multilayer Perception (MLP) technology to train artificial neural networks; and 2) deterministic approaches implementing Multi Correspondence Analysis (MCA) to find regressions between input and output logs. Figure 2.7 displays input logs; the target is the core-derived rock type model (discrete) and the result which is a continuous rock type log.

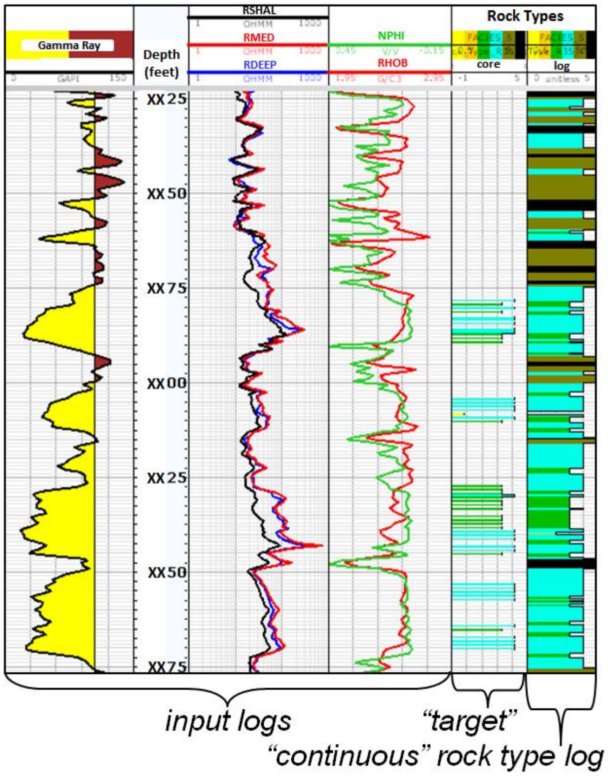

Figure 2.7: Input logs utilized to derive a continuous rock type log for uncored wells.

The match between core- and log-derived rock types is imperfect in cored depths (Figure 2.2). One factor influencing that match is the resolution of the measurements. Lab measurements are performed at inch-scale core plugs whereas logging tools record reservoir properties at foot-scale. Poor correlation of core and well-log based rock types adds uncertainty to the permeability prediction, which is the parameter serving as link between the static reservoir description and the dynamic measurements, such as well tests.

### 2.4.5 PERMEABILITY

#### *2.4.5.1 Absolute Permeability*

The R35 values for each rock type can be averaged in a single value; this allows the absolute permeability to be derived from total porosity and a discrete rock type model as follows:

$$K(rock\ type\ 1) = 10^{((log(0.75)+0.864\times log(PHIT)-0.732)/0.588)}$$

$$K(rock\ type\ 2) = 10^{((log(0.25)+0.864\times log(PHIT)-0.732)/0.588)}$$

$$K(rock\ type\ 3) = 10^{((log(0.08)+0.864\times log(PHIT)-0.732)/0.588)}$$

$$K(rock\ type\ 4) = 10^{((log(0.023)+0.864\times log(PHIT)-0.732)/0.588)}$$

Figure 2.8 is a graphical representation of this approach; continuous black lines represent rock type boundaries and dashed grey lines correspond to the above permeability models.

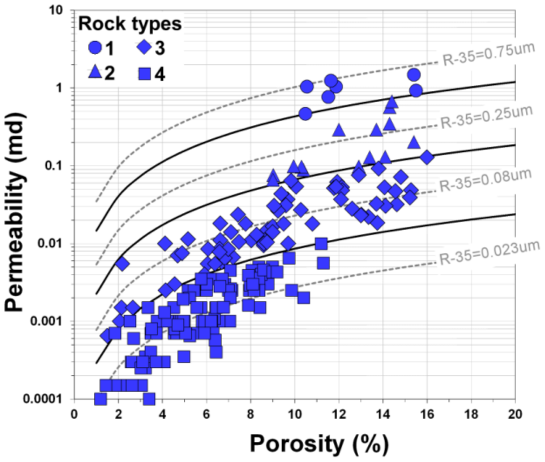

Figure 2.8: Average Winland R35 values generating rock type-dependent porosity-permeability functions (grey dashed lines).

The continuous absolute models are computed from the two alternative log-derived rock type models and the total porosity logs using simple Boolean statements.

Figure 2.2 (track 9) displays an example of the log-derived permeability using the MCA-derived rock type; blue circles represent absolute permeability from core plugs.

### *2.4.5.2 Relative and Effective Permeability*

The approach for fitting discrete measurements to gas relative permeability vs. water saturation functions in drainage cycles uses the engineering form of the Corey equation (Brooks and Corey 1964), which states that:

$$k_{rgD} = \left(1 - \frac{(S_w - S_{wcg})}{(1 - S_{gc} - S_{wcg})}\right)^{ngd}$$

where KrgD is the non-wetting phase (gas) drainage relative permeability, Sw is the wetting phase saturation, Swcg is the critical water saturation for the gas phase, Sgc is the critical gas saturation, and ngd is the slope of the relative permeability to water function. The Swcg, Sgc and ngd parameters are optimized to reduce the mismatch between discrete measurements and the KrgD fitting function.

For permeability measurements taken in imbibition cycles, the fitting function states that:

$$k_{rgI} = \left(1 - \frac{(S_w - S_{wi})}{(1 - S_{wi} - S_{gt})}\right)^{ngi}$$

where Swi is the initial wetting phase saturation and the Sgt is the residual non-wetting phase (gas) saturation.

Figure 2.9 displays permeability fitting parameters and resulting functions for a sample with seven measurements, four taken in drainage cycle, and three in imbibition cycle.

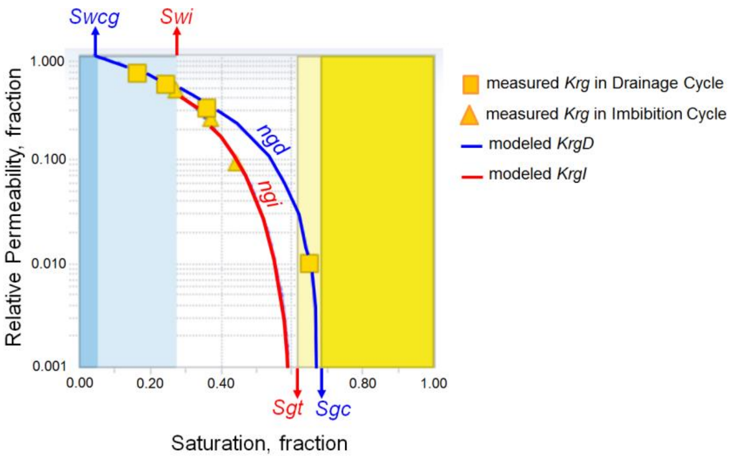

Figure 2.9: Modelling of gas relative permeability functions in drainage and imbibition cycles.

Gas relative permeability is modelled in individual samples; then the samples are classified by rock types based on the scheme described in 2.4.4.1. Final drainage and imbibition gas relative permeability functions (KrgD and KrgI) are averaged by rock type; results are shown in Figure 2.10. Notice that the number of samples is larger for poorer rock qualities (3 and 4); there is only one sample representing rock type 2. Since rock type 1 was not sampled, its parameters are assumed to be slightly more optimistic than rock type 2.

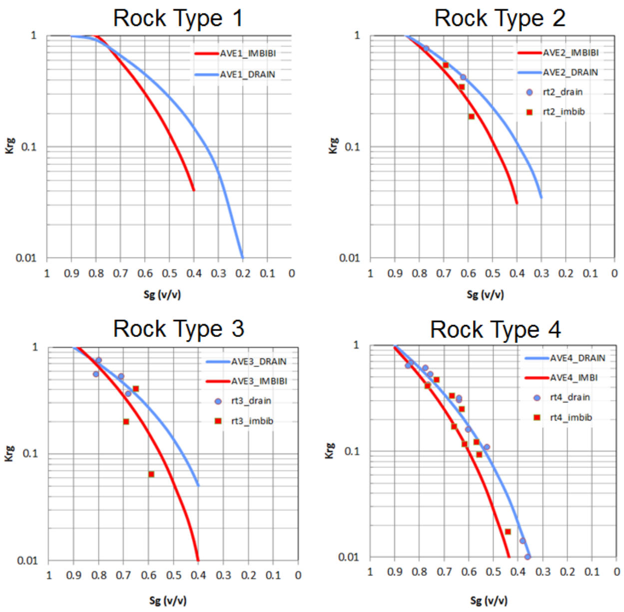
Rock Type 1

Rock Type 2

Rock Type 3

Rock Type 4

Figure 2.10: Averaging of gas relative permeability functions by rock type.

The log-derived effective permeabilities are computed as follows:

$$K_{egD} = K_{abs} \times K_{rgD}$$

$$K_{egI} = K_{abs} \times K_{rgI}$$

where Kabs is the log-derived absolute permeability and KrgD and KrgI are continuous parameters derived from modelled functions and log-derived total water saturation. Figure 2 (track 10) displays absolute and effective permeabilities for a reference cored well.

## 2.5 CALIBRATION TO DYNAMIC DATA

Production logs are devices lowered into the borehole that describe the nature and behavior of fluids during production. These logs are considered “dynamic measurements” and report type of fluid and rate of flow by reservoir depth. This type of logs commonly represents the first confirmation of whether fair reservoir quality interpreted from logs actually yields hydrocarbon after the rock is hydraulically stimulated.

The percentage of individual reservoir contribution interpreted from production logs is used to qualitatively validate the log-derived gas effective permeability model (Merletti et al., 2013). Such logs are commonly run weeks after the well is completed. Since weekly production might vary substantially, the average production during the first 30 days after completion (IP-30) is taken as the basis for this analysis.

Figure 2.11 details this validation in a borehole with an IP-30 equal to 350 mcfd. Tracks 1 thru 3 display the basic petrophysical log, track 4 shows the petrophysical rock type interpretation and track 6 absolute and effective gas permeability. Track 6 displays the perforated intervals. It is assumed that the hydraulic fracture connects the upper two perforations; therefore, they are treated as one entity. Track 7 shows the zonal contribution (% gas) interpreted from the production log and track 8 corresponds to the interpreted gas flow tied to the IP-30 of the well.

The remaining tracks report the interpretation from the log-derived gas effective permeability. Track 9 corresponds to the summation of gas effective permeability times thickness (Keg.H) over each perforation. Track 10 is the relative contribution of perforated reservoir to the cumulative KegH (5.94 mD.Ft). Finally, Track 11 shows interpreted gas flow rates from the log-derived model.

This type of validation was performed in other wells with production logs in order to challenge the validity of the log-derived rock type interpretation and the gas effective permeability model. Production logs confirmed that perforation 1, which is mostly composed of rock type 2, is the largest contributor with 234 thousand cubic feet of natural gas per day (MCFD). Perforation 6, composed of a one third of the thickness by rock type 2 and two thirds of rock type 3, is the second largest contributor with 64 MCFD. The latter perforations make 85% of the production of the well. The remaining

15% comes exclusively from rock type 3 which is not an efficient contributor to the overall hydrocarbon production.

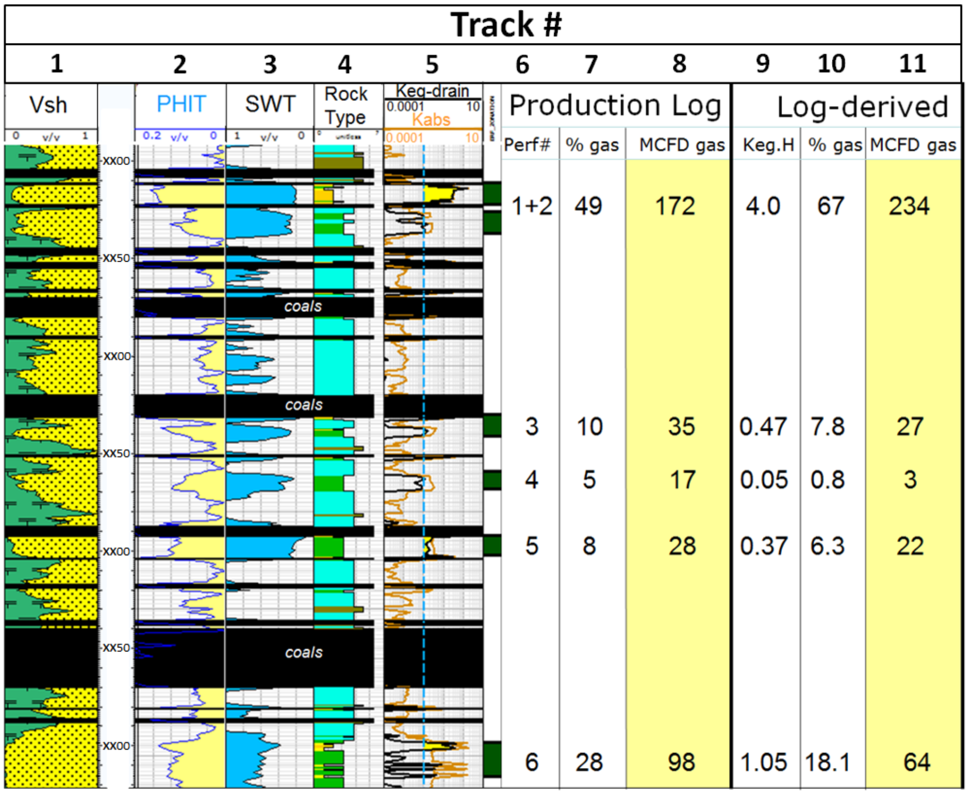

| Production Log | | | Log-derived | | |
|---|---|---|---|---|---|
| Perf# | % gas | MCFD gas | Keq.H | % gas | MCFD gas |
| 1+2 | 49 | 172 | 4.0 | 67 | 234 |
| 3 | 10 | 35 | 0.47 | 7.8 | 27 |
| 4 | 5 | 17 | 0.05 | 0.8 | 3 |
| 5 | 8 | 28 | 0.37 | 6.3 | 22 |
| 6 | 28 | 98 | 1.05 | 18.1 | 64 |

Figure 2.11: Qualitative validation of log-derived, gas effective permeability with production log interpretation. All production rates are tied to IP-30 of each well (Merletti et al., 2013)

The lack of consistency between the petrophysical rock quality and the zonal contribution of hydrocarbon from production logs can be caused by the presence of natural fractures in the vicinity of boreholes. When low quality rock intervals (i.e., rock types 3 and 4) produce large amounts of hydrocarbon, a common explanation is the presence of a natural fracture network contacted either by the borehole or by the hydraulic fracture. This additional contribution to production has not been observed in the wells used for this study.

## 2.6 SUMMARY AND CONCLUSIONS

This study focused on calibrating wireline log to core measurements collected over the Almond formation in the Wamsutter field. A subset of 1,450 wells was selected over an area of 6,600 Km2 to construct a petrophysical model that characterizes a wide range of reservoir qualities. Three whole cores cover the entire Almond formation with plug measurements performed using the latest generation of lab equipment. These routine and special core analyses provided the “ground truth” for the log-based petrophysical evaluation.

The neutron-density crossplot and a nonlinear (Clavier) gamma ray-derived shale volume models were evaluated and their pros and cons discussed. The fact that the majority of neutron logs older than 15 years need variable log normalization led to the decision for gamma-ray derived models. Still, the neutron log is very valuable in the flagging of coals along the stratigraphic column. The total amount of clay ranges between clay-free reservoirs to shale volumes around 10%. As a rule of thumb, half of the clay content can be kaolinite and mixed layer illite-mica; the other half can be mixed-layer illite-smectite. The percentage of expandable clay in the mixed-layer is relative small (<15%) and any effect on the electrical conductivity of reservoirs is considered negligible.

The density-derived total porosity displays a fair match with the helium porosity from the lab measurements. The good agreement is a result of an optimization routine where the RHO_fl is interactively changed in 0.05 g/cc steps until the modelled and the (measured) core porosity difference is minimized. Total porosity at in-situ conditions varies between 1 and 16%.

The water saturation model uses the Archie model with variable electrical properties and salinity values tied to the depositional environment. The log-derived water saturation model displays a fair agreement with direct measurements of water recovered from core plugs by Dean-Stark distillation. Reservoirs above the fluids transition zone exhibit water saturation values between 15 and 40% depending on the petrophysical rock quality.

Four petrophysics rock types were defined in total porosity, absolute permeability and capillary pressure space. Such a rock type scheme was extrapolated to wireline logs using stochastic and deterministic approaches. Common log inputs were gamma ray, bulk density, neutron porosity and electrical resistivity logs. The two alternative log-derived rock type models were combined with total porosity to obtain rock type-dependent absolute permeability logs. Absolute permeability varies between 0.0001 to 1 mD and each petrophysics rock type covers approximately one order of magnitude permeability.

Rock type-dependent relative permeability functions were derived from pulse-decay lab measurements using the Corey model. The input of such functions is the Archie's water saturation model validated by distillation processes in core plugs. The (static) gas effective permeability model was validated against production logs in a few wells. The validation exercise confirmed that rock types 1 and 2 are the largest contributors of the hydrocarbon coming out of reservoirs after stimulation. The largest zonal contribution in the production log coincides with the reservoirs with the largest gas permeability thickness. Rock type 3 might be a hydrocarbon contributor only if found over thick intervals, something that is unrealistic given the Almond's average net-to-gross value (~20%). Hydrocarbon produced in analyzed wells comes from hydraulically-stimulated rock matrix; there is no apparent contribution to production from natural fractures in the vicinity of boreholes. The static-to-dynamic validation is a must-do activity before sophisticated modelling, such as saturation-height modelling, is planned and executed.

# CHAPTER 3 INTEGRATION OF DEPOSITIONAL, PETROPHYSICAL, AND PETROGRAPHIC FACIES

## 3.1 ABSTRACT

Understanding the linkages between grain mineralogy, and diagenetic and sedimentary processes enhances the reliability of petrophysical models to predict reservoir deliverability from permeability. Petrographic data within well-defined depositional facies associations reveal the diagenetic evolution of porosity-permeability relationships. Formation evaluation methods relying solely on petrophysical rock typing are seriously limited when predicting ultimate reservoir performance in complex pore geometries.

The Almond Formation is characterized by three depositional facies associations; shoreface, deltaic (bay-head, flood-tide) and fluvial/coastal plain, which present three distinctive porosity-permeability trends. Textural features resulting from depositional processes, such as grain size and sorting, vary little between facies associations yet permeability can vary by up to four orders of magnitude for the same porosity value. Differences between petrophysical facies are primarily driven by diagenetic (cementation and grain dissolution) effects on different framework grain compositions (petrographic facies).

The characterization of depositional and diagenetic controls on pore geometry allows the narrowing of uncertainty in absolute permeability prediction. In this study, I quantify the relationship between depositional facies, with their specific mineral composition and diagenetic overprint, and the steepness functions in porosity-permeability space. The permeability model derived from the understanding of depositional and diagenetic processes is compared against two models built solely on

petrophysical rock typing. The former exhibited the best correlation with post-hydraulic fracture initial gas production in a large (44) number of wells.

## 3.2 INTRODUCTION

‘Tight gas reservoir’ is a term commonly used to refer to low-permeability gas-bearing reservoirs. Early definitions of tight gas reservoirs related the expected gas permeability to specific values (i.e., less than 0.1 mD). A more comprehensive definition of a tight gas reservoir is “a reservoir that cannot be produced at economic flow rates nor recover economic volumes of natural gas unless the well is stimulated by a large hydraulic fracture treatment, by a horizontal wellbore, or by use of multilateral wellbores” (Holditch, 2006). Three groups of parameters must be considered in assessing the potential for economically successful development of tight gas reservoirs. These are the geological parameters, the petrophysical properties of the net reservoir, and the mechanical properties of both net reservoir and encasing rocks (e.g. Sebastian et al., 2015; Sun et al., 2015; Spain et al., 2015; Cadwallader et al., 2015).

The main geological parameters include those associated with the sedimentary system, regional tectonics, and the regional thermal and pressure gradients. Sedimentary systems contain specific suites of depositional environments, which are characterized by specific facies associations. Facies associations record a suite of sedimentary processes (e.g., transport, reworking and burial) observed in modern analogs to have formed specific geomorphic features. Tying depositional facies associations to log signatures permits characterizing the distribution of facies associations and expected reservoir architecture, namely dimension, textural maturity, and mineralogy (Fisher and Brown 1984; Berg 1986). Furthermore, applying the basic petrophysical properties of the net reservoir defines the pay thickness, porosity, water saturation, and absolute permeability, from which gas in place and deliverability are derived.

In this study, I improved the understanding of the links between the depositional and diagenetic processes that give rise to the in-situ petrophysical properties related to the storage and flow capacity of reservoirs, namely porosity and permeability. Diagenesis comprises all processes that convert sediment to rock (Worden and Burley, 2003). Prior to the onset of diagenesis, porosity and permeability are controlled by sediment composition and conditions that prevailed during deposition. Diagenesis commonly reduces the original porosity and average pore throat diameter, causing an increase in both tortuosity and the number of isolated and/or disconnected pores (Rushing et al., 2008). However, diagenesis can locally increase porosity through the formation of fractures, removal of cements or leaching of framework grains (Ali et al., 2010). The net result of diagenetic processes can be a complex pore structure evidenced by wide scatter in porosity-permeability space (Figure 1).

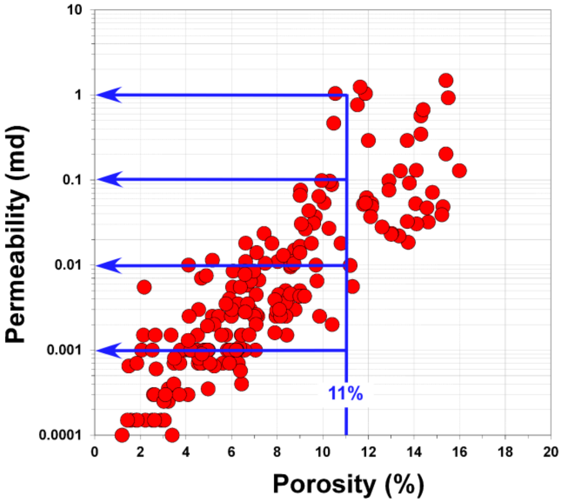

Figure 3.1: Complex reservoir demonstrating scatter in porosity-permeability space. Permeability can vary by up to four orders of magnitude at a single porosity.

Notice how an 11% porosity reservoir can vary by four orders of magnitude in permeability. The derivation of permeability from logs remains a challenge in uncored wells because commonly acquired logs only respond to porosity, relative fluid volume, and lithology.

The analysis of depositional facies with petrographic information in porosity-permeability (Ø-K) space helps identify drivers for improvement or deterioration of reservoir quality; in other words, the prediction of different Ø-K trends. Once depositional and diagenetic controls on pore geometry are characterized, one can use well logs to infer the properties needed for narrowing the uncertainty in the in-situ permeability assessment. For instance, variations in porosity and quartz content can be used for interpreting the steepness of trends in Ø-K space (Merletti et al., 2014). Log-derived permeability models are integrated over depth to generate flow capacity profiles which, in turn, are correlated with dynamic reservoir performance indicators such as production logs and initial production indexes. The uncertainty in resource recovery is considerably reduced when the link between static and dynamic reservoir flow capacity is established.

### 3.3 DEPOSITIONAL, PETROPHYSICAL AND PETROGRAPHIC FACIES

Rushing et al. (2008) summarizes the various rock type classification schemes in sandstones and carbonate reservoirs. We agree on the concept that depositional, petrographic and hydraulic rock types capture different physical and chemical processes affecting rock properties during and after deposition (Newsham and Rushing, 2001; Rushing and Newsham, 2001). However, I prefer to use the term “facies” when describing such processes and to exclusively use the term “rock type” for describing rocks with similar flow characteristics.

Depositional facies are defined as rock intervals exhibiting a particular combination of lithological, sedimentological and biological structures (de Raaf et al., 1965; Middleton, 1978). These facies are commonly described in outcrops and whole cores. Their interpretation links sedimentary structures to transport, reworking and early burial to define depositional environment. Depositional facies can also be defined on a fine scale with subtle differences (i.e., minor differences in the style of lamination) not detectable with basic well logs. Therefore it is practical to combine closely related facies into facies associations or groups of facies genetically related to one another, and which have some environmental significance (Collison, 1969). These coarser scale depositional facies associations (DFA) have also been termed architectural elements, implying they are the building blocks of various depositional systems (Jackson 1976; Miall, 1985). Reservoir continuity and connectivity can be interpreted from DFA mapping.

Rock types (petrophysical facies) are grouped by rock with similar flow characteristics, related to pore throat size or hydraulic radius. Rock types are commonly defined through laboratory measurements of porosity, permeability and capillary pressure on core plugs. There are empirical and experimental approaches for classifying reservoirs into rock types. Amaefule et al. (1993) proposed the use of a parameter called Flow Zone Indicator (FZI) to characterize rock intervals with similar pore throat attributes, which were referred to as "hydraulic units". This method, applicable to properties derived from routine core analysis, does not require parameters difficult to measure experimentally, such as the shape factor and the Kozeny constant. Rather, the FZI is calculated from core-derived effective porosity and permeability.  Other authors published regression-based, experimental models that relate effective pore throat radius (PTR), total porosity, and absolute permeability to air (Pittman, 1992; Gunter at al., 1997 and 2014). Once rock types are defined in core measurements and extrapolated to log data, they are used for computing rock type-dependent porosity vs. permeability functions, water saturation vs. height profiles and gas/water relative permeability vs. water saturation functions (Spain et al., 2015).

Petrographic facies can be defined as rocks displaying similar textural attributes, framework, matrix and cement composition, porosity types, etc. They are mostly described through point-count petrological analysis of thin-sections and complemented by observations using scanning electron microscopy (SEM) and X-ray diffraction (XRD).

### 3.3.1 Diagenetic controls on pore structure

Depositional and diagenetic processes control the evolution of pore characteristics in sandstones, reducing porosity from up to 45% at deposition through the combined processes of compaction and cementation (Armitage et al., 2010) to its current porosity and permeability. Three key diagenetic processes act to modify sandstone pore throat characteristics: 1) mechanical compaction and pressure solution (chemical compaction), 2) cementation and 3) dissolution.

Mechanical compaction mechanisms include re-orientation and closer packing of grains, plastic deformation of ductile grains, and ultimately fracturing of rigid grains. More ductile grains, such as clays and certain volcanic rock fragments, compact to a greater degree than more rigid grains such as quartz. Early cementation or reduction in effective stress by increased pore fluid pressure can work to reduce mechanical compaction (Ali et al., 2010). Pressure solution (sometimes referred to as chemical compaction) in siliciclastics is the process of dissolution at contact points between quartz grains and transport of solute into the adjacent pore space (Sheldon et al., 2003). Dissolved material is thought to be precipitated on adjacent quartz grains and not to be transported significant distances.

Cementation is the process by which ions are precipitated from pore fluid to form new crystalline material on or between existing grains. Common cements include quartz, carbonate and authigenic clay minerals which typically act to progressively reduce porosity and permeability. However, early cementation can act to strengthen the rock framework and retard porosity loss by mechanical compaction. Additionally, small amounts of grain coating authigenic clay can inhibit quartz cementation by reducing nucleation sites for quartz overgrowth (Bloch et al., 2002). Figure 2 shows hypothetical changes along a single Ø-K trend. Compaction followed by cementation tends to decrease log(k) proportionately as Φ is decreased.

Dissolution of sedimentary grains, matrix, and authigenic cements by reactive pore fluid can act to locally change porosity and permeability. Pore space developed by dissolution is known as secondary porosity (Ali et al, 2010). Figure 2 shows how dissolution can increase porosity without causing significant improvements in permeability.

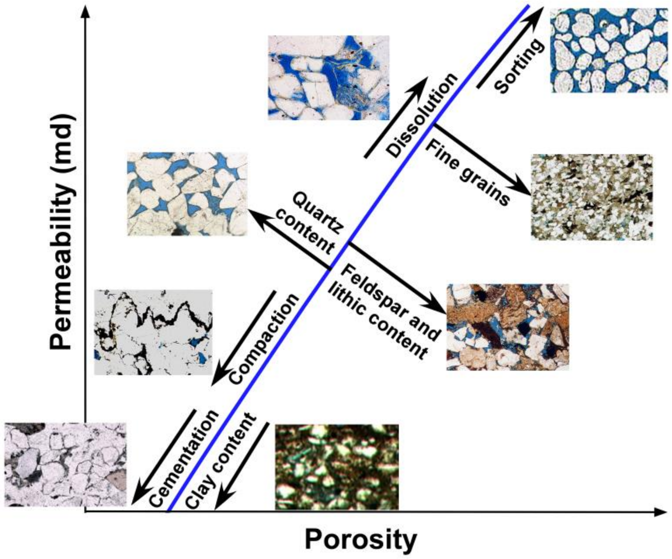

Figure 3.2: Hypothetical changes to a single Ø-K trend resulting from different depositional and diagenetic processes.

Textural parameters present at deposition exert some influence in porosity, permeability and the development of diagenesis (Hartmann and Beaumont, 1999). Porosity is independent of grain size but permeability is strongly affected by grain size; the finer the sand, the lower the permeability (Beard and Weyl, 1973). Good sorting tends to correlate well with both high porosity and permeability (Figure 2). Poorly sorted sandstones typically have more detrital clay and non-quartz grains.

## 3.4 METHODS AND DATA

### 3.4.1 Depositional Facies

Almond depositional facies have been interpreted by various authors from outcrops (e.g. Roehler 1988 or Kieft et al., 2011) and high-resolution subsurface data such as whole cores (Lawrence, 2007) and borehole electrical images (Blomenkamp et al., 2007). Less than five percent of the subsurface data have cores or borehole electrical images; most of the acquired data are low-resolution triple-combo logs which respond to lithology and porosity changes. It is difficult to distinguish depositional facies solely by log response because of vertical resolution limitations and/or petrophysical property changes are not large enough to yield different log responses; good examples are “cross-stratified sandstones” and “massive, structureless sandstones”. However, when depositional facies are grouped into architectural elements or depositional facies association, the extrapolation of facies described in cores or borehole images using log pattern recognition becomes less uncertain.

Three depositional facies associations were defined in cored wells and calibrated to log patterns; these are fluvial/coastal plain, back-barrier deltas & tidal inlet channels and shorefaces. The fluvial /coastal plain facies association are nonmarine equivalents to shallow marine deposits. Facies include (from base to top) fine-grained rippled and planar-laminated sandstone, structureless sandstone, very fine-grained planar laminated argillaceous sandstones, siltstone, silty mudstone and mudstone (Figure 3.3). Sandstone facies rest abruptly on mudstone, silty mudstone or rarely coals. The contact between sandstone and underlying fine deposits can be sharp or locally erosional. When the contact is erosional it is usually filled with a lag of silty mudstone and coaly clasts. The fluvial facies were likely deposited by meandering channel systems because they yield an upward-increasing GR log pattern typical of point bars, though these become blocky if multiple sandbodies are amalgamated. Rippled and deformed very fine-grained sandstones facies are interpreted as overbank deposits and produce a slightly upward-decreasing GR log pattern.

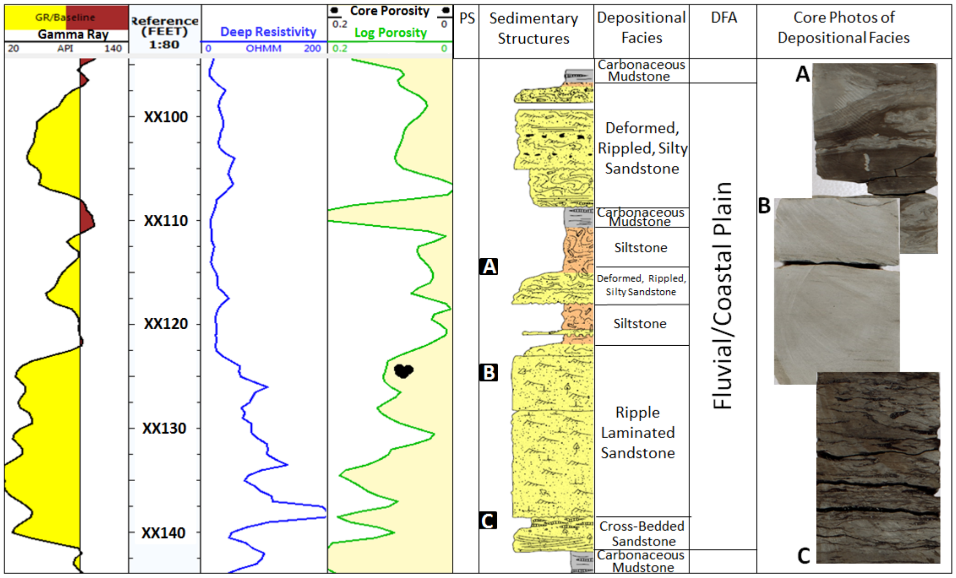

Figure 3.3: Section of core showing sedimentary features and their calibration to log patterns for the fluvial/coastal plain facies association (modified from Quest and Gatling, 2007)

The back-barrier delta facies association includes flood-tidal and associated inlet channel and bay-head deltas developed in the lagoon environment. It is commonly composed of very fine- to fine-grained, upward-coarsening sandstone successions that are thinner than 15ft (Figure 3.4). Individual depositional units can be 1 to 8ft thick and includes (from base to top) interbedded heteroliths, ripple laminated sandstone, and structureless or horizontal planar laminated sandstone. In a few cases, the interbedded heterolithic facies passes directly to cross-bedded sandstone. Some upward-coarsening units are overlain by structureless bioturbated mudstone, carbonaceous mudstone and coals.

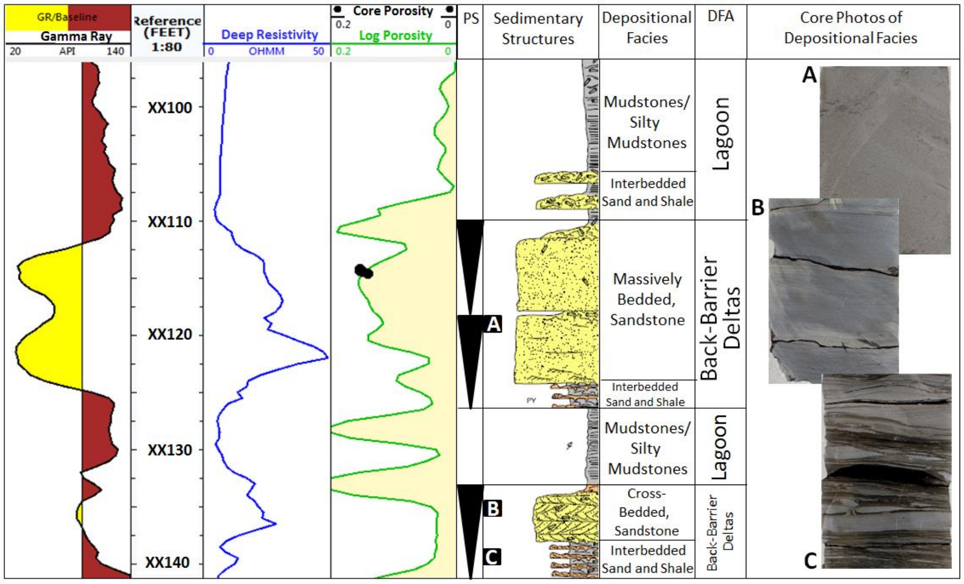

Figure 3.4: Section of core showing sedimentary features and their calibration to log patterns for the back-barrier delta facies association (modified from Quest and Gatling, 2007).

The shoreface facies association is typically composed of very fine- to medium-grained, blocky to upward-coarsening sandstone-dominated successions which can be 25 to 100ft thick. Individual depositional facies can be 0.5 to 6ft thick and include massive (structureless) sandstone, rippled sandstone, planar-and trough cross-stratified sandstone, parallel stratified sandstone, swaley cross stratified sandstone, intensively bioturbated sandstone, oyster-rich shaly sandstone and interbedded heterolithics. The occurrence and abundance of each facies, the type of contact (i.e., sharp vs. gradational) and the bioturbation index provides insights on the wave energy of the shoreline. Figure 3.5 displays an example of the shoreface depositional facies association in the Siberia Ridge reservoir. The core shows a 25-feet fine to very fine grained sandstone deposited on top of siltstones of the Echo Springs' lagoonal environment. Facies pass (upward) from structureless and rippled sandstones to planar and parallel stratified sandstones. Toward the top, the sandstone is intensively burrowed and bioturbated.

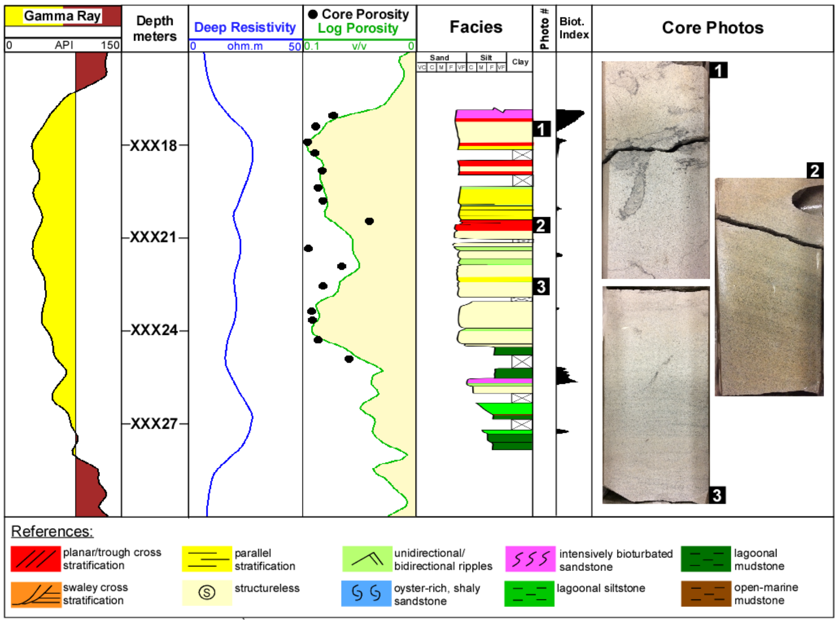

Figure 3.5: Section of core showing sedimentary features and their calibration to log patterns for the shoreface facies association.

### 3.4.2 Petrophysical Facies (Rock Types)

Since regression-based models are supported by hundreds of lab measurements, I prefer their use over empirical approaches. The rock typing interpretation starts by examining mercury injection capillary pressure (MICP) tests and their associated porosity and permeability values. The Winland plot (Kolodzie, 1980; Gunter et al., 1997) is used for identifying four rock types in Almond samples, for which boundaries are picked at PTR of 0.45, 0.15 and 0.045 microns (Figure 3.6).

Equations allow the prediction of the effective PTR (R35) from samples with only routine core analysis tests. Additionally, if the average R35 value for each rock type is interpreted as shown in Figure 3.6 (grey dashed lines), permeability can be calculated from porosity and a discrete rock type model.

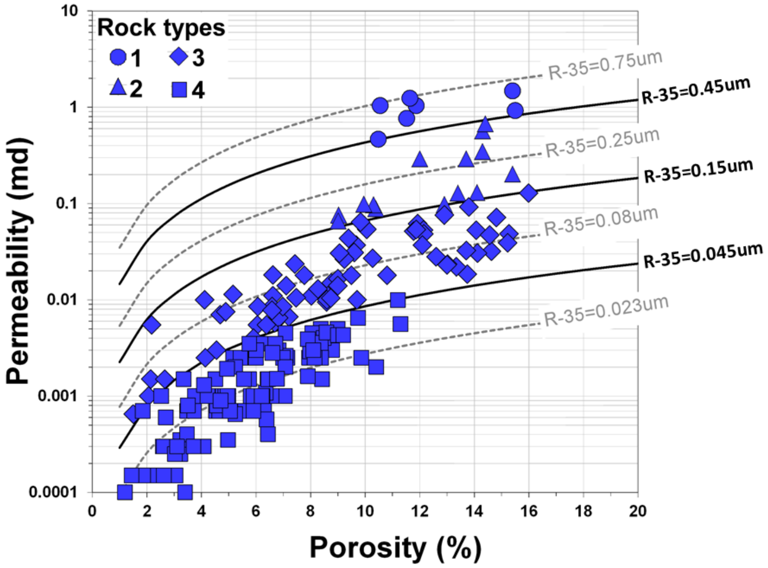

Figure 3.6: Average R35 values for rock type boundaries (black continuous lines) and porosity-permeability functions (grey dashed lines).

### *3.4.2.1 Results: Depositional Facies associations in Porosity-Permeability Space*

Porosity and permeability measurements at reservoir conditions are sorted by their depositional facies associations (DFA), which are interpreted from core descriptions. Group 1 (Figure 3.7, green circles) corresponds to samples interpreted as fluvial/coastal plain, Group 2 (yellow dots) corresponds to Shoreface and Group 3 is assigned to bay-head, ebb, and flood tidal delta deposits (red dots). Notice the existence of different trends, which merge in porosity values around 9% (i.e., below that there is a common porosity-permeability trend regardless of the DFA). Group 1 exhibits the best flow capacity at moderate porosity values (e.g., ≈12%). However this group exhibits the smallest storage capacity of the three groups. When parameters such as net thickness, lateral continuity, storage, and flow capacity are evaluated jointly, Group 2 is considered to have the best reservoirs. Most of the historical Almond production has been from this group in a ‘sweet spot’ named Echo Spring-Standard Draw (Horn and Schrooten 2005).

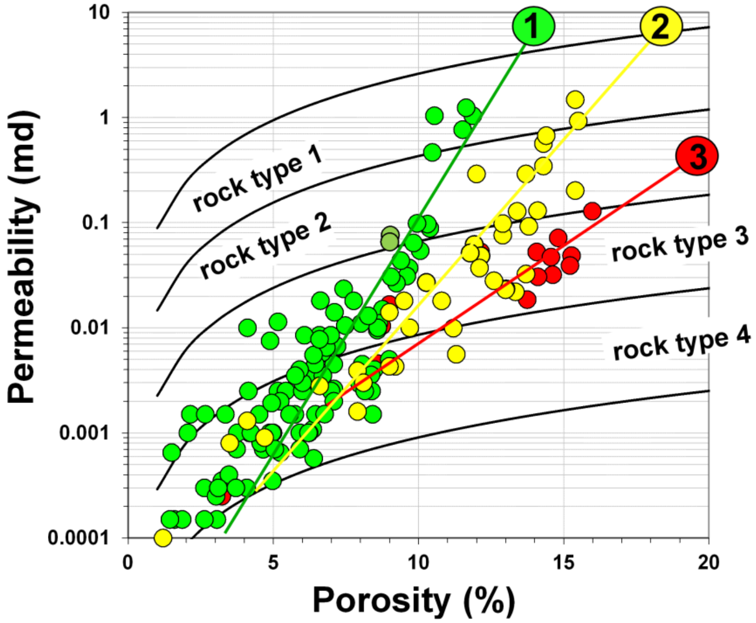

Figure 3.7: Depositional facies associations show distinctive trends in porosity-permeability space. Trends 1, 2 and 3 represent fluvial/coastal plain, shoreface and delta Depositional Facies Associations respectively.

### 3.4.3 Petrographic Observations

Tobin et al., 2010 described the diagenetic controls on rock quality in the Almond. Diagenetic processes affecting complex detrital mineralogy has led to loss of primary porosity from mechanical compaction, pressure solution (chemical compaction) and cementation. Secondary porosity resulted from feldspar and volcanic rock fabric dissolution. Micropores are found within the detrital clay matrix, chert, and volcanic grains. The relative amounts of these pore types control the porosity–permeability relationships. These authors identified eleven “petrofacies” based on a combination of wireline log characteristics, core measurements and petrographic features. Some properties (e.g., sorting, grain size, permeability) are difficult to predict in uncored wells and the recognition of such petrofacies can be uncertain if only based on log characteristics. My strategy consists of evaluating petrographic features in ternary and box plots by the depositional facies associations. The objective is to understand drivers for rock quality preservation and degradation.

Figure 3.8 displays variations in the mineral composition of framework grains in a quartz-feldspar-lithics (QFL) ternary plot. Shoreface has a higher proportion of feldspars, volcanic rock fragments, and depositional and authigenic clay material – all of which are typically associated with secondary and micro–porosity. The amount of quartz decreases and the percentage of lithics and feldspar increases from fluvial-coastal plain to shoreface. There are likely two sources of sediment; one is quartz-rich western provenance area which is associated to the Sevier orogeny and fed fluvial deposits in the Ericson Formation and the Lower and Middle Almond. The second source of sediment is a northern and northwesterly lithics- and feldspar-rich provenance that brings sediment from the Granite Mountains to the Red Desert Delta (Roehler, 1988) and its distributaries. Bay-head deltas, fluvial and shoreface deposits in the Upper Almond were fed by this sediment source.

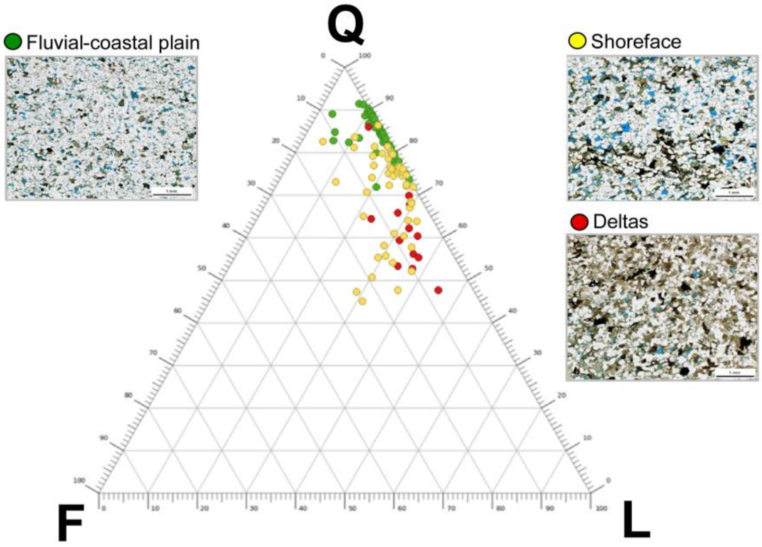

Figure 3.8: Quartz-Feldspar-Lithics (QFL) ternary plot

Figure 3.9 displays point-count (visible) porosity in the x-axis and unstressed helium total porosity in the y-axis for each DFA. Departures above the 45° line can be taken as a qualitative proxy for larger amounts of micro-porosity as a proportion of the total porosity. Notice that deltaic facies, followed by shoreface facies, has more micro-porosity in proportion with total porosity than the fluvial-coastal plain; this leads to more tortuous porosity networks and lower permeability for a given porosity. These differences in pore architecture arise from differences in primary depositional fabric and mineralogy and their subsequent alteration during diagenesis.

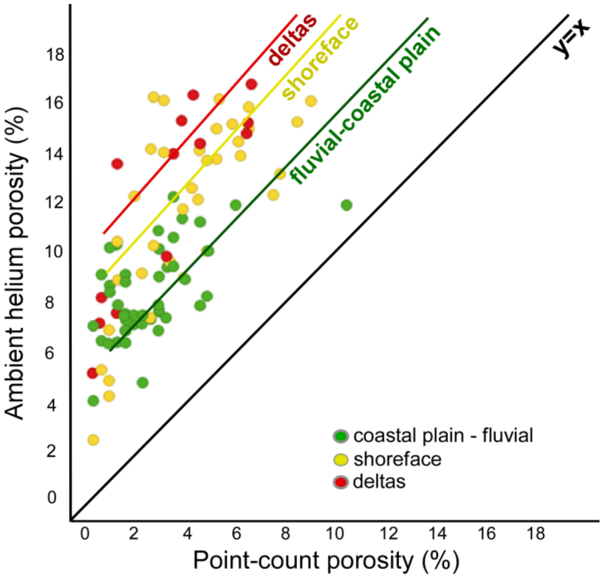

Figure 3.9: Point-count total porosity (x-axis) vs. routine core analysis-derived ambient total porosity (y-axis).

The box plots in figure 3.10 show various textural characteristics by DFA. Shoreface deposits have a wider distribution of mean grain size and a tail toward higher values than deltaic and fluvial-coastal plain facies (Figure 3.10A). The latter exhibits the largest intergranular porosity followed by shoreface, and deltaic (Figure 3.10C). The mean of total cement distribution does not show a relevant variation among DFA (Figure

3.10B). Given the larger amount of feldspar and lithics in framework grains (Figure 3.10), shoreface facies shows a similarly larger amount of secondary porosity than deltaic facies; quartz-rich fluvial-coastal plain facies display the lowest secondary porosity (Figure 3.10D).

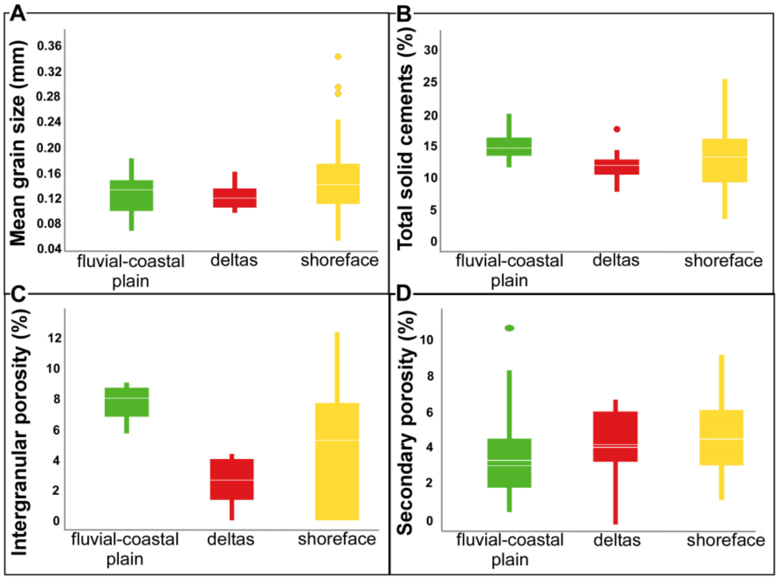

Figure 3.10: Box plots displaying mean grain size (A) total cement, (B) intergranular porosity, (C), and secondary porosity (D).

### 3.5 DISCUSSION: INTEGRATION OF FACIES

Fluvial-coastal plain deposits exhibit the steepest porosity-permeability trend (Figure 3.7). Its larger quartz content (Figure 3.8) better preserved primary intergranular porosity (Figure 3.10C) from mechanical compaction, and led to less grain dissolution. Since most of the framework grains are compositionally stable, there is not much grain dissolution that could potentially increase the storage capacity of these deposits. Therefore, this DFA is associated with the low-porosity end of each petrophysical rock type (Figure 3.7).

The shoreface deposits represent a high-porosity and high-permeability end member for petrophysical rock types 1 and 2 (Figure 3.7); these deposits display the best storage and flow capacity. Most of the Almond production has been from shoreface deposits in a sweetspot named Echo Spring-Standard Draw (Horn and Schrooten 2005). The good reservoir quality is associated with tails of high mean grain size (Figure 3.10A) and intergranular porosity (Figure 3.10C). Figure 3.8 shows that the shoreface facies has a higher proportion of feldspars, volcanic rock fragments, and depositional and authigenic clay material – all of which are associated with secondary (Figure 3.10A) and micro–porosity (Figure 3.9). This leads to more tortuous porosity networks and lower permeability for a given porosity creating detachment from fluvial-coastal plain trend.

Bay-head, ebb and flood tidal deltaic deposits demonstrate the lowest rate of increase of permeability with porosity (Figure 3.7). This facies has the lowest intergranular primary porosity (Figure 3.10C) and the largest proportion of micro-porosity (Figure 3.9), which is driven by the high abundance of dissolution. Previous observations indicate that the effect of primary depositional processes on trends observed in porosity-permeability space is not as direct as it was originally believed. Rather, trends are driven by diagenesis targeting different framework grain compositions, which are associated with different sediment sources (river-supplied vs. long-shore transport). If diagenetic processes had less influence or if all depositional facies had the same framework composition (e.g. high quartz content), the separation between porosity-permeability trends would be less pronounced.

When depositional and diagenetic controls on pore geometry are understood within the stratigraphic framework, well logs can be used to derive the properties needed for reducing the uncertainty in the absolute permeability assessment (Figure 3.1). Since the amount of quartz framework grains systematically decreases from fluvial-coastal plain to shoreface to deltaic deposits, this property can be used with porosity to predict the correct trend for computing permeability. The quartz content can be interpreted from spectroscopy logs or from multi-detector pulsed neutron-derived Silica Activation Index logs (Zett et al., 2012; Merletti et al., 2014). Given that proxies for quartz content are often unavailable, we can exploit the relationship between depositional and petrographic facies with porosity-permeability and extract a most-likely trend by interpreting log patterns from open-hole logs. The pattern recognition is coupled with the stratigraphic correlation to generate DFA maps as the one shown in Figure 3.11A. The sand thickness map (Figure 3.11B) provides the boundaries of the reservoir container and porosity thickness map the volume available for fluids (Figure 3.11C). Notice how, even though the sand body extends to the upper right corner of the map, porosity decreases substantially in that direction and permeability is below the threshold of producible reservoirs (Figure 3.11D). Since those reservoirs are up to 2,000 feet deeper in the structure, they underwent much more mechanical compaction, quartz and carbonate cementation.

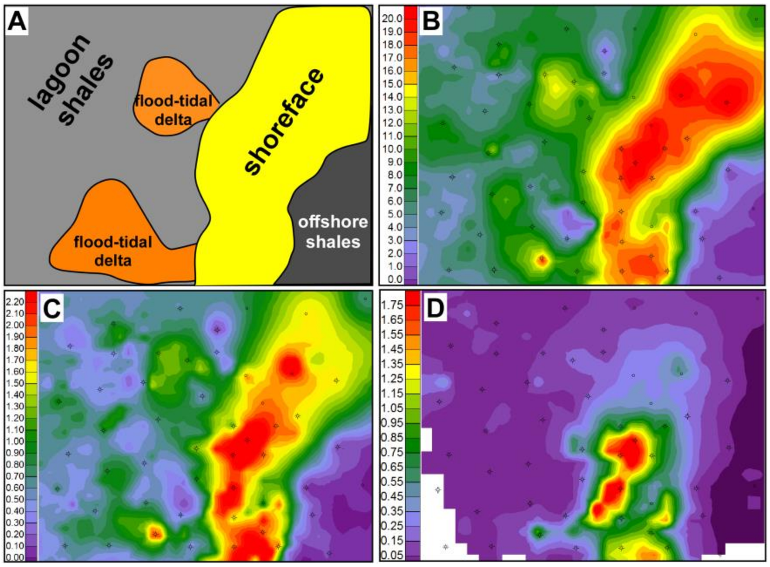

Figure 3.11: Maps displaying depositional facies associations (A), sandstone thickness (B), porosity thickness (C) and gas permeability thickness (D).

## 3.6 IMPLICATIONS: RESERVOIR PERFORMANCE PREDICTION

Merletti et al. (2013) compared three alternative core-calibrated, log-derived gas permeability models with actual initial reservoir performance. The first two models used the core-derived petrophysical rock typing scheme described previously for computing in-situ absolute permeability. The difference between the two models is the approach used (i.e., deterministic vs. neural network-based) for deriving a continuous rock type model from triple-combo logs. Having a continuous rock type and a porosity log, absolute permeability is obtained using the functions in Figure 3.6. The third model computed absolute permeability from porosity using a DFA model interpreted from log patterns and cross-checked by geological mapping.

The three absolute permeability models were converted to gas effective permeability (Keg) using the same rock type-dependent relative permeability functions and a resistivity-based water saturation model. Keg models were subsequently integrated over perforated intervals and compared to actual reservoir performance, post-hydraulic stimulation. Figure 3.12 shows crossplots between the average gas production 30 days after completion (IP-30) and the summation of gas effective permeability calculated over perforated intervals (Keg.H) for 44 uncored wells. Empty circles in each cross plot represent a subset of wells exhibiting low stimulation quality; these wells were excluded from any regression analysis.

When absolute permeability is derived through petrophysical rock types, the regression coefficient ($R^2$) is relative low; 0.22 and 0.29 respectively for models using neural network and deterministic approaches. The highest $R^2$ value corresponds to the model using the DFA scheme. Dashed lines represent boundaries of what is interpreted as successfully stimulated matrix permeability under similar reservoir pressure conditions. Data plotting outside of dashed lines toward the upper left corner represent reservoirs poorly stimulated or displaying evidence of depletion. Conversely, data plotting toward the lower corner of the plot represent low quality reservoirs displaying anomalously high gas production; this is associated to the presence of natural fractures intercepted by either the borehole or the hydraulic fracture generated in the stimulation process. Data plotted in Figure 3.12 confirms observations made in section 2.5; the contribution of natural fractures to the overall gas production in analyzed wells is negligible. However, this statement cannot be generalized for the entire field. Sturm et al. (2001) reported increased hydrocarbon production associated to the proximity of wells to structural lineaments and natural fractures in the Siberia Ridge field.

The scatter observed in Figure 3.12 between dashed lines is associated with different stimulation technology implemented in wells completed over a period of 40 years. Dawson et al. (2015) documented similar results in another tight-gas siliciclastic reservoir in the Middle East. They reported $R^2$ above 0.90 when reservoirs are stimulated using the same parameters (i.e., fluid type, proppant volumes, etc.) over 10 years.

Ideally, Keg.H derived from logs should be compared and reconciled with the same parameter obtained from pressure transient analysis (PTA).  Since the DFA-derived permeability yielded the best correlation with dynamic data, this model is used to populate the porosity distribution with gas effective permeability. Figure 11D demonstrates how an apparently continuous reservoir shrinks to smaller, less continuous areas when gas effective permeability or reservoir deliverability is incorporated with the regular reservoir mapping.

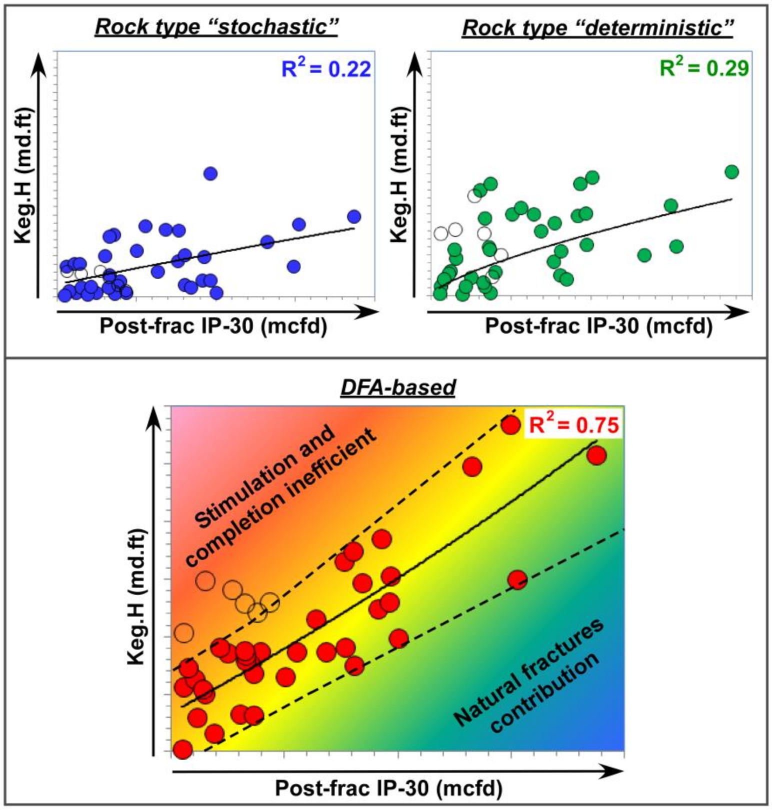

Figure 3.12: Correlation initial gas production (x-axis) and the summation of effective permeability to gas over perforated intervals (y-axis) for alternative permeability models.

### 3.7 CONCLUSIONS

The linkage between depositional facies, petrophysics rock types, and petrographic observations (framework composition, types/amount of cement, and porosity type) should be fully understood to more reliably predict reservoir performance. While this is recommended in conventional reservoirs, it is absolutely necessary in tight-gas sandstones where complex porosity-permeability relationships are expected. In the case of the Almond Formation, a 10% porosity reservoir could exhibit a range of four orders of magnitude for absolute permeability (Figure 3.1). Reservoirs with mean porosities around that value and an average net-to-gross could yield either an exceptional well or an uneconomic well, depending on the absolute permeability of those reservoirs.

The three depositional facies associations, shoreface, deltaic and fluvial-coastal plain, present distinctive trends in porosity-permeability space. The effect of primary depositional processes (e.g., hydrodynamic grain size sorting) on such trends is present, but it is not as significant as originally thought. Rather, trends are driven by diagenesis (cementation and grain dissolution) targeting different framework grain compositions which, in turn, are associated with source and transport mechanisms. The pore architecture differs with primary depositional fabric, but the current porosity and permeability result more from rock frame mineralogy and subsequent diagenetic overprint than from primary depositional fabric. The different rock frame mineralogy is associated with two sediment sources, one is quartz-rich western provenance area that fed fluvial deposits in the Ericson Formation and the Lower and Middle Almond; the other is a northern and northwesterly lithics- and feldspar-rich provenance that brought sediment from the Granite Mountains to feed bay-head deltas, fluvial and shoreface deposits in the Upper Almond.

When depositional and diagenetic controls on pore geometry are understood within the stratigraphic framework, one can systematically use well logs to more reliably predict absolute permeability. The reservoir porosity and the amount of framework quartz can be used to interpret the appropriate transform/trend for deriving absolute permeability from porosity. In this study, we apply DFA (with their specific mineral composition and diagenetic overprint) for permeability prediction.

DFA are interpreted using log pattern recognition and stratigraphic correlation (Figure 3.11A). Sand thickness maps provide the extent of the container (Figure 3.11B) and the pore thickness map indicates the available space for saturating fluids (Figure

3.11C). The permeability model derived from DFA exhibited the best correlation with post-hydraulic fracture initial production and therefore is used to populate the pore space with appropriate gas permeability functions (Figure 3.12). The effect of poor stimulation jobs, depletion and natural fractures can significantly reduce the correlation between initial production and log-derived Keg.H. Reservoirs exhibiting any of these effects should be excluded from the analysis to select the best model describing matrix permeability. These completions also identify potential remediation candidates and warrant further study. The computation and mapping of gas permeability thickness in the context of depositional facies architecture is a proven engine for integration. Such integration aims to guide an efficient development of complex tight gas reservoirs.

# CHAPTER 4 WATER SATURATION MODELS USING SPECIAL CORE ANALYSIS

## 4.1 ABSTRACT

Tight-gas reservoirs undergo unique and often complex burial, diagenetic, structural, fluid pressure and saturation histories. Porosity alteration from compaction, cementation and grain leaching can continue after hydrocarbon charge, further complicating saturation modelling. Many reservoirs have gone through multiple cycles of drainage and imbibition, often at different stages on the diagenetic pathway to current pore-scale morphologies. The understanding of saturation distribution and state is not only desired, but required for predicting reservoir performance, estimating realistic recoverable volumes, and optimizing costs for development and production.

Drainage and imbibition saturation-height models have been developed from core studies and integrated with logs to verify that reservoirs are at primary drainage and to highlight any potential imbibition due to trap tilting or leaking. Centrifuge and multi-cycle mercury injection data were integrated to produce composite drainage capillary pressure curves. Stressed mercury extrusion tests are commonly used for modelling water saturation through the imbibition process. These tests display no correlation with rock quality at low capillary pressures. To circumvent these problems, mercury extrusion was integrated with maximum trapped gas measurements obtained by counter-current imbibition experiments.

Using the resistivity-derived water saturation model as reference, the free water level for drainage and imbibition models was optimized by matching saturation-height models in reservoirs free of resistivity shoulder bed effects. The accuracy of the match in different rock qualities provided insights on the likely saturation state of reservoirs. Such

observations were used to develop successful interpretations of the spatial distribution of free-water level, reservoir architecture, and hydrocarbon charge.

## 4.2 INTRODUCTION

Tight gas reservoirs all have very specific histories of burial, diagenesis (porosity alteration due to compaction, cementation and grain dissolution, both before and after hydrocarbon migration), fluid pressures (over-pressuring and de-pressurization) and uplift, and hence their consequent saturation histories. The net result is that many tight gas accumulations have gone through several cycles of drainage, imbibition, re-drainage and re-imbibition, often at different stages on the diagenetic pathway to their current pore morphologies (Spain et al., 2013).

In the primary drainage process, the saturation of the non-wetting phase increases as hydrocarbon fills the pore space and displaces the original water of deposition. In this process, saturations are controlled by reservoir fluid densities, inter-facial tension (IFT), reservoir capillarity, and height above the free water level (FWL).

Tilting of the trap or leakage along faults can create a reduction of closure, leading to gas migration out of the trap, or gas accumulation pressure increase from further burial, can all reduce the gas column height and associated buoyancy pressure. This creates a situation where imbibition of water into gas saturated zones can occur. During imbibition events, water migrates along the water-wetting films to reduce the overall gas saturation of the pore system as the pressure differential between the gas and water phases reduces (Spain et al., 2013). For any pore throat there will be a critical pressure difference below which the gas phase continuity across it cannot be maintained. Snap-off occurs and severs the gas phase connection across the throat. Once all gas phase access to a pore is removed then the gas remaining in that pore is trapped (Figure 4.1).

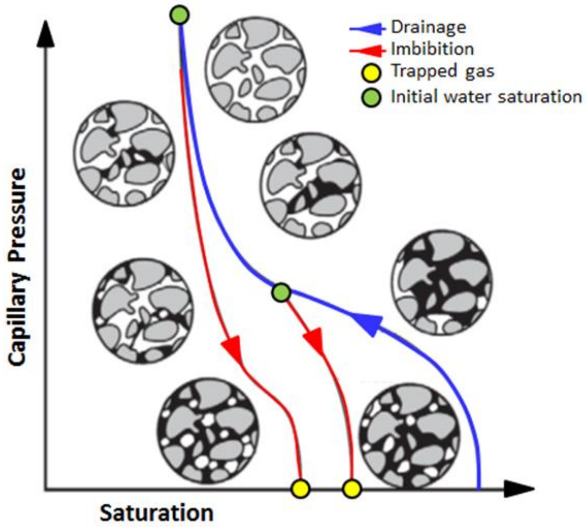

Figure 4.1: Core plug end-face saturations (grains grey, wetting-phase black, non-wetting phase white) indicating different phase (and continuous phase) distributions in drainage and imbibition conditions (modified from Spain et al., 2013).

In order to reconnect this gas (re-drainage), the controlling pore throat systems need to be resaturated. This can take place in a number of ways. Further gas migration and accumulation may occur in geologic time, increasing the buoyancy pressure (as the gas-water contact is lowered) within the system. Structural tilting can also cause secondary drainage by gas migrating from the portion of the structure undergoing imbibition. Both situations increase gas saturation for a greater volume of the continuous phase gas, which improves the gas effective permeability, gas production and deliverability, and reduces water effective permeability and water production.

Fluid distribution models of saturation vs. height above FWL are usually well-constrained for simple drainage conditions, but when imbibition and more complex re-drainage and re-imbibition occur, the concept of a current FWL as a datum from which saturations can be predicted (based upon drainage capillary pressure data) is lost. As a result, using core-derived fluid pressure measurements and log-computed saturations to predict a FWL depth is often impossible (Spain et al., 2013).

However, a couple of factors make the Almond formation behave more similarly to conventional reservoirs. First, the present day structure (Figure 4.2) in the northern half of the field is quite similar to the one in Eocene time when the hydrocarbon migration started. Second, the trap model has a strong stratigraphic component with the overlying Lewis marine shales providing the top seal and lagoonal and marine shales providing lateral seals. As the reservoirs are also charged with hydrocarbon by the Almond intraformational source rocks, they could have remained relatively isolated from basin configuration changes. These facts encouraged us to derive and implement drainage saturation-height models (SHM) for better understanding the correlation between saturation distribution and reservoir quality as well as highlighting mismatches between SHM and resistivity-derived water saturation (Sw). Given that some reservoirs (Figure 4.2, shoreface bars labeled as 1 and 4) display higher Sw than other shoreface bars and non-marine reservoirs in general, there is a good opportunity to evaluate imbibition SHM.

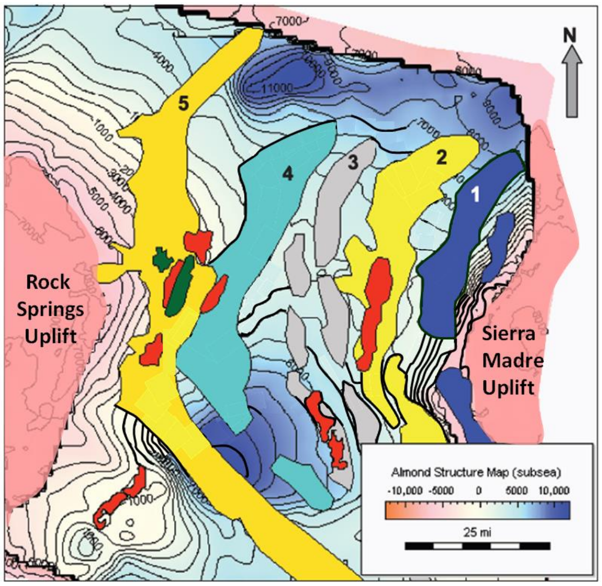

Figure 4.2: Upper Almond shoreface bars superimposed on the present-day structure (modified from Tobin et al., 2010).

The objective of this study is to analyse a comprehensive dataset of lab measurements for deriving robust drainage and imbibition SHM. When modelling imbibition, I overcome limitations of the mercury extrusion tests at low capillary pressures by combining them with trapped gas saturation using counter-current imbibition tests. I also test the dependency of SHM parameters on petrographic attributes of the rock. SHM are tested in tens of wells and relevant observations are discussed.

## 4.3 SATURATION-HEIGHT MODELS

The generation and implementation of saturation-height models (SHM) involves a series of steps which are sequentially described in this section. The overall workflow starts with converting capillary pressure tests to the right fluid system and in-situ reservoir conditions. Subsequently, composite drainage and imbibition capillary pressure curves (CPc) are constructed by combining the best attributes of each SCAL test. Finally, water saturation models (i.e., Thomeer) are used to fit parameters such as entry pressure, geometric factor and irreducible water saturation to CPc on a sample-by-sample basis.

### 4.3.1 Prerequisites

A robust resistivity-derived water saturation model (Rt_Sw) is commonly used as a reference for SHM. Merletti et al. (2013) offered a revision of each parameter that goes into the Rt_Sw calculation and placed emphasis in the water salinity uncertainty.

In non-marine reservoirs, the formation water salinity is below 10K ppm NaCl equivalent and its variability is relatively low. However, water salinity in shallow marine reservoirs is above 40K ppm NaCl equivalent and variable. This is mitigated by the use of electrical resistivity measured from Upper Almond-only produced water. The sampling was from wells with significant volumes of water production to minimize the effect of dilution by water condensed from produced gas.

The second prerequisite is the availability of a comprehensive special core analysis (SCAL) program designed to characterize each of the DFA. The program included ambient high-pressure mercury injection (HPMI) and centrifuge capillary pressure, stressed multi-cycle mercury injection and extrusion, and determination of maximum trapped gas. Three stressed mercury extrusion cycles were programmed at non-wetting phase saturations of 40%, 60% and the one corresponding to the maximum achieved injection pressure (Figure 4.3). The counter-current imbibition (CCI) test was used to assess maximum trapped or residual gas (Sgt-max).

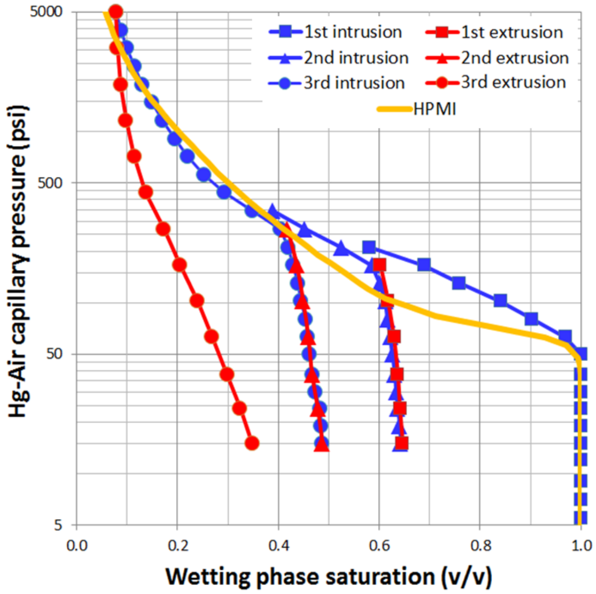

Figure 4.3: Example of ambient HPMI and stressed multi-cycle intrusion and extrusion capillary pressure acquired in one of the core plugs.

Thin-section petrography was performed on each sample to understand variations of rock frame composition, type and amounts of cement and porosity.

#### *4.3.1.1 Conversion of Lab to Reservoir Conditions.*

The HPMI and stressed multi-cycle capillary pressure tests went through the following:

a. Conversion of injection pressure from air-mercury to air-brine:

$$Pc_{a/b}{}^{lab} = Pc_{a/m}{}^{lab} \cdot \frac{IFT_{a/b}{}^{lab} \cdot \cos\theta_{a/b}}{IFT_{a/m}{}^{lab} \cdot \cos\theta_{a/m}} =$$

$$Pc_{a/m}{}^{lab} \cdot \frac{72 \cos 0°}{480 \cos 140°} = -0.196 Pc_{a/m}{}^{lab}$$

where Pc is capillary pressure at lab conditions, IFTlab is interfacial tension at lab conditions, Θ is contact angle and subscripts a/b and a/m represent air-brine and air-mercury fluid systems respectively.

b. Correction of non-wetting phase by clay-bound water (CBW):

Core plugs were dried at 116°C in a normal convection oven to remove movable, capillary-bound water and CBW. To restore the volume occupied by CBW, we use this equation (Juhasz, 1979):

$$Sw_{nwp}{}^{CBW_{corr}} = Sw_{nwp} \cdot \frac{\emptyset_e}{\emptyset_t}$$

$$Sw_{wp}{}^{CBW_{corr}} = 1 - \ Sw_{nwp}{}^{CBW_{corr}}$$

where, SwwpCBWcorr is the pseudo-wetting phase saturation (water) corrected by CBW, Swwp is the total pseudo-wetting phase saturation, Øt is total porosity and Øe is effective porosity. Øt is computed from nuclear magnetic resonance (NMR) data whereas Øe is computed as Øt minus the volume represented at 2.8 milliseconds in the NMR cumulative porosity distribution (Straley et al., 1994; Martin and Dacy, 2004).

c. Conversion of air-brine capillary pressure to reservoir conditions.

$$Pc_{a/b}{}^{res} = Pc_{a/b}{}^{lab} \cdot \frac{IFT_{a/b}{}^{res} \cdot \cos\theta_{a/b}}{IFT_{a/b}{}^{lab} \cdot \cos\theta_{a/b}}$$

$$Pc_{a/b}{}^{res} = 0.653 \cdot Pc_{a/b}{}^{lab}$$

where lab and res superscripts represent ambient and in-situ conditions. I interpret that these rocks remain strongly water-wet both in lab and reservoir conditions; therefore default contact angle values of 0° used in the lab are applied to in-situ conditions. The IFTa/bres parameter is taken from experimental measurements of IFT at various formation pressure and temperature by Jennings and Newman (1971). At the average formation pressure of 5,600 psi and temperature of 195°F, the interpreted gas-water IFT is around 47 dynes/cm (Rushing et al., 2008).

### 4.3.2 Primary Drainage

Mercury intrusion and drainage centrifuge capillary pressure tests reproduce the initial hydrocarbon charge of reservoirs. The pore-filling water is displaced as the lower density hydrocarbons migrate to the top of the reservoir. The accumulation of hydrocarbons exerts a buoyancy pressure determined by the vertical thickness of the hydrocarbons and the density contrast with the pre-existing reservoir water. This increased pressure expels water from the pore space and equilibrium is achieved when the buoyancy pressure equals the capillary pressure.

#### *4.3.2.1 Composite Capillary Pressure (CPc)*

Figure 4.4 displays of the approach taken for building Drainage CPc from SCAL data. We combine the first and second stressed mercury intrusions tests (yellow and orange circles) with the centrifuge capillary pressure (green triangles) when wetting phase saturations are lower than 40%. Notice how the CBW-corrected stressed mercury injection at the 3rd intrusion differs from the centrifuge capillary pressure at low wetting phase saturations. This could be evidence of capillary-bound water and dead-end pore space not associated with clay content. Even though centrifuge capillary pressure is recorded at ambient conditions, this test provides a more accurate representation of the irreducible wetting phase saturation than mercury injection tests. Notice that the largest difference between the ambient and stressed mercury injection tests is at low capillary pressure and negligible differences are expected at low wetting phase saturations (Chierici et al., 1967).

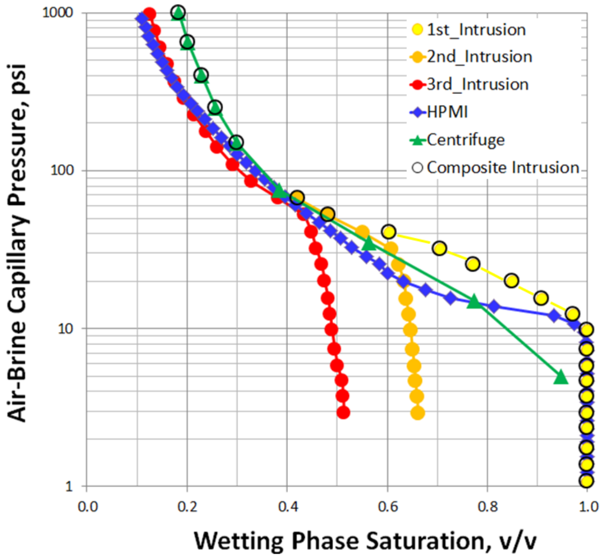

Figure 4.4: Capillary pressure data used to build composite drainage curves.

#### *4.3.2.2 Curve Fitting and Correlation with Petrophysical Properties*

A Thomeer (1960) water saturation model was used to fit parameters such as irreducible water saturation (Swirr), entry pressure (Pe) and geometrical factor (G) to the CPc curve. The fitting exercise is implemented using a Generalized Reduced Gradient (GRG) nonlinear algorithm embedded in a spreadsheet application. These parameters derived are correlated to the porosity (Ø) and permeability (Kk) measured in the same core plug; $\sqrt{Kk/\emptyset}$ is also correlated against Thomeer's parameters. It is a common practice to perform individual correlations by petrophysical rock types. We found better correlations when parameters are sorted by DFA as a continuum across all rock qualities. Figure 4.5 shows Thomeer's parameters in the y-axes and the petrophysical properties showing the highest correlation coefficient in the x-axes. Two equations are derived, one for shoreface and delta samples and another one for fluvial and coastal plain samples. Notice that Swirr can take negative values when $\sqrt{Kk/\emptyset}$ is less than 2.5. This effect is caused by continuing desaturation in the high capillary pressure range (Figure 4.4). When data points are fitted by SW models, the asymptote is reached at negative Swirr values. This means that the SW model is inaccurate at high capillary pressures.

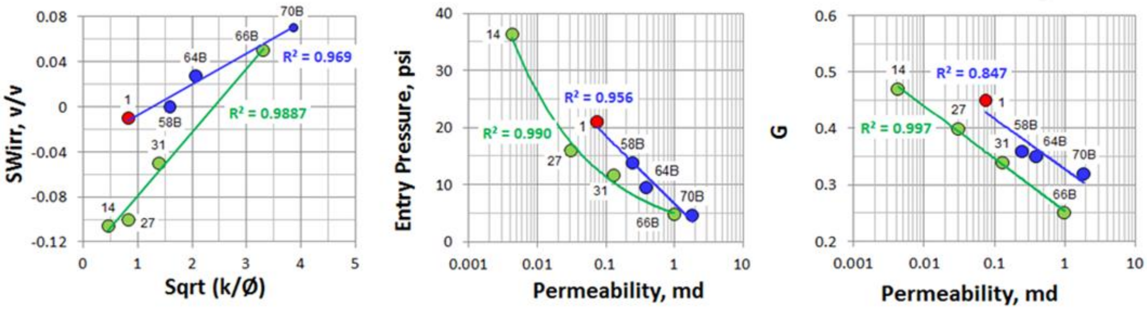

Figure 4.5: Trend lines used to reproduce Thomeer's parameters from petrophysical properties. Red, blue and green colors correspond to delta, shoreface and coastal plain/fluvial samples respectively.

The saturation-height model is given by the expression below, where Swshm is the water saturation at some height above the free water level (HAFWL), given gas and water specific gravities (SGg and SGw respectively):

$$Sw^{shm} = Sw_{irr} + (1 - Sw_{irr}) \cdot \left(1 - e^{\frac{G}{log(Pe/Pc)}}\right)$$

$$Pc = HAFWL \cdot (SGw - SGg) \cdot 0.433$$

### 4.3.3 Primary Imbibition

The lack of sealing capacity or the tilting of the trap can cause imbibition of water into the previously gas saturated reservoir. The point at which imbibition starts is called initial water saturation (SWi) and can either equal SWirr or be at higher SW values if reservoirs were in a fluid transition zone. As shown in Figure 4.1, this is the first end member of the imbibition curve. Our modelling approach assumes that reservoirs were fully charged with hydrocarbons and they went through a primary imbibition from the SWirr condition.

Adams (2003) described the “imbibition from drainage or IFD” approach in which imbibition capillary pressure curves are described as a function of their drainage capillary pressure curve precursors. Other authors (i.e., Seth et al., 2013) have successfully implemented the IFD approach in their working reservoirs. In this paper, we combine mercury extrusion capillary pressure curves with counter-current imbibition (CCI) tests (Pickell et al., 1966) to generate imbibition saturation-height profiles. We understand that non-extruded (trapped) mercury might not be an accurate representation of in-situ residual gas saturations and perhaps gas saturations at low capillary pressures.

#### *4.3.3.1 Trapped Gas*

Trapped gas saturation is the second end member of the imbibition curve (Figure 4.1) and its accurate determination is the key to characterize the SW state. As previously introduced, trapped gas remains after the displacement of mobile gas by water encroachment into the reservoir. The importance of recognizing trapped gas saturation is that under current reservoir conditions, the gas is immobile. A similar gas volume occurring from primary drainage may still be economically producible.

Dacy (2010) stated that for rocks with significant microporosity, mercury trapping usually exceeds gas trapping due to absence of a rapid-gas-diffusion. This mechanism, described by Jerauld (1996), takes place at gas-liquid interfaces in small pores with high capillary pressure. Figure 4.6A shows in the x-axis the maximum trapped gas saturation (Sgt-max) interpreted from the CCI tests and in the y-axis the Sgt interpreted from the mercury extrusion tests.

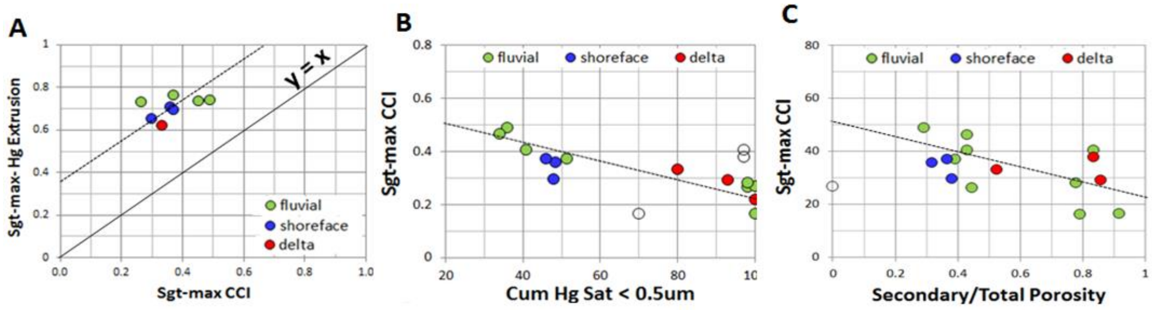

Figure 4.6: Overestimation of Sgt-max by mercury extrusion tests; (B) high cumulative mercury saturation in micro-porosity is associated with low CCI Sgt-max; (C) high secondary porosity is associated to equal or low Sgt-max.

The figure demonstrates that the latter consistently overestimates Sgt-max in these microporous Almond core samples. Figure 4.6B shows a correlation between cumulative mercury saturation below 0.5 microns and the CCI Sgt-max. Notice how high cumulative saturations associated with microporosity are correlated to low CCI Sgt-max values.

In a conventional rock system, reservoirs experiencing secondary porosity due to grain dissolution would have a high pore-body to pore-throat aspect ratio and therefore a high Sgt-max. Figure 4.6C demonstrates that samples having the largest proportion of secondary porosity display either similar or lower Sgt-max values than samples with small or moderate secondary porosity. This indicates that the conventional aspect ratio concept has little applicability in this type of rock with multiple pore types.

The CCI lab test starts with the core sample at the fully-dried condition; namely, the initial gas saturation (Sgi) equal to unity. Land (1968) and Jerauld (1996) offer empirical models for deriving trapped gas saturation (Sgt) from Sgi and Sgt-max; their models state that:

$$Sgt^{Land} = \frac{Sgi}{1 + Sgi \cdot \left({}^{1}/_{Sgt-max} - 1\right)}$$

$$Sgt^{Jerauld} = \frac{Sgi}{1 + \left({}^{1}/_{Sgt-max} - 1\right) .\ Sgi^{(1/(1-Sgt-max))}}$$

Dacy (2010) reported that Jerauld's equation tends to match clastic reservoirs whereas Land's equation tends to match carbonate reservoirs. In order to validate alternative models, we measured Sgt at three different Sgi in one of the core samples. Since experimental data plot approximately half way between the models (Figure 4.7), an average model is taken as the most representative of Almond reservoirs. Sgi is computed in each of the samples assuming that Sgi equals to one minus the Swirr interpreted for drainage saturation-height models. This allows the modelling of reservoirs going through imbibition after they were fully charged with hydrocarbon. In this study, we do not intend to model imbibition in partially charged reservoirs.

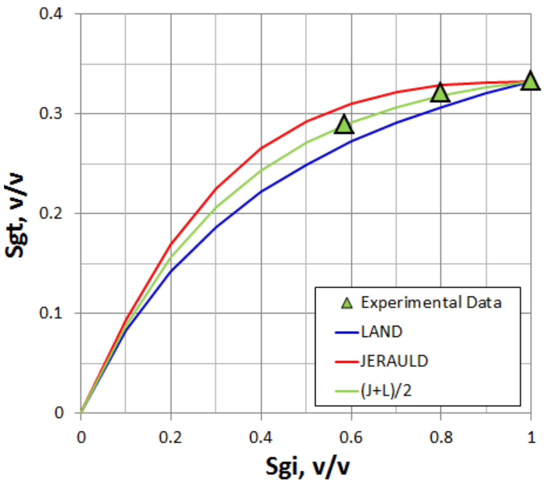

Figure 4.7: Experimental data show that an average between Jerauld and Land models is appropriate for Almond samples.

### *4.3.3.1 Modeling Approach and Correlation with Petrophysical Properties*

The Brooks-Corey's Sw model (1964) for drainage is modified to characterize primary imbibition. The wetting phase saturation, Sw, is linearly rescaled between the boundaries of experimental data; namely between Swirr and Swgt as shown in Figure 4.8A. Swgt represents the water saturation at trapped gas.

$$Swgt = 1 - Sgt$$

The rescaled parameter is called normalized water saturation (Swn) and is derived as follows.

$$Swn = \frac{Sw - Sw_{irr}}{Swgt - Sw_{irr}}$$

Subsequently, experimental data are fitted using the following hyperbolic function:

$$\mathrm{Pc} = \mathrm{A} \cdot \mathrm{Swn}^{-\mathrm{B}}$$

where A is the capillary pressure at Swgt and B is the curvature of the function. Figure 4.8B displays an example of the fitting procedure. In this case, data below 30 psi capillary pressure are disregarded as they depart from the power trend. Combining the two equations above, Sw is derived as follows.

$$Sw = \left(\frac{Pc}{A}\right)^{-1/B} \cdot (Swgt - Sw_{irr}) + Sw_{irr}$$

Figure 4.8C displays an example of the composite capillary pressure curve that fits CCI-derived Sgt and mercury extrusion data above a threshold capillary pressure value which tends to increase as the rock quality degrades.

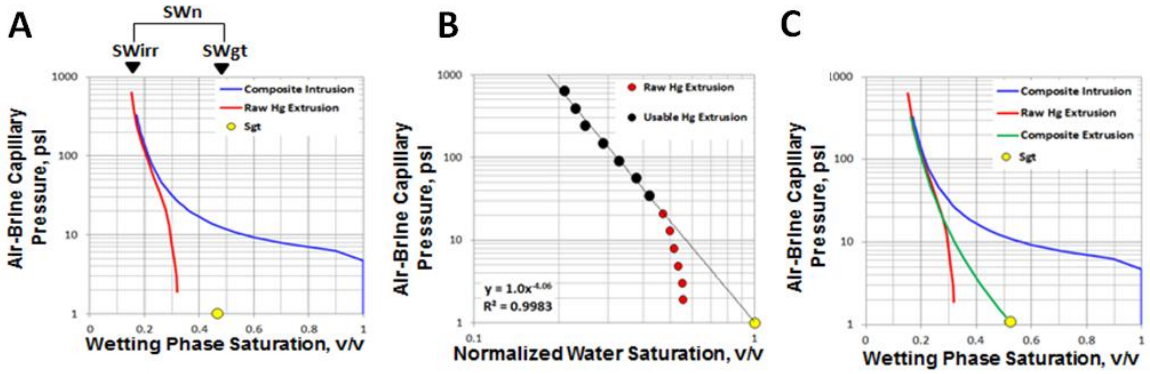

Figure 4.8: Procedure to combine mercury extrusion tests and CCI-derived Sgt to get composite extrusion curves.

The interpreted parameters Swirr, Sgt and B for eight core plugs are correlated to porosity (Øt), permeability (Kk) and squared root of Kk/Ø. As when modelling drainage, better correlations are found when parameters are correlated by depositional and diagenetic facies as a continuum across all rock qualities. Figure 4.9 shows modified Brooks-Corey's parameters in the y-axes and the log-derived property displaying the best fit in the x-axis. Blue and red circles correspond to shoreface and deltaic facies respectively whereas green circles are samples from coastal plain facies.

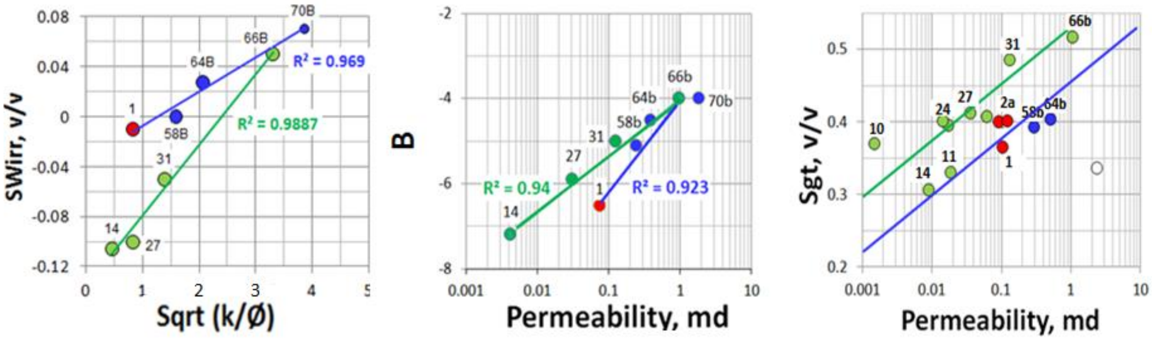

Figure 4.9: Correlations between modified Brooks-Corey's parameters and petrophysical properties.

### 4.3.4 Preliminary Results

The correlations between Thomeer and modified Brooks-Corey models against petrophysical properties in core plugs (Figures 4.5 and 4.8) are used to reproduce SHM from the log-derived porosity and permeability. The FWL for primary drainage and primary imbibition models was optimized by matching SHM in reservoirs free of resistivity shoulder bed effects (>6-feet thick). In other words, this matching exercise assumes that Rt_Sw is a useful reference for flagging intervals with anomalous SW distributions with depth.

Figures 4.10 through 4.12 display representative examples of common observations; tracks on the right-hand side show the match between the reference Rt_Sw against drainage and imbibition saturation-height models (Dra_SHM and Imb_SHM respectively). Figure 4.10 shows a fairly good agreement between the reference and the drainage model (track #5) in the lower interval whereas the imbibition model (track #6) works better in the upper interval. Alternatively, a drainage model with a 600-feet shallower FWL offers a reasonably good match (track #7).

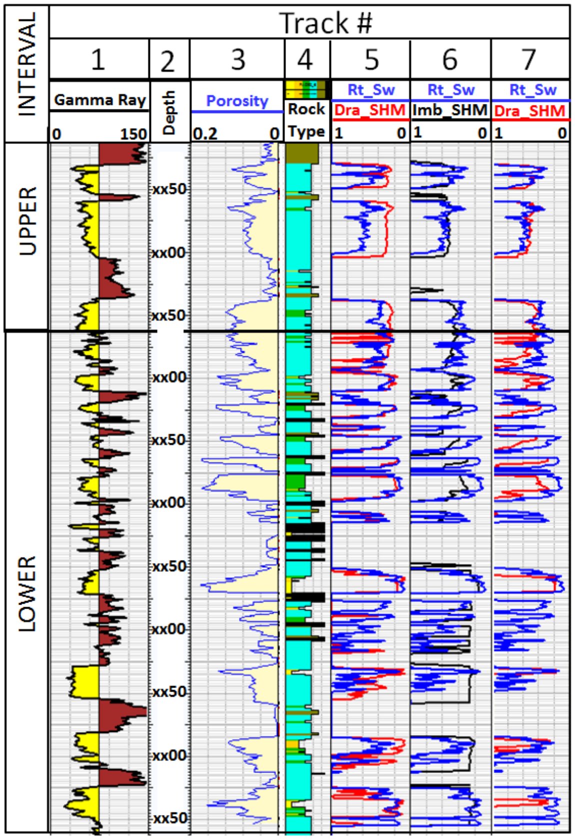

Figure 4.10: First example of matching exercise between reference (blue), drainage (red) and imbibition (black) SW models in tracks 5 thru 7.

Figure 4.11 is another well exhibiting a similar pattern. In this case, almost the entire formation can be fitted by the drainage model (track #5). Only the uppermost 40 feet of the sand package, referenced as upper interval, can be equally better fitted with an imbibition model (track #6) or a drainage model considering 400-feet shallower FWL (track #7).

Figure 4.12 displays another fair match of the reference against the drainage model for the lower interval (track #5). However, the imbibition and drainage models with shallower FWL do not yield similar results. In this case, the imbibition model (track #6) offers a remarkable good fit against the reference SW but an alternative drainage model using a 400-feet shallower FWL fails to provide a feasible solution (track #7).

The heterolithic character of reservoirs and the rock quality variations over small vertical distances make the saturation matching exercise quite challenging. The accuracy of the interpreted FWL is around a couple of hundred feet; in other words, a fair match between the reference and the SHM can be achieved using a FWL within that depth range.

A common FWL depth can only be used in wells located within a few miles of each other; the reason is the source-reservoir configuration.

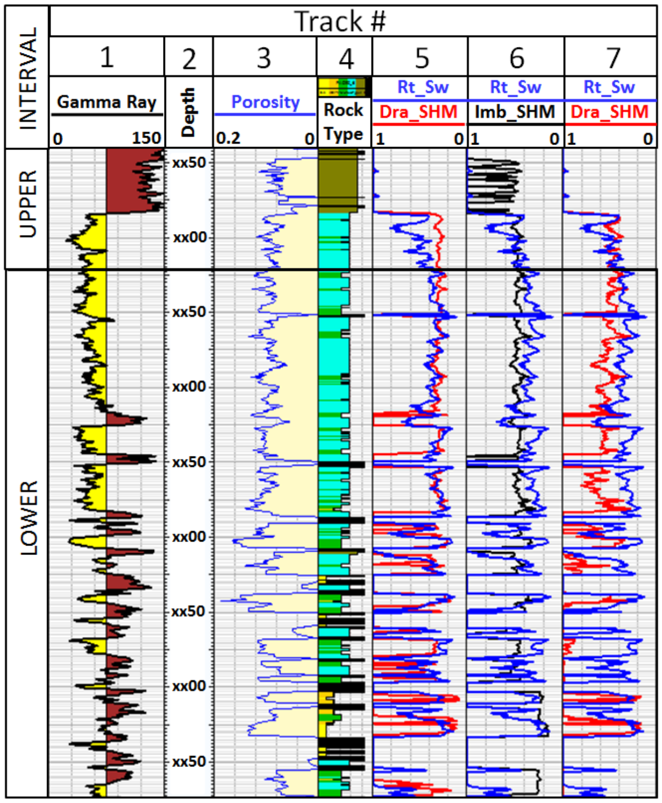

Figure 4.11: Example where most of the well can be fitted by a drainage model (track #5).

The reservoirs were mostly charged from source rocks, displayed as black bars in track #4 at Figure 4.10 to 4.12. The generated hydrocarbon migrated upward and filled shoreface and back-barrier facies in the Upper Almond; it also migrated downward and filled coastal plan and fluvial facies in the Lower Almond. The mechanism by which uppermost shoreface deposits resulted in higher SW than the rest of the reservoirs remains unclear. One possibility is that they were fully charged with hydrocarbon (primary drainage) and the trap subsequently leaked (primary imbibition).

Figure 4.2 shows the proximity of Upper Almond shoreface bars labelled as 4 and 5 to Rock Springs outcrops; near-surface faulting could have leaked hydrocarbon to surface through back barrier sandy facies. Since intervals with high SW are toward the top of shoreface bars, another possibility is that they were not fully charged and display shallower FWL than other facies closer to source rocks. These facies are highly compartmentalized by coals, shales and carbonate cemented layers that could explain either of the two possibilities described above; that is, heterogeneity could have prevented reservoirs from being entirely imbibed by water when the trap leaked or fully charged with hydrocarbon under primary drainage. The number of wells analysed so far allows us to present alternative explanations, but definitive conclusions will require a field-wide modelling of water saturation using the described alternative exercises.

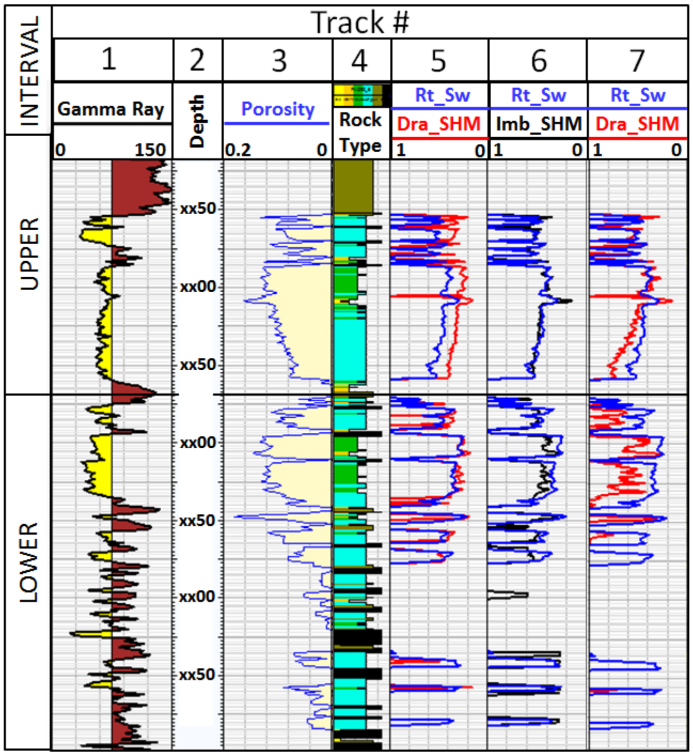

Figure 4.12: Example where the imbibition model (track #6) works better in the upper interval and the lower interval is best fitted by a drainage model (track #5).

## 4.4 CONCLUSIONS

The use of fluid pressure measurements and resistivity-derived water saturation models to predict a FWL depth often have limited applications in reservoirs experiencing several cycles of drainage, imbibition, re-drainage and re-imbibition. However, the Almond formation at the Wamsutter field presents some characteristics that make a saturation-height modelling exercise worthwhile. For instance, the subsurface structure remained unchanged from Eocene time (onset of hydrocarbon charge) and the trap model has a strong stratigraphic component.

Composite drainage capillary pressure curves are built by combining the first and second stressed mercury intrusions with the centrifuge capillary pressure when wetting phase saturations are lower than 40%. The fact that CBW-corrected stressed mercury injection differs from the centrifuge capillary pressure at low wetting phase saturations could be evidence of capillary-bound water and dead-end pore space not associated with clay content.

An imbibition SHM based on mercury extrusion might yield an inaccurate representation of SW near the imbibition FWL. We present a practical way to combine stressed mercury extrusion tests with CCI-derived Sgt-max when building the imbibition SHM. Trapped gas saturation is perhaps the most important parameter in the construction of imbibition SHM. It was demonstrated that samples having the largest proportion of secondary porosity display either similar or lower Sgt-max values than samples with small or moderate secondary porosity. The conventional aspect ratio concept has little applicability in this type of rock with mixed pore types.

The heterolithic character of reservoirs and the rock quality variations over small vertical distances make the saturation matching exercise quite challenging. The accuracy of the interpreted FWL is two hundred feet. Assuming that reservoirs were fully charged with hydrocarbon, the drainage SHM is key for flagging departures from the expected rock quality-dependent SW. Preliminary observations in tens of wells show that the reference resistivity-derived SW can be fitted by drainage SHM in the majority of the Almond section. Some upper Almond shoreface bars display anomalously high SW which could be explained by imbibition of water due to trap leaking or by reservoirs being not fully charged.

Initial observations upon implementation of SHM in the log domain encourage us to apply the water saturation models to other parts of the field. Interpretations of saturation states will be coupled with petroleum system models to produce a reliable saturation history of reservoirs.

# CHAPTER 5: STRATIGRAPHY AND SEDIMENTOLOGY OF THE UPPER ALMOND

## 5.1 ABSTRACT

Marine shoreline transgressions have been debated for the last six decades, and their most intriguing aspect is that transgressive ravinement often removes evidence of the shoreline itself, until there is turnaround to regression. This high-resolution chronostratigraphic study of an overall transgressive coastline, documented with over 1,450 wells with high quality petrophysical logs over an area of 6,200 km$^2$, defines the fundamental geobodies as a series of 15 elongate sandstone units stacked into 6 reservoirs. Mapping of the lateral extent and vertical stacking of the individual sandbodies shows that there was a spectacular and westward rising of back-stepping barrier spits, sourced by long-shore currents mobilizing sand from a delta to the north.

Each fundamental barrier spit unit (BSU) is a 6 to 12 meters thick, regressive, southward elongate and narrowing sandbody generated by longshore drift of sandy sediment. Internally, each BSU is composed of accretion sets with variable preservation of mud drapes. Each barrier and its related overlying transgression deposits is estimated to represent some 20-30Ky.

Strong transgressive ravinement events periodically flooded across the top of the barrier spits and shifted the deposition westward in 4 to 35 km steps. The westward transgressive-stepping across and into a structurally-generated embayment progressively dampened wave energy with each backstep. Morphologically, there were two endmember

sandbody types: 1) narrow and elongated, drum stick-like sandbodies built mostly by longshore accretion, i.e. true barrier bars, and 2) broader and more extensive regressive belts of sandstone that resemble strandplains. The former display typically longer backsteps across lagoonal areas whereas the latter show a more aggradational stacking arrangement which evidences a quasi-balance between accommodation and sediment supply.

There is no evidence of a smooth and continuous transgression controlling sandstone deposition and preservation. The clear alternation of long-term coastal retrogradation and short lived barrier spit development by longshore accretion and seaward progradation makes the "hybrid punctuated" transgression the most appropriate model for creating and preserving Upper Almond sandbodies. It is notable that the long-term, extensive transgression shown by the Upper Almond marks the onset of higher subsidence rates in the Western Interior Seaway and the onset of Laramide orogeny.

## 5.2 INTRODUCTION

The thickness and facies of transgressive deposits are controlled by the numerous factors influencing the shoreline retrogradation (Heward, 1981). The controlling factors, which include the rate of transgression and coastal morphology, yield different types of deposits over relatively short distances within the same sedimentary basin. Subtle changes in one or a combination of the controlling factors can substantially modify the characteristics of transgressive deposits (Cattaneo and Steel, 2002).

Several models have been proposed to explain the stratigraphic response to transgression, of which continuous and punctuated transgressions represent end members.

Continuous landward migration of the shoreline during sea-level rise leads to barrier shoreface retreat, whereas punctuated transgressions occur by alternation of coastal retrogradation and short progradational shoreline transits (regression) despite the overall landward-stepping of the shoreline.

This study aims to frame a range of transgressive deposits and their variability (e.g., thickness, lateral continuity, orientation) and compare and contrast the reservoir architecture and the formative sedimentary processes. The sandbodies of the Almond Formation are latest Cretaceous and developed in the Western Interior Seaway. The Campanian Almond Formation (Martinsen, 2003) in southern Wyoming probably represents one of the most extensive (300 km) and lengthy (1.7 My) transgressions in the stratigraphic record. Penetrated by thousands of wells and sampled by dozens of conventional cores, the upper section of the Almond Formation in the subsurface of southwest Wyoming presents a unique opportunity to understand transgressive mechanisms that form a range of reservoirs. Stratigraphic correlation and mapping documents three types of sandbodies within the overall transgressive succession, (1) sub-ravinement shorefaces that were sheetlike and as extensive as the prior shoreface progradation, (2) isolated (drowned in place) or ravinement-tip barrier bars at the transgressive-regressive (T-R) turnaround, both of which would be narrow and elongated parallel with the prior shoreline, and (3) supra-ravinement, thin transgressive sandstone lags or thick, tidal sand ridges that were also narrow and elongate but with variable orientation.

## 5.3 GEOLOGICAL SETTING

The study area lies in the eastern part of the Greater Green River Basin (GGRB) of southwestern Wyoming (Figure 5.1, dashed line). The GGRB is bounded on the north by the Wind River and Granite mountains and to the southwest by the Uinta Mountains, all of which are basement-involved compressional features (Erslev, 1993; Flores, 2003). The western boundary is the Sevier thrust belt, a series of thin-skinned, imbricate thrust sheets (Lageson and Smith, 1994; Morgan, 2003). To the east, the basin edge is defined by the Rawlins uplift and the Sierra Madre mountains (Otterman and Snoke, 2005).

Prior to the formation of the GGRB, this area had been part of a large-scale, Western Cretaceous Interior Seaway (WCIS) foreland basin, but this became broken up into sub-basins with intervening uplifts or arches by the late Cretaceous to early Tertiary Laramide tectonic activity (Dickinson et al.,1988; Morgan, 2003). The eastern part of the GGRB, where the Wamsutter field is located, is divided into three sub-basins.

The Great Divide Basin to the north and the Washakie Basin to the south are separated by the Wamsutter arch. The highest structural relief in the basin is the basement-cored Rock Springs Uplift (Stearns et al, 1975; Montgomery, 1996; Devlin et al., 1993), the fault-crest tip of an eastward-tilted Laramide block on which the Great Divide and Washakie sub-basins sit.

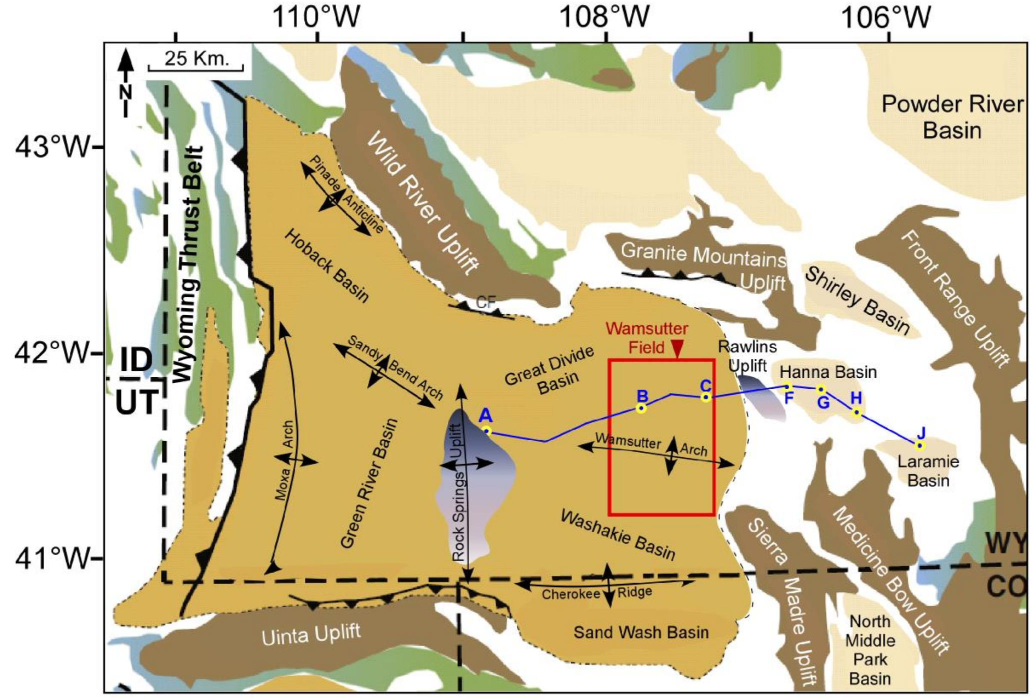

Figure 5.1: Location of the Wamsutter field and regional cross section connecting subsurface interpretation and outcrops (blue line). Modified from Roehler, 1992a, 1992b; Smith et al., 2008; Jagniecki et al., 2013; and Murphy Jr. et al., 2014.

The flanks of Rock Springs Uplift offer outcrop exposures of Almond strata along sections oriented oblique to depositional strike (Flores, 1978; Van Horn, 1979; Roehler, 1988; Martinsen and Christensen, 1992; Jackson and Rawn-Schatzinger, 1993; Schatzinger and Tomutsa, 1999 and Kieft et al., 2011). Tectonic loading at the thrust belt or increased Laramide structuring is thought to have increased subsidence at the end of the Ericson Formation deposition, setting up a much higher accommodation and lower sediment supply during the Almond formation (Devlin 1993; Liu et al., 2005). The lower part of the Almond Formation represents a continuation of the earlier Western Interior Seaway development, recording the initial late-stage retreat of the seaway, after a highly progradational Ericson Fm. tongue had reached as far east as the Laramie basin

(Martinsen et al., 1993). However, the late Campanian to earliest Maastrichtian strongly back-stepping upper part of the Almond Formation records the run-up of greatly increased subsidence rates of the overlying Maastrichtian Lewis Shale caused by prominent Laramide subsidence and block tilting (Carvajal and Steel, 2012).

Modest eustatic sea-level variations combined with reduced sediment supply and gradually increased rates of tectonic subsidence had produced a series of large-scale, regressive-transgressive depositional cycles within the Western Cretaceous Interior Seaway (Molenaar, 1983; Krystinik and Dejarnett, 1995). Superposed on the second-order Mesa Verde succession, third-order cycles are expressed as siliciclastic sediment wedges (Steel et al, 2012, their figure 17.18) that comprise alluvial plain, coastal plain, shallow-marine and shelf strata deposited along the western margin of the Seaway (Figure 5.2). The youngest part of this large-scale succession, based by a regional unconformity (73 Ma by Gill and Cobbam, 1973) and composed of the upper member (Canyon Creek Member) of the Ericson Formation, the overlying Almond Formation and the lowermost part of the Lewis Shale (Figure 5.2) This interval contains a series of higher frequency 4th-order regressive-transgressive cycles that are studied herein.

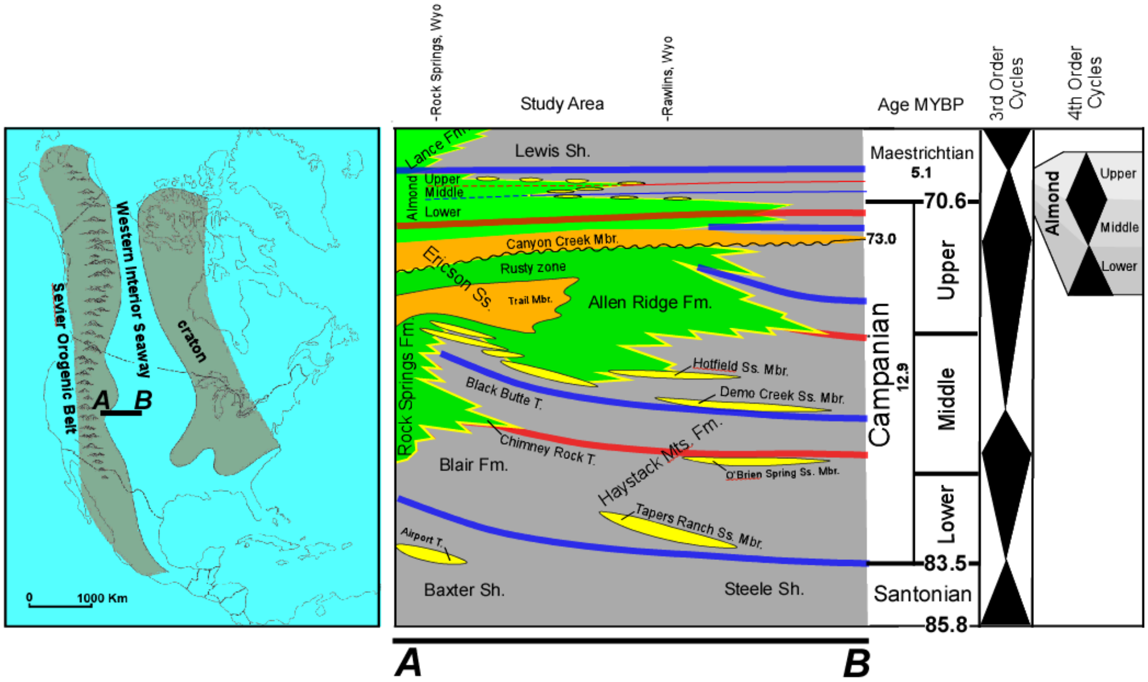

Figure 5.2: Left – schematic location map of the Western Interior Seaway. Right - an E-W cross section showing restored Upper Cretaceous across northern Utah and southern Wyoming (Modified from Roehler, 1990). Blue and red lines represent major transgression and regression surfaces respectively.

### 5.3.1 Paleogeography

In the area of southwest Wyoming (Figure 5.1) the late Almond transgression, although within a large-scale north - south oriented coastline, had produced a large, east-west elongate embayment (Figure 5.3) called the Hallville embayment by Lewis (1961) and the Rock Springs embayment by Roehler (1988). Most likely, the embayment formed in response to a localized high subsidence rate, possibly the result of tectonic loading in the Overthrust Belt causing local downwarping of the crust (Hendricks, 1983), or simply the strong localization of early Laramide subsidence between the twin uplifting bulwarks of the Uinta Mountains to the south and Wind River and Granite ranges to the north (Figure 5.3).

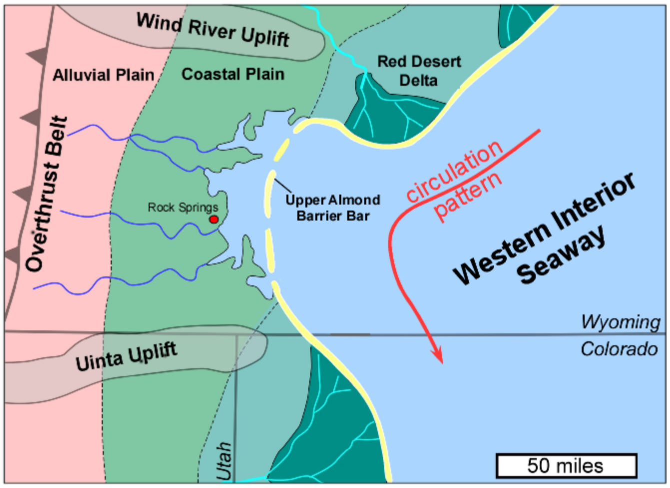

Figure 5.3: Early Maastrichtian paleogeography of the Upper Almond Formation (modified from Roehler, 1988).

Sediments entering the seaway through Red Desert Delta in the north of the Rock Springs bay (Figure 5.3) would have been caught up in the strong north-south oriented longshore current system and carried southward (Roehler, 1988; Sageman and Arthur 1994). A combination of decreased wave energy, increased tidal energy and the indentation of the shoreline in this part of western Wyoming caused the strandline to change from wave- dominated shoreface system to a wave-dominated, tidally influenced inlet dominated barrier island with an associated back-barrier lagoon. Minor fluctuations in subsidence rate, eustatic sea level, and sediment supply rate, both from longshore-feeding currents and from the Almond fluvial system that would have flowed from the west into the head of the embayment, would explain the alternating periods of lagoonal infilling, barrier progradation and transgressive back-stepping of the barrier system (Martinsen and Christensen, 1992). This is the object of further study herein.

### 5.3.2 Previous Work

The Almond Formation in the outcropping Rock Spring Uplift was divided into two mappable parts (Hale, 1950, Lewis, 1961, Jacka, 1965, Flores, 1978). An upper part consisting dominantly of sandstones of marine to brackish water origin (barrier beach, tidal inlet, tidal delta, and shoreface deposits), and a lower part consisting of interbedded coals, shales, siltstones and sandstones of continental and brackish water origin (fluvial channel, splay, overbank, swamp, fresh and salt water marsh, lagoon, tidal flat and tidal channel deposits). This division informally established the recognition of two members: upper and lower members of the Almond Formation in the Rock Springs Uplift area (Martinsen and Christensen, 1992). Van Horn (1979) further subdivided the lower Almond into lower and upper parts, resulting in a threefold division of the formation (Table 5.1). According to Van Horn (1979), the lower part of the Lower Almond contains exclusively nonmarine fluvial-related deposits. The upper part of the lower Almond, in contrast, records alternating fresh and brackish water conditions and consists of cyclical sequences of freshwater coals and brackish water carbonaceous shales, mudstones, siltstones and thin sandstones. Roehler (1988) also recognized a threefold subdivision of the Almond but did not relate his boundaries to the ones defined by other authors.

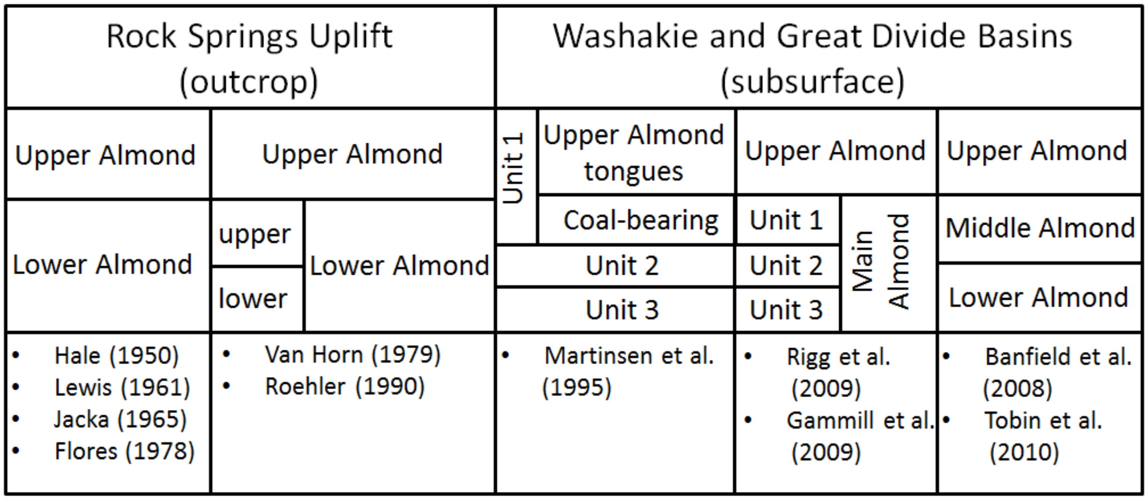

<table>
<tr><td colspan="3">Rock Springs Uplift (outcrop)</td><td colspan="5">Washakie and Great Divide Basins (subsurface)</td></tr>
<tr><td>Upper Almond</td><td colspan="2">Upper Almond</td><td rowspan="2">Unit 1</td><td>Upper Almond tongues</td><td colspan="2">Upper Almond</td><td>Upper Almond</td></tr>
<tr><td rowspan="3">Lower Almond</td><td>upper</td><td rowspan="3">Lower Almond</td><td>Coal-bearing</td><td>Unit 1</td><td rowspan="3">Main Almond</td><td>Middle Almond</td></tr>
<tr><td rowspan="2">lower</td><td colspan="2">Unit 2</td><td>Unit 2</td><td rowspan="2">Lower Almond</td></tr>
<tr><td colspan="2">Unit 3</td><td>Unit 3</td></tr>
<tr><td>• Hale (1950)<br>• Lewis (1961)<br>• Jacka (1965)<br>• Flores (1978)</td><td colspan="2">• Van Horn (1979)<br>• Roehler (1990)</td><td colspan="2">• Martinsen et al. (1995)</td><td colspan="2">• Rigg et al. (2009)<br>• Gammill et al. (2009)</td><td>• Banfield et al. (2008)<br>• Tobin et al. (2010)</td></tr>
</table>

Table 5.1: Subdivision of the Almond formation in outcrop and subsurface by various authors.

The extrapolation of upper and lower Almond nomenclature into the subsurface stratigraphy has also been common. However, what is designated as upper Almond varies laterally and is neither chronostratigraphically nor lithostratigraphically correlative with what is designated as upper Almond in the Rock Spring Uplift outcrops (McCubbin and Brady, 1969; Van Horn, 1979; VerPloeg et al., 1983; Weimer et al., 1982). Moreover, the upper Almond pinches out into Lewis Shale just to the east of the Rock Springs uplift, and thus is not present through most of the Washakie and Great Divide basins. For the most part, the Almond Formation within these basins is correlative to the lower Almond member of the Rock Springs uplift (Martinsen and Christensen, 1995).

In the eastern Washakie and Great Divide basins, Martinsen et al. (1995) divided the Almond into three genetic units (Table 1). Unit 1 includes the upper Almond marine sandstone tongues and a coal-bearing succession, Unit 2 consists of a series of coarsening-upward shale-to-sandstone shallow marine packages, and Unit 3 contains interbedded coal, shale, siltstone and sandstones deposited in a coastal-plain environment. Rigg et al. (2009) simplified the latter scheme by excluding the upper Almond from what they called Main Almond. Banfield et al. (2008) developed a regional chronostratigraphic model where the boundaries between Almond members are defined by turnarounds of the depositional system. The lower-middle Almond boundary was given by the maximum flooding surface that represents the maximum westward transgression across the Wamsutter field. The middle-upper Almond boundary was defined as the maximum regression surface representing the turnaround from regression to transgression.

### 5.4 CONCEPTUAL SEDIMENTATION MODELS

Studies of relict facies patterns of drowned continental shelf areas have revealed two mechanisms by which beaches and barrier islands migrate landward (Reading, 1986). The first accepted mechanism is termed “barrier” or “shoreface retreat” (Johnson, 1919; Brunn, 1962, Swift, 1968; Swift et al, 1970). The barrier/shoreface retreat model describes barriers that migrate continuously landward as sea level rises (Figure 5.4A). In doing so, the breaker zone erodes the barrier by transgressive wave-ravinement, causing the former barrier area to become entirely submerged (i.e., part of the offshore shelf). The model assumes that former back-barrier lagoonal sediments would become “exhumed” by erosion on the seaward side of the barrier, during the landward erosive transit of the breaker zone. Deposits of the barrier would occur only in the latest (maximum transgressive) position of the barrier before the shoreline reverted to regression. However, a modest thickness of reworked sediments would occur as transgressive lag deposits and sometimes thicker shelf sand ridges would develop above the ravinement surface because of wave/tide reworking of the exhumed back-barrier deposits (Snedden and Dalrymple, 1999).

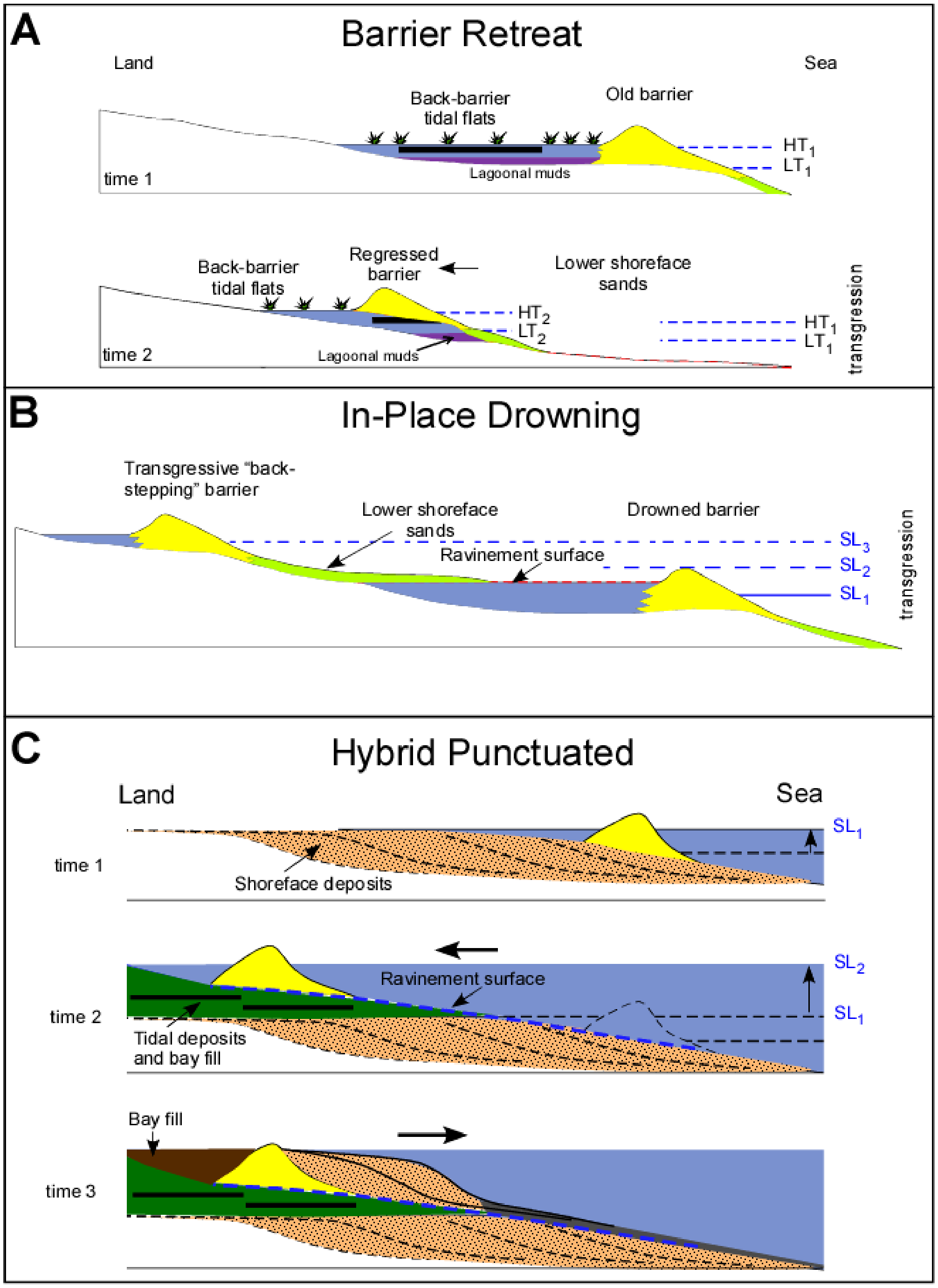

Figure 5.4: Mechanisms of barrier migration during transgression. Modified from Sanders and Kumar (1975) and Clifton, 2006)

Alternative models can be foreseen when the rate of sea-level rise is unsteady. The “in-place drowning” model (Kumar and Sanders, 1975) states that if sea level rises quickly, a barrier may remain in place, while the lagoon on its landward side deepens and widens (Figure 5.4B). Eventually, the breaker zone reaches the level of the top of the barrier dunes, the water drowns the barrier and the breakers then skip landward to form a new barrier along the landward edge of the former lagoon (Gilbert, 1885; Sanders, 1963). When barriers are drowned in-place, the surf zone does not pass continuously across the area; instead it moves across the track submerged in successive pulses. A third option, the “hybrid punctuated transgression” model considers the alternation of long-term coastal retrogradation and intervening, short term progradation (regression) resulting in the overall landward-stepping of the surf zone (Figure 5.4C). In the punctuated transgression model, most of the preserved deposits correspond to the regressive episodes which take place when sediment supply outpaces the accommodation. In this case, broad elongate (sheet-like) deposits are expected as opposed to the narrow-elongate ones generated either by barrier in-place drowning or by barrier preservation at transgressive-regressive turnaround.

### 5.4.1 Current Terminology

There is an overall consensus on the unsteady or discontinuous character of the long-term transgression in Almond times because the preserved sandbodies do not resemble the very thin and narrow deposits left behind by a continuous transgression, and because many of the sandbodies are clearly upward coarsening, implying regressive growth (Lewis, 1961; Weimer, 1965 and 1966, McCubbin and Brady, 1969; Roehler, 1988; Martinsen and Christensen, 1992; Hendricks, 1994; Lawrence, 2007 and Kieft et al., 2011). However, the connection between transgression mechanisms and the resulting architectural elements has not been discussed in detail by authors. There has been no clear distinction between terms such as “prograding barrier island” and “strandplain” when interpreting the Almond. The last term was sometimes conveniently avoided given the overall transgressive character of the formation, and the term ‘prograding barrier’ is simply incorrect, as barrier bars by definition are transgressive, except at their turnaround position where they are no longer a ‘barrier’.

Roehler (1988) provided the first model for barrier generation, growth and preservation for an Upper Almond shoreface bar (Barrier G at Rock Springs Coal Field). He proposed that the barrier shoreline prograded because of sediments supplied and swept southward by longshore currents while the lagoon behind the barrier expanded. Subsequently, a decrease in sediment supply resulted in the bar abandonment and transgressive ravinement obliterating both the surface expression of the bar and causing erosive removal of part of the underlying peat beds. Given the sandstone dimensions of Barrier G (60 miles long and 4 miles wide), the assumed transgression mechanism is in-place drowning. Lawrence (2007) used an extensive subsurface dataset to characterize three genetic units in the Upper Almond. He concluded that the sandbodies were back-stepping (transgressive) barrier islands which were juxtaposed with and overlie related back-barrier and coastal plain facies.

Hendricks (2009) reported that complete seaward-stepping (regressive) sandbodies were preserved below ravinement surfaces when the accommodation to sediment supply ratio inverted, changing gradually from low to high. The regressive half-cycles are more numerous in the western and northern parts of the Great Divide and Washakie basins. Kieft et al. (2011) interpreted at least nine vertically stacked regressive-transgressive cycles in the upper Almond around the Rock Springs Uplift. The regressive component consists of thick (up to 22m) strandplain or wave-dominated delta facies overlain by coastal plain deposits. The transgressive component of each cycle consists of one or more, thick (up to 18 m) and well-preserved bay-fill successions. These last two studies seem to fit what was previously described as "hybrid punctuated" transgression mechanism with a gradual switch between supply and accommodation dominance.

## 5.5 DATABASE AND METHODOLOGY

Over 8,500 vertical wells have been drilled in the Almond's Wamsutter field over the last 50 years (Figure 5.5). The Upper Almond interval, in the present study, was inspected on a well-by-well basis in areas of high drilling density (40-acre well spacing) and a subset of 1,300 representative wells were selected for petrophysical analysis, facies interpretation, stratigraphic correlation and depositional systems mapping. An additional set of 150 wells were selected in West Desert Springs, Desert Springs and Patrick Draw fields for correlating the subsurface data at the Wamsutter field with the Rock Springs Uplift outcrops (Figure 5.5).

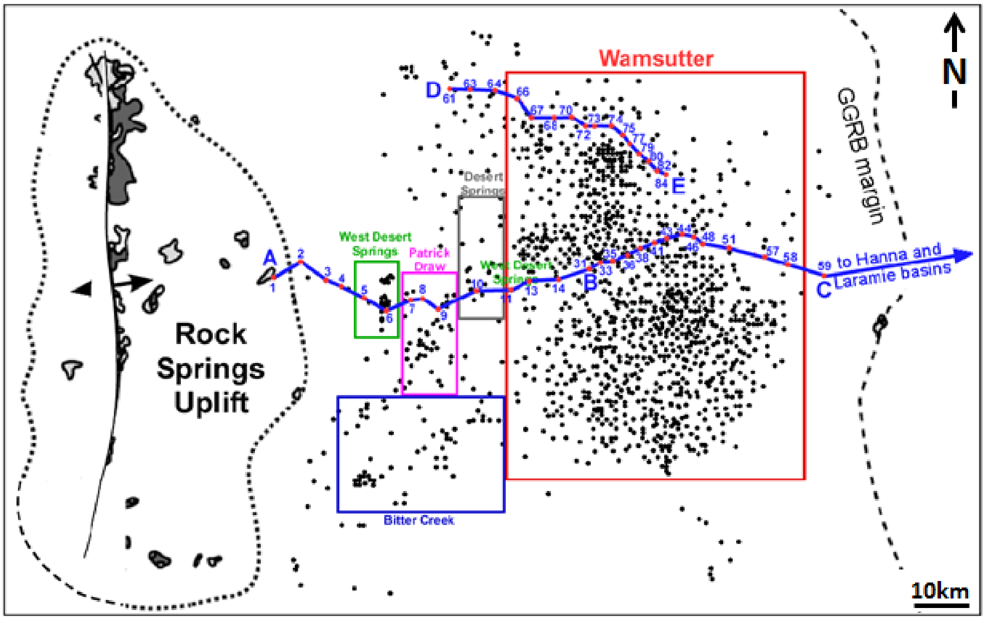

Figure 5.5: Base map showing the selected wells and reference cross sections for this study. Color boxes indicate different fields.

The open-hole logs acquired in selected wells include gamma ray (GR), bulk density (RHOB), neutron porosity (NPHI) and deep electrical resistivity (RDEEP). Forty three wells have high-resolution (HR) resistivity images and thirty two wells have whole core of variable footage and variable coverage.

Preceding rock analysis, well logs were quality controlled using caliper (CALI) and differential bulk density (DRHO) as proxies for washouts and borehole rugosity. Figure 5.6A displays typical raw logs across the Almond Formation. The petrophysical evaluation involves the interpretation of lithology, sand volume, total porosity, water saturation as well as absolute and relative permeability (Lieber and Miller, 2009; Merletti et al., 2013 and 2016). Using these properties, the interpretation of coals from RHOB and NPHI responses and total porosity from RHOB support the traditional GR-derived pick of sandbody boundaries (Figure 5.6B and 5.6C). Detailed facies models described in slabbed cores and HR resistivity images are commonly grouped into depositional facies associations (DFA) that can be confidently interpreted using basic log pattern recognition (Figure 5.6D).

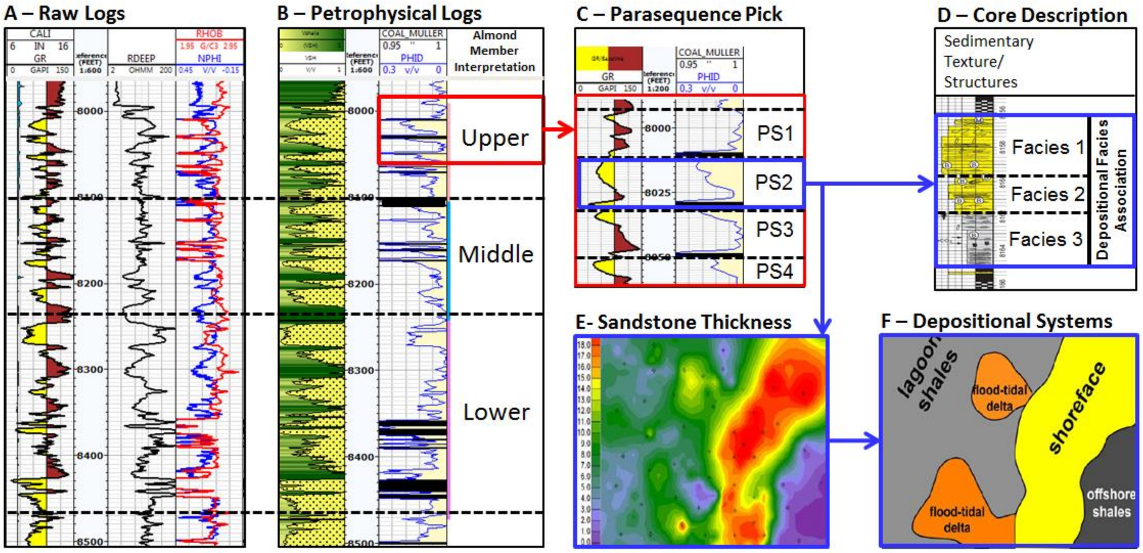

Figure 5.6: Methodology to interpret depositional systems from logs and core data

The depositional system (Figure 5.6F) is interpreted based on trends in sandstone percent maps (Figure 5.6E) and core-calibrated, log-based depositional facies. These maps are compiled to understand the spatial evolution of the shoreline through time. Table 5.2 details features that were used for inferring the transgression mechanisms. Diagnostic features include well-log pattern, facies, and sandbody width and relative orientation respect to shoreline.

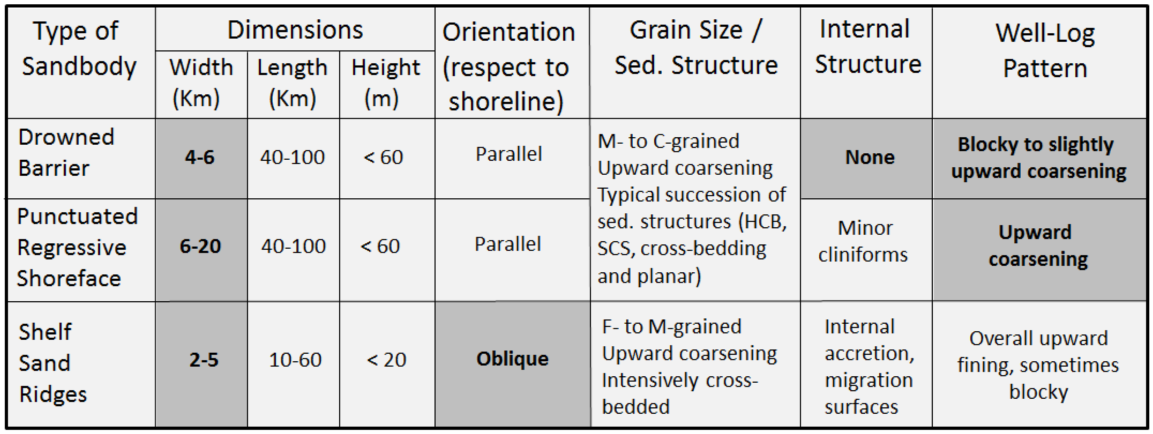

| Type of Sandbody | Dimensions | | | Orientation (respect to shoreline) | Grain Size / Sed. Structure | Internal Structure | Well-Log Pattern |
|---|---|---|---|---|---|---|---|
| | Width (Km) | Length (Km) | Height (m) | | | | |
| Drowned Barrier | **4-6** | 40-100 | < 60 | Parallel | M- to C-grained<br>Upward coarsening<br>Typical succession of sed. structures (HCB, SCS, cross-bedding and planar) | **None** | **Blocky to slightly upward coarsening** |
| Punctuated Regressive Shoreface | **6-20** | 40-100 | < 60 | Parallel | | Minor cliniforms | **Upward coarsening** |
| Shelf Sand Ridges | **2-5** | 10-60 | < 20 | **Oblique** | F- to M-grained<br>Upward coarsening<br>Intensively cross-bedded | Internal accretion, migration surfaces | Overall upward fining, sometimes blocky |

Table 5.2: Characteristic of sandbodies generated during transgressions; dark grey are diagnostic features.

## 5.6 RESULTS

### 5.6.1 Framework definition

The Almond Formation depositional facies and regional shoreline trends are shown in a 290Km long cross section that connect the Rock Springs Uplift in the west to the Hanna and Laramie basins in the east, via Wamsutter and other subsurface data sets (Figure 5.7). The well data in the cross section are flattened on a stratigraphic datum in the Lewis shale, a volcanic ash horizon informally called “Asquith marker”. This marker has been interpreted as associated with the condensed sedimentation interval, deposited during the maximum transgression of the Lewis Sea. The Asquith Marker is a reliable pick on logs, and is characterized by high gamma ray and resistivity log responses.

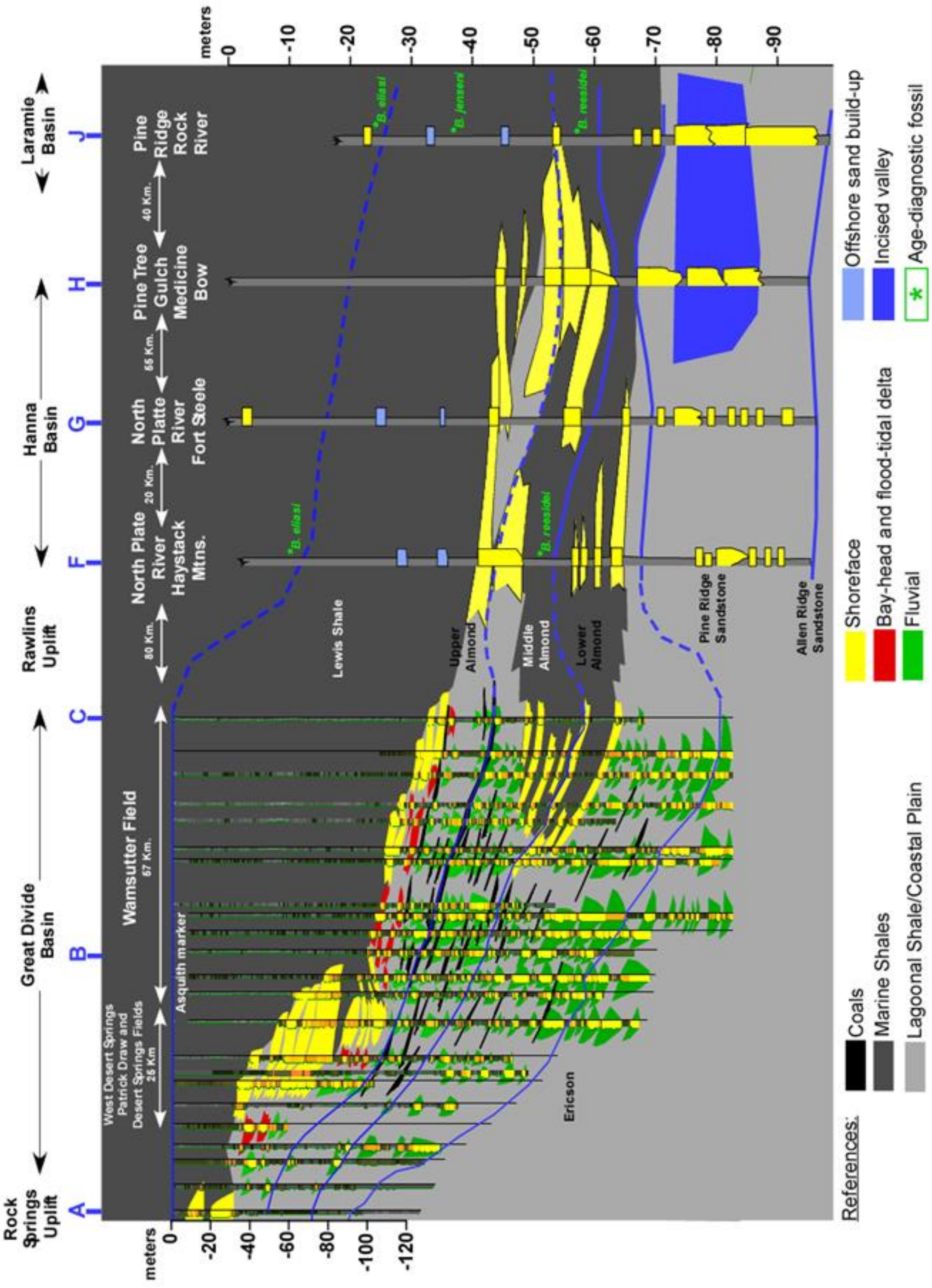

Figure 5.7: Regional Almond cross section connecting Rock Spring Uplift outcrops in the west to subsurface facies and to outcrops in the Hanna and Laramie Basins (modified from Martinsen et al., 1993) in the east. The location of the cross section is in Fig. 5.1.

The Almond to Lewis lithostratigraphic contact is placed at the uppermost sandstone below the Asquith marker. When captured in cores, this contact consists of a thin, highly bioturbated shaly sandstone, and is interpreted as a transgressive surface of erosion (Martinsen & Christensen, 1992). Below this transgressive surface of erosion, the main sandstones packages are not arranged chronostratigraphically and layer-cake equivalent; rather, they are stratigraphically higher and therefore younger to the west (Figure 5.7). Although the contact between the Almond Fm. and the overlying Lewis shale has historically been considered conformable (Gill et al., 1970; Van Horn, 1979), the above stratigraphic architecture indicates that this boundary is diachronous, becoming younger from east to west (Martinsen & Christensen, 1992).

The basal Almond contact with the underlying Ericson is consistently picked both in outcrop and in the subsurface in the western part of the basin. However, this pick becomes progressively less consistent toward the east in the Wamsutter field area. In the present study, the contact is picked where the section changes upward from a section of thick, amalgamated and channelized fluvial sandstones to a section of interbedded shale, coal and thin sandstones (Martinsen et al., 1995). Because sandstones in the lower Almond are commonly laterally discontinuous as individual channels, associated with coals, and fining-upward profiles on logs, they are distinguished from upper Ericson sands which generally lack coal and have very amalgamated and thick blocky sandstone patterns. Locally, amalgamated sands in the Lower Almond and shaly upper Ericson intervals make the picking of the contact more uncertain in the Wamsutter area (Figure 5.7).

The Almond base is associated with a maximum shoreline progradation level (maximum regression surface) in the east. Following this regression, the system turned around into a transgression (Banfield et al., 2008) and deposited the Lower Almond. The transgression records upward-coarsening, 2-3.5 m-thick sandstone units well developed in the eastern part of the Wasmutter field. The parasequences abruptly pass westwards into lower coastal plain deposits which can be laterally discontinuous (Figure 5.7). The lack of back-barrier facies (i.e. flood-tidal deltas) could be because of a relatively flat shoreline trajectory, with little (or no) transgressive deposits preserved (Helland-Hansen and Gjelberg, 1994). Such a non-accretionary transgression interpretation would suggest high rates of sea-level rise, a low-gradient topography being transgressed and negligible sediment supply to the shorezone during Lower Almond times.

The Lower to Middle Almond contact corresponds to a transgression-regression turnaround marked by a 4rd-order maximum flooding surface. At this time, the shoreline was located near the center of the Wamsutter field and the system began to prograde to the east (Figure 5.7). Middle Almond sandstone bodies are slightly thinner (2-3 m thick) than those of the Lower Almond. Similar to the Lower Almond, the eastern part of the Wamsutter field exhibits a strong shallow marine overprint whereas the western part displays exclusively coastal plain deposits with the largest proportion (thickness) of coals in the succession. It is likely that the aggradational shoreline trajectory promoted the deposition and preservation of peats.

The surface marking the top of the middle Almond was picked at the surface of maximum regression, marked by the most seaward (easterly) position of the shoreline (sensu Martinsen and Martinsen, 1993). Because this turnaround takes place to the east outside of the study area, the Middle-Upper Almond boundary is picked where the succession changes upward from a relatively thick (>2 m) and laterally continuous coaly interval to lagoonal shales (Figure 5.7). This coaly interval is interpreted to have formed during a more aggradational period, where there was a low rate of regression combined with rising relative sea-level. Under such conditions, the peat was able to accumulate to its maximum thickness for the longest period of time (McCabe and Parrish, 1992). Upper Almond sandbodies are composed of preserved strandplain and barrier island complexes (upper to lower shoreface, ebb and flood delta deposits) across the entire Wamsutter area, Desert Spring, Patrick Draw and Rock Springs Uplift. The thickest parasequences are recorded in the eastern part of the Wamsutter field where sandbodies can be as thick as 30 m (Figure 5.7). The lithostratigraphic top of the Almond in this study is marked by the uppermost Almond sandstone at any given location across the area.

### 5.6.2 Core Description of Shoreface Facies Association

The shoreface facies association is typically composed of very fine- to medium-grained, blocky to upward-coarsening sandstone-dominated successions which can be 8 to 30m thick. Individual depositional facies can be 0.2 to 2m thick and include massive (structureless) sandstone, rippled sandstone, planar and trough cross-stratified sandstone, parallel stratified sandstone, swaley cross stratified sandstone, intensively bioturbated sandstone, oyster-rich shaly sandstone and interbedded heterolithics. The occurrence and abundance of each facies, the type of contact (i.e., sharp vs. gradational) and the bioturbation index provide insights on the wave energy of the shoreline. Figure 5.8 displays the sedimentary description of a representative whole core in the Echo Springs bar. The sandbody is 7 meters thick, and shows a sharp base of bioturbation-free cross-bedded sandstone onto lagoonal siltstones. Upwards, there is an alternation of thickly bedded swaley and amalgamated sandstones with no apparent shale break. Overall, the individual bed thickness decreases upwards as bioturbation becomes pervasive close to the sandbody top. This core does not show evidence of a typical stacking of facies for prograding shorelines; instead it displays features of shallow marine reworked sandbodies.

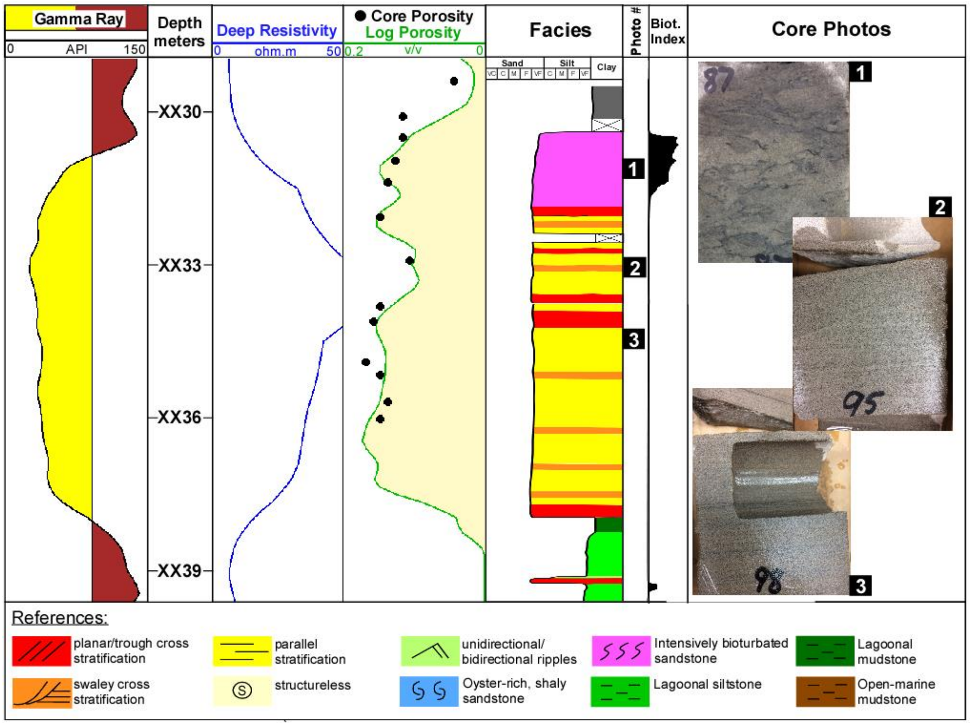

Figure 5.8: Depositional facies composing the "Shoreface Facies Association" in the Echo Springs bar. Photos correspond to "Intensively bioturbated sandstone" (1), "Swaley cross stratified sandstone" (2) and "Parallel stratified sandstone" (3) facies.

Figure 5.9 displays an example of the shoreface depositional facies association in the Siberia Ridge unit. The core shows an 8-meter fine to very fine grained sandstone deposited on top of siltstones of the Echo Springs' lagoonal environment. Facies pass (upward) from structureless and rippled sandstones to planar and parallel stratified sandstones. Toward the top, the sandstone is intensively burrowed and bioturbated. When compared to the core in the Echo Springs bar, this core displays less wave reworking as well as less evidence of shoreline progradation. Figure 5.10 displays a whole core in the West Wamsutter bar. The lower half of the core displays a monotonic alternation of very fine structureless to faint parallel stratified sandstones; the bioturbation index is high at the base and decreases toward halfway up the sandbody. There is an upward increase in bed thickness and in the occurrence of high wave energy intervals picked by planar tabular cross-bedded sandstones facies. Toward the top, there is oyster-rich, thinly bedded sandstone and an increasing of mud content upwards.

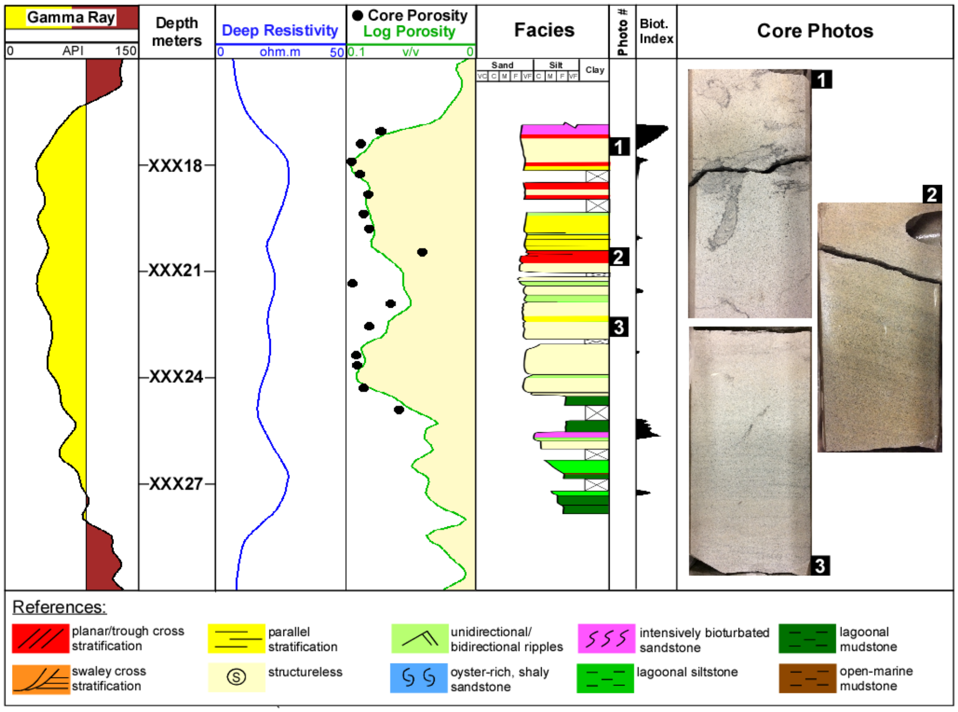

Figure 5.9: Depositional facies composing the “Shoreface Facies Associations” in the Siberia Ridge bar. Photos correspond to “Structureless sandstone” (1), “Planar cross-stratified” (2) and “Parallel stratified sandstone” (3) facies.

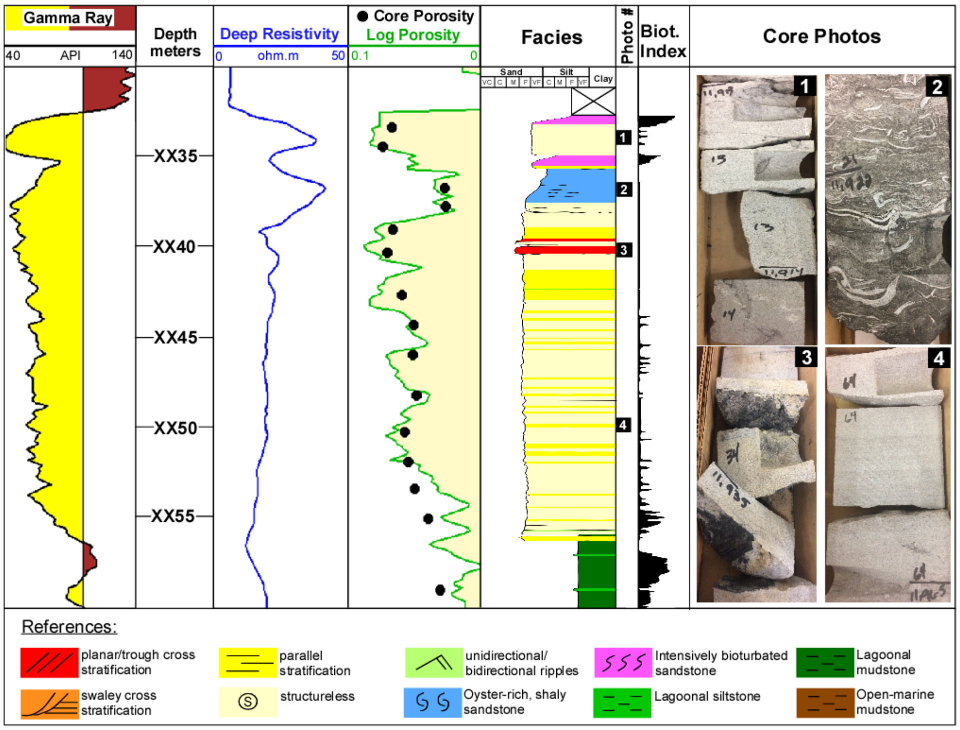

Figure 5.10: Depositional facies composing the "Shoreface Facies Associations" in the West Wamsutter bar. Photos correspond to "Structureless sandstone" (1), "Oyster-rich, shaly sandstone" (2), "Planar cross stratified sandstone" (3), and "Parallel stratified sandstone" (4) facies.

### 5.6.3 Mapping the Upper Almond Intervals

The boundary between Middle and Upper Almond is interpreted as the surface that reflects regressive-transgressive turnaround of the shoreline to the east of the study area (Figure 5.7). Since there is no well control to the east, the presence of coals in available data is used as a proxy for picking a surface of maximum regression.

The presence of coals in specific portions of transgressive-regressive cycles in the Upper Cretaceous of the Western Interior Seaway has been previously described (Sears et al., 1941; Weimer, 1960, Fassett and Hinds, 1971; Beaumont et al., 1971; Ryer, 1984). The most extensive and thickest coal layers are restricted to vertically stacked progradational events, which characterize transgressive and regressive maxima (Cross, 2012). Ryer (1981) studied the seaward-stepping Ferron Sandstone parasequences and observed that the most extensive and the greatest volume of coal is contained in events representing the end of the vertically stacked (aggradational) phase. The aggradation occurred when the accommodation in the coastal plain was at the maximum, but prior to the maximum rate of long-term sea-level rise that kicks off the landward stepping.

A 1.5 to 2.5 m-thick coal layer picked over the entire study area is formed at the end of the regression-transgression turnaround and the onset of backstep. Above a prominent coaly marker, the Upper Almond member is subdivided into 6 intervals; these include in order of deposition Basal Upper Almond, Fillmore Creek, Echo Spring, Siberia Ridge, Luman and West Wamsutter. Some of these names are borrowed from subsurface literature that describes intervals with producing reservoirs.

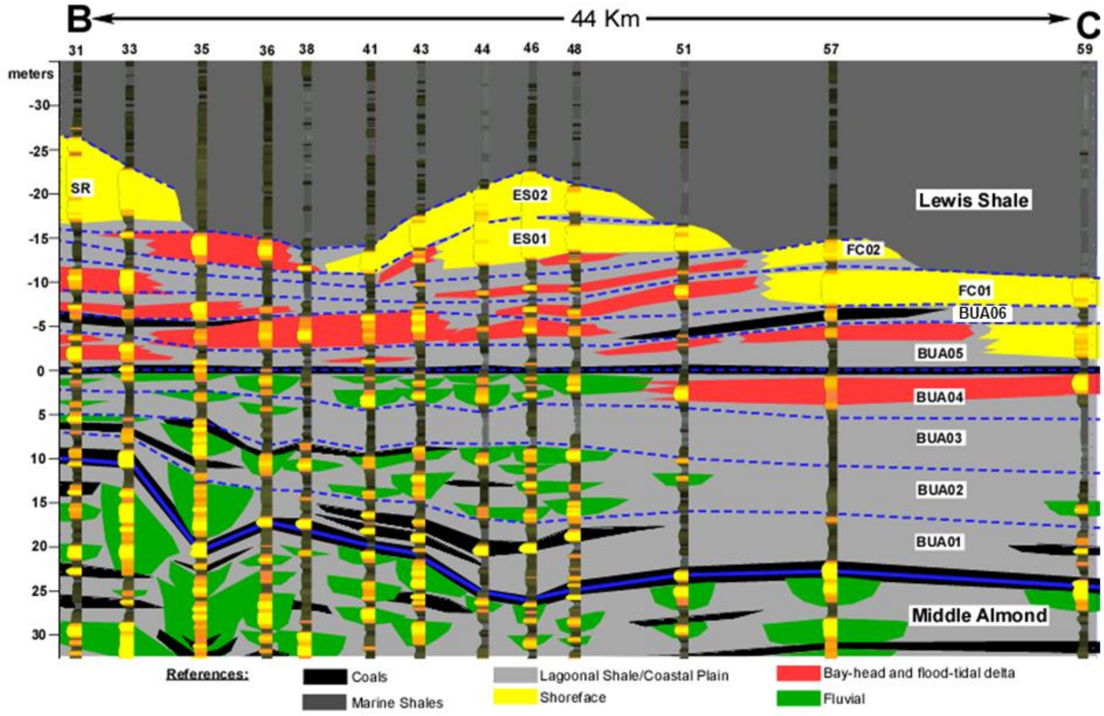

Figure 5.11: West-east cross section showing stratigraphic intervals in the eastern part of the field. The cross section is flattened to the top of the BUA04 interval. Abbreviations mean Basal Upper Almond (BUA), Fillmore Creek (FC), Echo Springs (ES) and Siberia Ridge (SR). Location of cross section is displayed in Figure 5.5

### *5.6.3.1 Basal Upper Almond (BUA)*

This interval, in the west of the study area, is the nonmarine/brackish equivalent of at least six shallow-marine parasequences in the east of the study area. The units BUA01 through BUA03 are dominated by fine-grained, coastal-plain deposits (Figure 5.11). Individual sandstone units are 1.5 to 4m thick, display an upward-fining or an upward-coarsening GR log patterns and are interpreted as fluvial channel and crevasse-splay fills deposits respectively. The patchy, irregular sandstone distribution on the sandstone thickness maps makes the interpretation of paleoflow direction difficult when mapping individual units. However, when the three older units are stacked, they suggest southerly to south-easterly dominant flow direction (Figure 5.12A).

The BUA04 (Figure 5.12B) includes 1 to 3m thick sandstone units which display both upward-fining and upward-coarsening GR log patterns. The BUA04 deposits are interpreted as a northwest-fed fluvial system reaching a bay shoreline (blue line) and developing multiple bay-head delta lobes. This interval is topped by a 1m thick coal bed identified in every western well. The extensive lateral continuity of the coal suggests that the low-energy coastal plain environment in the western sections prograded over the fluvial system and bay-head deltas eastwards beyond the study area.

The first Upper Almond shoreface deposits are interpreted to have been deposited in Unit BUA05; two wells penetrated the landward side of a north-south trending barrier island in the east edge of the study area (Figure 5.12C). The barrier deposits are 5m thick and exhibit a blocky GR log pattern. In the bay or lagoon environment west of the barrier, three elongate to lobate features are apparent in sandstone thickness maps. The two closer to the inner-bay shoreline are interpreted as bay-head deltas whereas the one adjacent to the barrier island is likely to be a flood-tidal delta because it extends southeastward to what would be the barrier inlet. Unfortunately, there are no core data to provide sedimentary structures and rock texture in the described deposits. Upward-coarsening GR log patterns are observed in each well for these 2-3m-thick sandstone units, supporting the above interpretations. Alternatively, all three of these features can be interpreted as different stages of bay-head delta development onto the lagoon environment. The youngest unit of this interval, BUA06, is characterized by lobate-shaped features interpreted as the bay-head deltas (Figure 5.12D). The two lobes in the north are fed by north-westerly derived fluvial systems whereas the one in the south seems to be fed by a west-east fluvial system. The bay-head delta deposits show upward-coarsening GR patterns and average 3m thick.

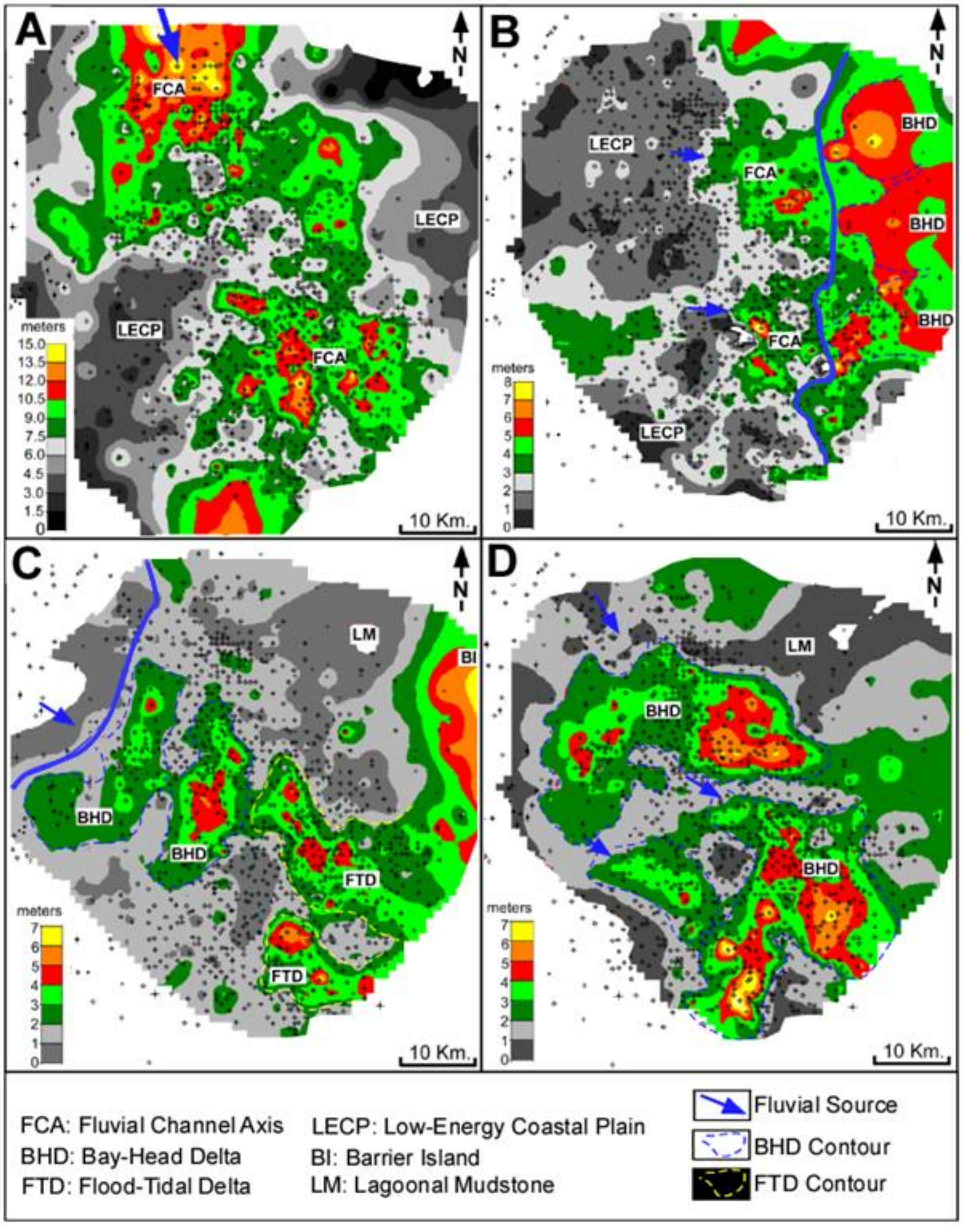

Figure 5.12: Sandstone thickness maps for four intervals within Basal Upper Almond (BUA). Sandstone maps correspond to BUA01 through BUA03 (A), BUA04 (B), BUA05 (C) and BUA06 (D). Continuous blue lines indicate the location of the bay shoreline.

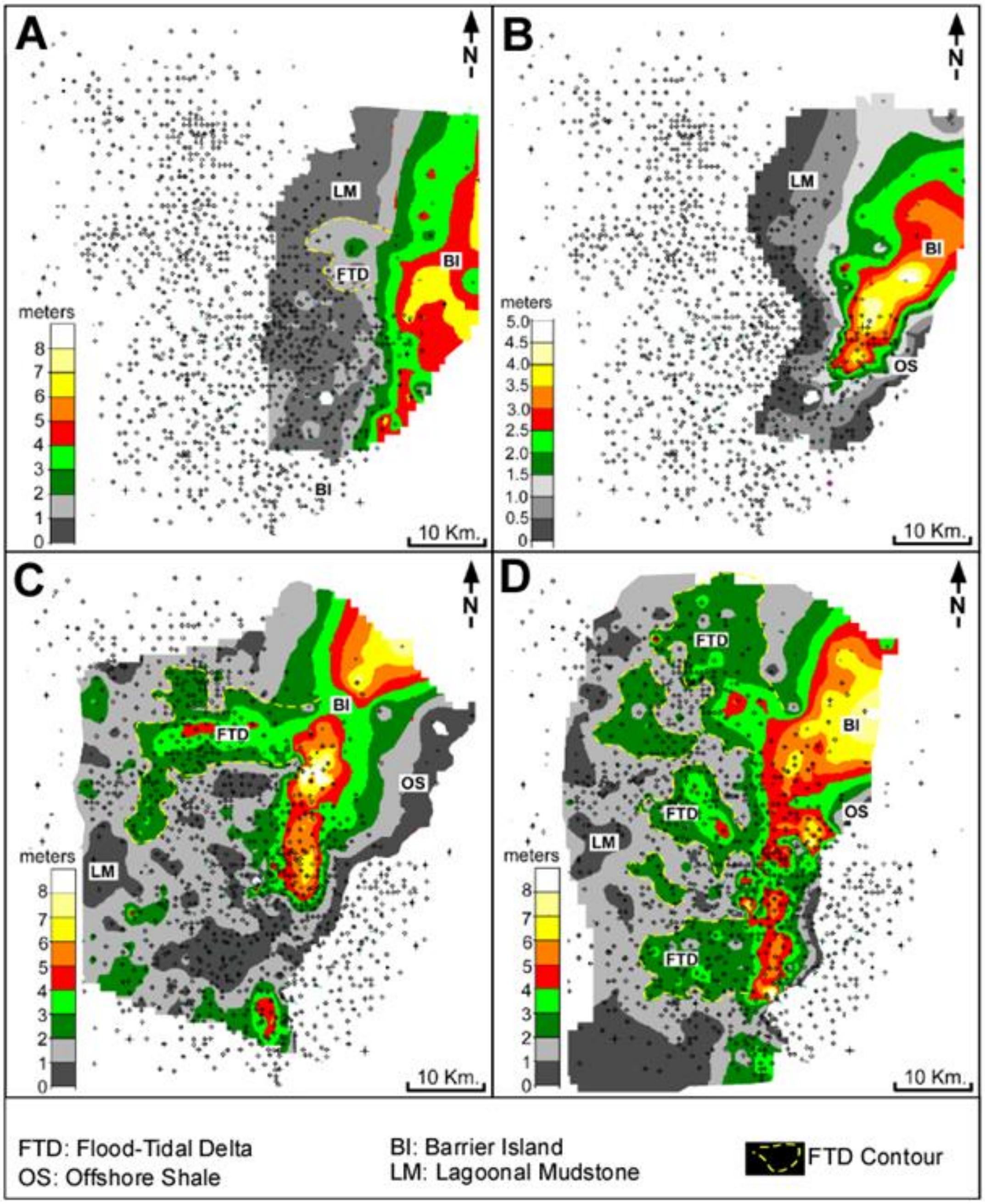

Figure 5.13: Sandstone thickness maps of Fillmore Creek (FC) and Echo Spring (ES) units. Maps correspond to FC01 (A), FC02 (B), ES01 (C) and ES02 (D).

The depositional facies associations of Basal Upper Almond units (Figures 5.12A through D) record a general backstepping of the bay shoreline with solely fluvial deposits in older units and bay-head deltas and a landward edge of a barrier island in younger units.

#### *5.6.3.2 Fillmore Creek (FC) Barriers*

This interval is composed of backstepping units referred to as FC01 and FC02 (Figure 5.11). The older unit shows an elongated sandbody only reached by wells in its landward edge (see FC01 in Figure 5.13A). In the landward wells, the units display a blocky to upward-coarsening GR log pattern. The sandstone fraction of the body FC01 is 6 to 12m thick, 40 Km long, at least 12 Km width and is interpreted as barrier island deposits. The FC01 parasequence is topped by relatively thin, 1 to 2m thick, marine shale that records the flooding of the barrier-island and possible associated ravinement. In some few locations, wave erosion removed marine shales and the boundary to the next unit is rather interpretative (sand on sand contact). At the top of FC01, the paleo-shoreline transgressed approximately 4 km to the west to start the regressive development of the new barrier complex referred to as FC02 (Figure 5.13B). This barrier island is 8 to 12 m thick, 40 Km long, 11 Km width as seen on the sandstone thickness map. This sandbody displays a dominantly blocky GR profile, commonly with a sharp base toward its landward side. Such sharp bases are fairly common towards the thinning 'butt-end' of barriers. Sandbodies of FC01 and FC02 show a southward narrowing and pinch out (Figure 5.3 A-B).

The Fillmore Creek interval also displays an incipient development of flood-tidal deltas (Figure 5.13A-B); these features evidence the presence of channels (tidal inlets) across the barrier connecting the shoreline with the lagoon. The flood-tidal deltas are 3 to 4 m thick and exhibit a clear upward-coarsening GR log pattern.

#### *5.6.3.3 Echo Springs (ES) Barriers*

Located twelve kilometres landward of the Fillmore Creek units, the Echo Springs (ES) stratigraphic interval contains two units referred to as ES01 and ES02. They display a depositional stacking pattern that varies from aggradational to slightly retrogradational (Figure 5.11). The intervening transgressive to regressive marine shale is preserved in some locations but eroded by wave ravinement in others (sand-sand contact).

Sandstone thickness maps (Figure 13C-D) show large, elongated morphologies across the entire study area. The sandbodies, interpreted as barrier island deposits, are 73 Km long, 12 Km wide, and 6 to 12m thick. In the wells, the sandstone units commonly display sharp bases and blocky GR log patterns, possibly caused in places by inlet channels.

Multiple flood-tidal deltas are spectacularly developed up to 22 Km away from the landward (westward) edge of barrier islands. Flood-tidal deltas are 3 to 6 m thick and display a typical upward-coarsening GR log pattern. They switch positions between successive parasequences and are larger than the ones interpreted in the underlying Fillmore Creek interval. There is no evidence of sediment being circulated out toward the basin and deposited as ebb-tidal deltas.

#### *5.6.3.4 Siberia Ridge (SR) Barriers*

The post Echo Springs flooding caused the barrier shoreline to migrate 30 Km to the west (landward) and formed the Siberia Ridge unit (Figure 5.14). This unit lacks fine grained beds that could support subdividing it into more than one unit. The sandstone fraction is 7 to 11 m thick and displays an upward coarsening GR log pattern. The sandstone thickness map (Figure 5.15A) displays a relatively abrupt reduction in sandbody width from 20 Km in the north to pinching out toward the centre of the field. The decrease in width is interpreted as the southern tip of a barrier island that, given its width and dominant GR character, prograded a few kilometres before the next flooding event. As with the Fillmore Creek barrier, the Siberia Ridge barrier shows a subtle development of a flood-tidal delta probably deposited in the early stage of the unit's development, before progradation started.

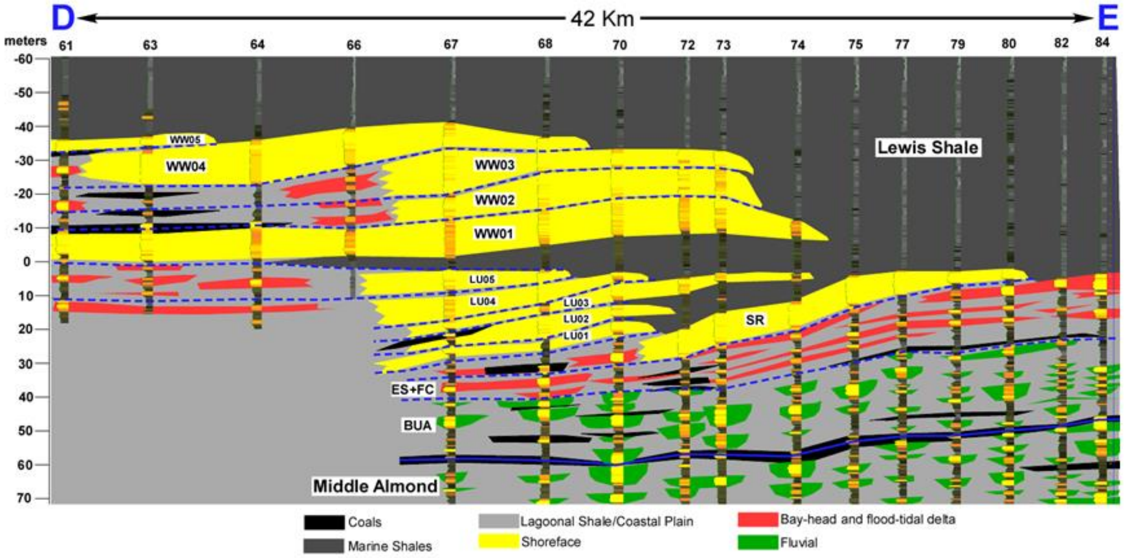

Figure 5.14: dip-oriented cross section showing stratigraphic intervals in the western part of the field. Location of cross section is displayed in Figure 5.5.

### *5.6.3.5 Luman (LU) Barriers*

Relative sea-level continued to rise, submerging the Siberia Ridge unit and shifting the shoreline 10 Km farther west, giving rise to the first (oldest) Luman sandbody called LU01. The sandstone thickness map displays a 25 km long, 8 km wide, depositional strike-elongate sandbody of irregular thickness (Figure 5.15B). LU01 is interpreted as a barrier island deposit and it is intersected by multiple inlet channels. The overlying two Luman units, LU02 and LU03, in the well cross section of Figure 5.14, each record a seaward stepping of approximately 5 km in a clear prograding pattern (Figure 5.14). Sandstone thickness maps, show 25 Km long, 12 to 14 Km wide elongated sandbodies with fewer inlet channels than in LU01 (Figure 5.15 C and D). The youngest Luman units, LU04 and LU05, display a retrogradational stacking pattern, where landward steps are about 2 kilometres. Luman parasequence boundaries are preserved as 1 or 2 m-thick marine shales and these two sandbodies pass landwards to coaly beds in the back-barrier environment. Sandbodies in each parasequence are 3 to 6 m thick and have blocky GR log patters with sharp bases. The entire Luman sandbody complex can be termed a parasequence set where the three older parasequences display progradation whereas the two younger parasequences show a retrogradational trend.

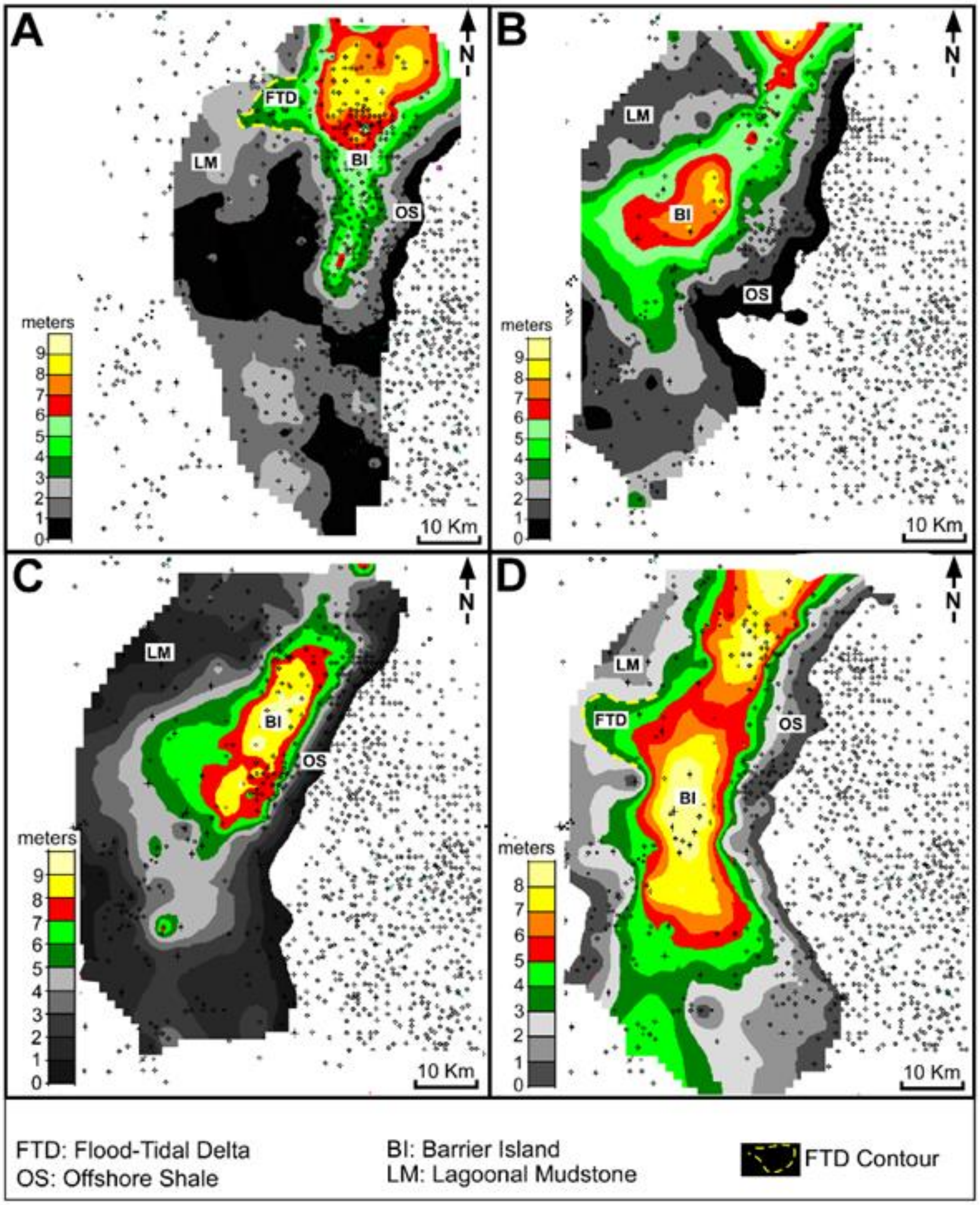

Figure 5.15: Sandstone thickness maps of Siberia Ridge (SR) and Luman (LU) units. Maps correspond to SR01 (A), LU02 (B), LU03 (C) and LU04 (D).

### *5.6.3.6 West Wamsutter (WW) Strandplains and Barriers*

The West Wamsutter (WW) sandbody complex is developed in the northwest corner of the Wamsutter field area and extends through the Desert Springs and Patrick Draw fields. It is the thickest of the sandbody complexes mapped in the current subsurface dataset, and can be as thick as 38 meters.

The West Wamsutter complex is composed of 5 genetic sandstone units separated by relatively thin (0.5 to 1m) shaly or coaly beds. Commonly, the shales and coals are eroded by transgressive wave-ravinement surfaces and not always preserved as distinct surfaces and as a consequence, parasequence boundaries are interpreted between sandstone units.

The base of the WW unit coincides with a regional flooding event that extended throughout the study area; the flooding is documented by the shale wedge between Luman and West Wasmutter units in Figure 5.14. After this flooding, the depositional system began to prograde again, giving rise to the oldest West Wamsutter parasequence, WW01.

The WW01 sandstone thickness map (Figure 5.16A) shows a 10-13 m thick, 30 km wide sandbody that covers a large part of the study area. This configuration of a broad and extensive regressive belt of sandstone, along with the persistent upward-coarsening GR log patterns, suggests that WW01 should be termed a regressive strandplain rather than a barrier bar. No inlet channels are observed to cut through the WW01 sandbody, even in areas of dense well spacing.

The progradation of WW01 eventually stalled and a new transgression gave rise to a series of backstepping parasequences (Figure 5.14). In contrast with WW01, WW02, WW03 and WW04 (Figure 5.16B-D) developed relative narrow 70 Km long, 12 Km wide sandbodies interpreted as barrier island deposits. The barrier islands of WW02,

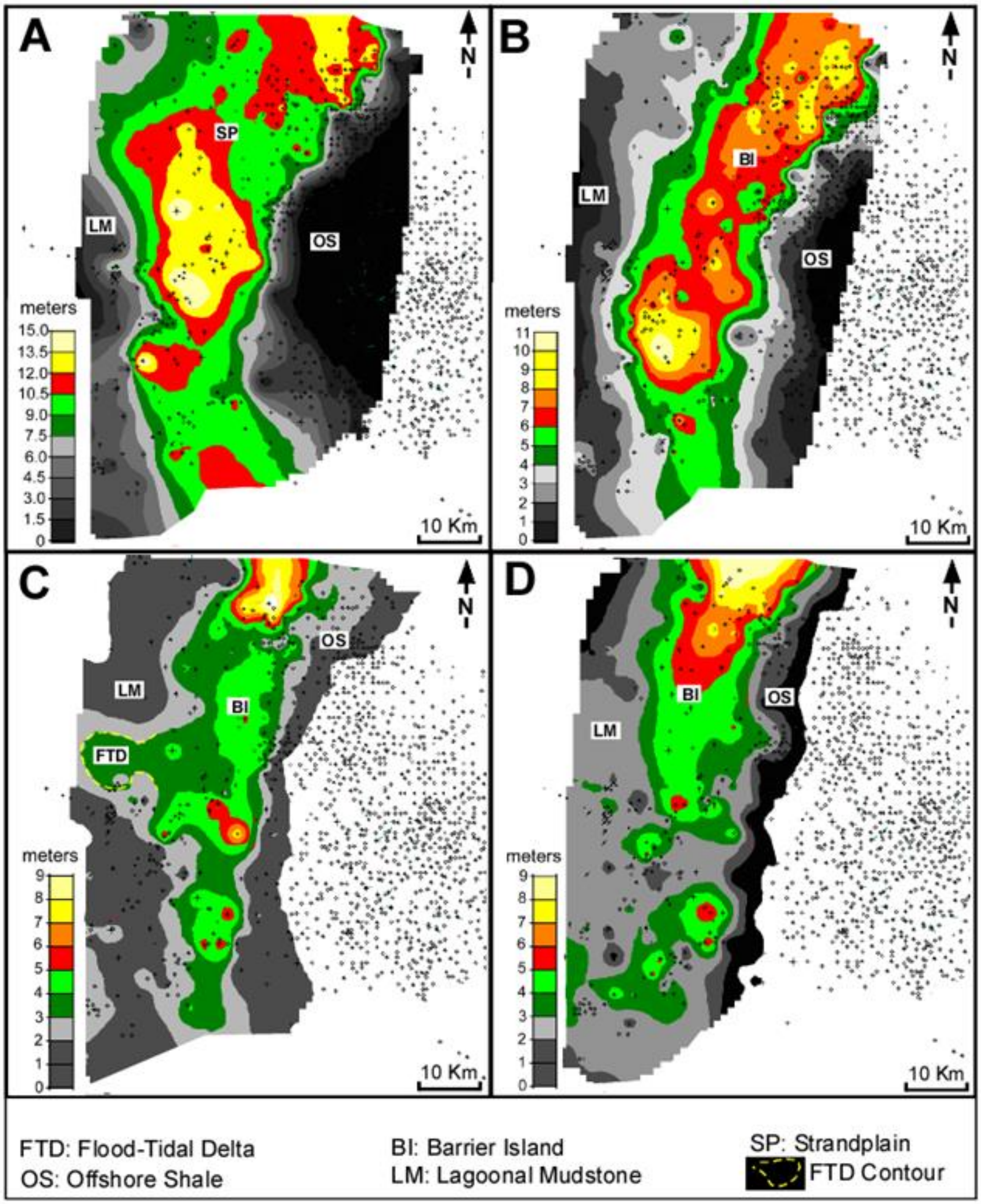

Figure 5.16: Sandstone thickness maps of West Wamsutter units. Maps correspond to WW01 (A), WW02 (B), WW03 (C) and WW05 (D).

WW03 and WW04 display shaly and coaly facies in their landward lagoonal side (Figure 5.14). The WW04 unit is topped by the WW05 parasequence which is only defined by its seaward (eastward) edge reached by some wells.

## 5.7 DISCUSSION

### 5.7.1 Barrier evolution and terminology

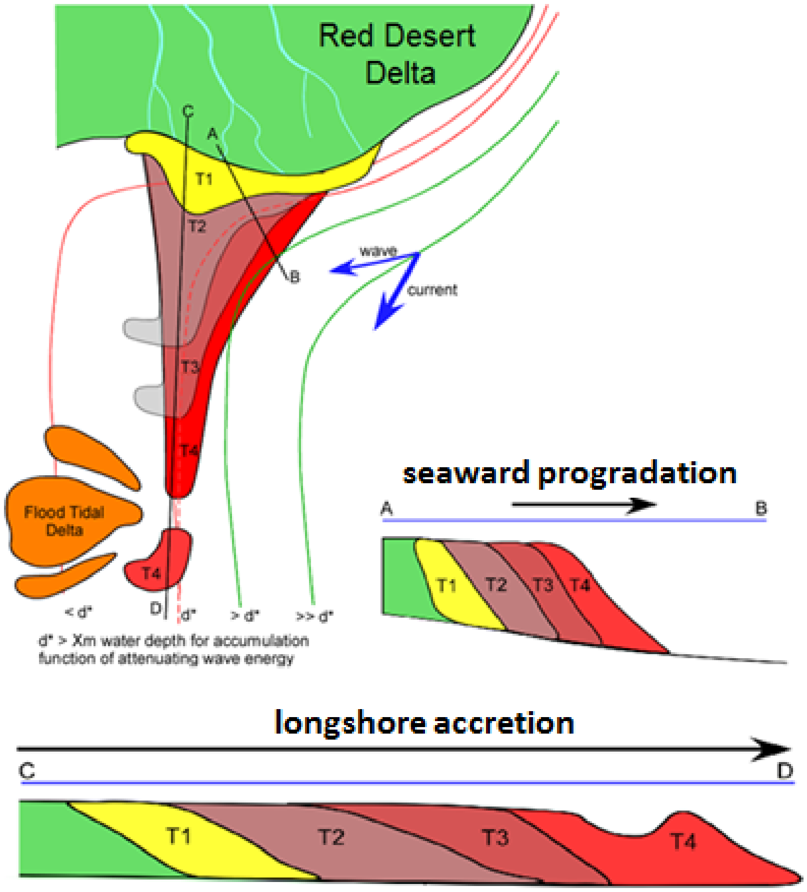

Figure 5.17: Reworking of delta-derived sediments into sandspit and then barrier island. Long-shore drift resuspends and transports delta dominated sediment southward into elongate barrier spit units.

There is overwhelming evidence of southward narrowing of the barrier islands in the Upper Almond shallow marine succession of the study area. This implies a dominantly southward longshore sediment transport, rather than direct supply from river currents bringing sediments eastwards from the Cordilleran thrust belt in the west. The formation of these north-south elongate sandbodies is assigned to three processes: 1- sediment sourced southward from distributary channel mouths and shorefaces of the Red Desert delta complex just to the north of the study area, 2- resuspension of delta front sands by waves and southward transport by longshore currents into elongated sandbodies or sandspits, and 3) variable growth of sandspits into barrier islands and occasionally sandbodies broad enough to be termed strandplains, by seaward accretion of newly reworked and transported sand by storm-wave generated long-shore currents. Figure 5.17 summarizes these processes in four time steps; the strike- and dip-oriented cross sections in the lower right show eastward progradation and southward accretion components of the barrier spit units. Eventual changes in the dominant wind direction might have caused the reworked material at the southward extent of the spit to swing around landward, generating hooked morphologies of the sandspits. This would account for some of the irregular shapes observed along the landward edge of mapped sandstone bars. After some significant elongation of the spits and establishment of barrier bars with some seaward-accretion, tidal currents opened inlets through the barriers and caused the development of multiple flood-tidal deltas (Figure 5.17). We therefore designate the Upper Almond marine sandbodies as Barrier Spit Units (BSU) and define them as elongated sandbodies generated by the seaward accretion of longshore drift-sourced reworked sediments. BSUs are underlain by either thin coaly strata of the coastal plain or by offshore marine shales. This vertical configuration implies that below each BSU there was a transgressive ravinement surface, connecting the distal tip of one BSU with the proximal ‘butt-end’ of the overlying BSU. This ravinement surface would have thin to very thin transgressive lag deposits and marine shales on top, but would also have preserved coaly coastal plain strata below, particularly at the landward end of the ravinement.  In some cases these underlying coaly and shaly layers were eroded by the sharp base of the BSU and the distinction of different BSUs can be interpreted only by landward shift of sandbody edges.

### 5.7.2 Paleogeography of BSUs

Paleogeographic reconstructions in Figure 5.18 summarize three backstepping barrier spit systems. The dashed lines inside the barrier island represent steps of seaward barrier accretion of two Echo Springs BSUs, caused by longshore drift sourcing from the northern delta source (Fig. 5.18A). As the barrier island evolved, tidal currents opened inlets and multiple flood-tidal deltas developed on the landward side of the barrier. When observed in cored wells (star in Figure 5.18A), these barrier island deposits usually have a sharp erosive base, bioturbation only at the top (developed from relatively high and constant storm-wave energy) and are represented by blocky to slightly upward-decreasing GR log patterns (Figure 5.8). Sandbody dimensions (Figure 5.13D-E) and log pattern interpretation suggest that there was a limited seaward progradational component when compared to the southward elongate accretion component (Figure 5.17).

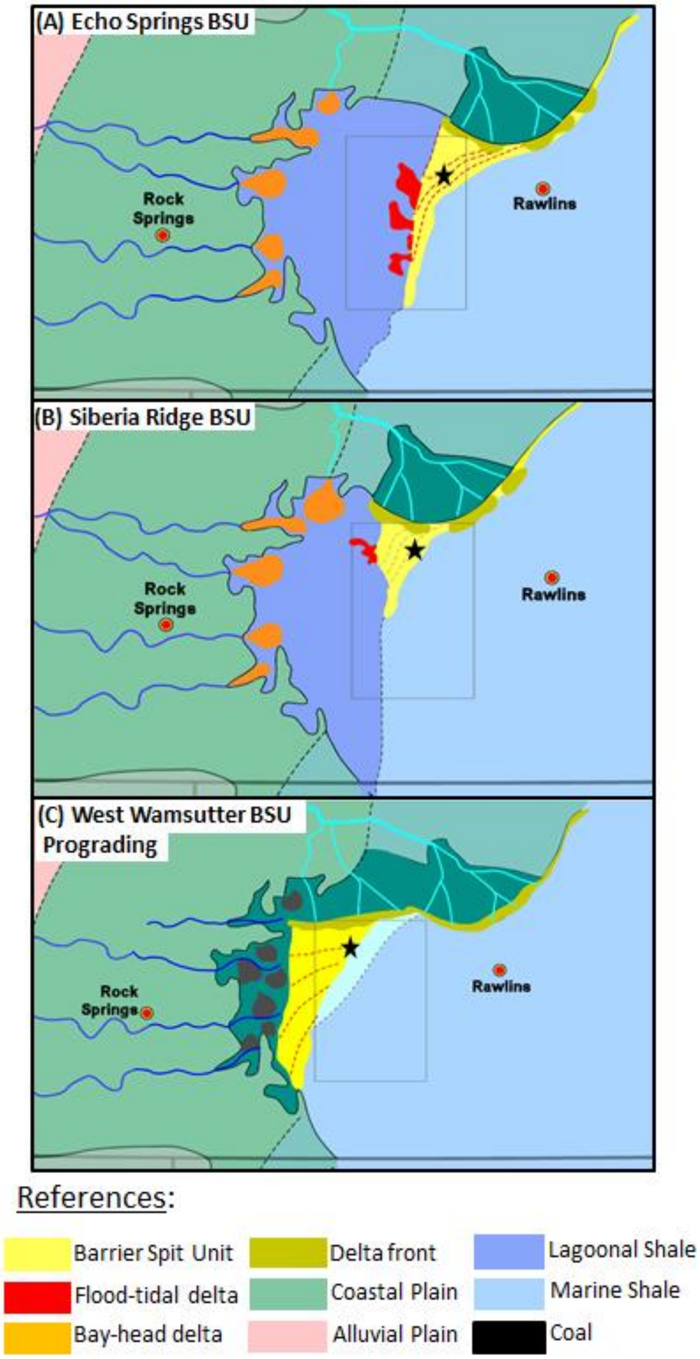

Figure 5.18: Paleogeographic reconstruction of Echo Springs (A), Siberia Ridge (B) and West Wamsutter (C) units.

The transgressive flooding event that drowned the Echo Spring bar moved the site of the next spit barrier unit 35 km westward, to the Siberia Ridge BSU. This shoreline movement is measured between the seaward side of the Echo Spring's youngest sandbody and the landward side of the Siberia Ridge unit (Figure 5.19).

The Siberia Ridge BSU exhibits the most abrupt southward narrowing and evidence of greater progradation than accretion (Figure 5.18B). The latter observation is supported by more pronounced upward-decreasing GR log patterns in numerous wells, especially the ones located in the seaward side of the sandbody. The sandstone southward narrowing morphology and log pattern indicate a proximity to sediment source. The Siberia Ridge BSU morphology also suggests that sediments were reworked but not transported very far southward before the subsequent drowning event. The core examined is from the seaward side and contains a high bioturbation index both in the bottom and the top of the sandbody (stat in Figure 5.18B). The overall upward increase from low to moderate wave energy is documented by structureless and rippled sandstones at the bottom to parallel and planar cross stratified sandstones at the top (Figure 5.9). When compared to the core in the Echo Springs unit, the Siberia Ridge core exhibits a low abundance of high wave energy sedimentary structures and more intervals with pervasive bioturbation. These observations suggest a more sheltered depositional environment which could have been caused by eastward progradation of the Red Desert Delta.

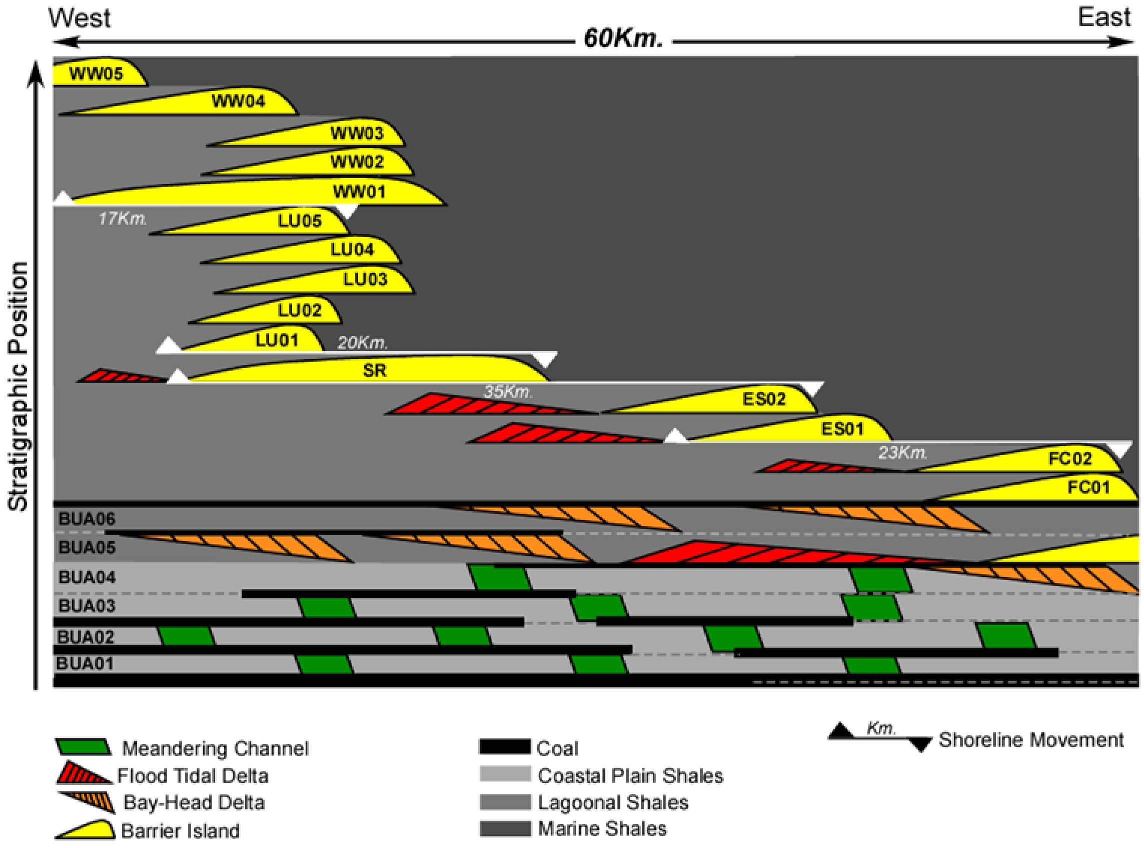

Figure 5.19: Depositional facies associations in a generic west-east cross section across the field.

The later flooding event that submerged the Siberia Ridge BSU moved the barrier spit shoreline 20 km to the west, marked by the position of the oldest Luman deposit, LU01 (Figure 5.19). The five Luman BSUs exhibit a similar morphology i.e., elongated strongly reworked accreted sediment assembled in barrier island complexes. A close balance between accommodation and longshore sediment supply characterized the Luman deposition where BSU ograded and transgressed in 2 to 4-kilometer steps (Figure 5.19). The abundance of coaly layers developed in lower coastal plain environment suggests progressive filling up of the well-developed lagoon typical of older BSUs. The lack of core data and the sparse well control in the landward side of Luman BSUs make the latter interpretation speculative.

The youngest flooding event recorded in the study area moved the barrier spit shoreline 17 km westward, marked by the landward side of the oldest West Wamsutter BSU (Figure 5.19). The north part of the West Wamsutter BSU is 28 kilometres wide and narrows to half of that width in its southern tip (Figure 5.18C). Marked upward-decreasing GR log patterns and great lateral extent of the sandbody suggest that this BSU records the largest progradational component in the study area when compared to older BSUs. Deposition of this 15 m thick composite body in WW01 is the most fluvial-dominated with low wave influence. This is supported by very sparse wave-induced sedimentary structures, thin to medium bedded amalgamated beds and low-to-medium bioturbation index throughout the entire cored interval (Figure 5.10). The location of the cored well, shown as a star in Figure 5.18C, coincides with the position of the underlying Siberia Ridge BSU; this superposition could have contributed to decrease the already low shoreline gradient and further reduced wave action. As longshore accretion and progradation progressed, the back barrier area filled up by sediment brought by bay-head deltas. This is recorded by abundant carbonaceous shales and coaly beds behind the spit and between BSUs (Figure 5.18C). There is very limited well control and no core on back-barrier areas of the younger West Wamsutter BSUs. These units display similar morphologies to Luman and Echo Springs units, therefore it is interpreted that the accretion component dominated the barrier formation and a lagoon developed as in older BSUs.

There is no evidence of a smooth and continuous transgression controlling sandstone deposition and preservation in Upper Almond times. The alternation of long-term coastal retrogradation and short lived southward accretion and eastward progradation (regression) makes the hybrid punctuated transgression model the most appropriate model (Figure 5.19). The upper shoreface deposits, recorded as planar and trough cross-stratification, are usually topped by an erosive ravinement surface and its overlying intensively bioturbated sandstones that developed as water depth increased (Figure 5.8).

### 5.7.3 Age and Cyclicity

Some age-diagnostic fossils from the Almond Formation have been collected from outcrops in the Rock Springs uplift area (Roehler 1988). The ammonite index fossil *Baculites baculus* was reported near the top of the Almond in the Rock Spring Uplift area and *Baculies eliasi* in the basal part of the Lewis shale northwest of Rawlins Uplift area in rocks that are equivalent of the Middle Almond (Gill et al., 1970). Gradstein et al. (2012) dated the *Baculites grandis* biozone as 70.5 to 71.1 Ma, the *Baculites baculus* biozone as 71.1 to 72.1 Ma and the *Baculites eliasi* biozone as 72.1 to 72.7.

In the Rock Spring uplift area, Martinsen et al. (1999) placed the base of the lower Almond in the uppermost *Baculites reesidei* biozone (73.3 Ma). This would imply that the whole Almond deposition, between the Asquith marker and the contact with the Ericson Formation in Rock Springs uplift represents about 1.7 My.

I take the average age of *Baculites baculus* (71.6 Ma, ±0.4) and *Baculites eliasi* (72.4 Ma, ±0.35 ) biozones as the representative ages for the top of Upper and base of middle Almond respectively. I infer that this time-period (0.8 My) represents the deposition of the prograding Middle Almond and the transgressing Upper Almond.

A minimum of seven upward-coarsening parasequences comprise the Middle Almond at the eastern edge of the field. The Upper Almond is composed of six Basal Upper Almond (BUA) units and fifteen Barrier Spit Units (BSU) in the study area (Figure 5.19). Additionally, a minimum of three BSUs are reported in Patrick Draw and Desert Springs fields (Figure 5.7). Assuming that base Middle and through Upper Almond were deposited in 0.8 My and the formation time of parasequences and BSUs is approximately similar, each of the main sandbodies could have been deposited in a time interval of about 25,000 years.

## 5.8 CONCLUSIONS

Analysis of high-quality well log suites in 1,450 wells over an area of 6,600 km$^2$ in the Upper Almond Formation has been used to construct a high-resolution chronostratigraphic framework. The mapping of individual bars allowed the evaluation of the evolution of the Wamsutter embayment during the long-term transgression of the late Campanian-early Maastrichtian period.

Fifteen BSUs that were stacked in a westward back-stepping architecture have been interpreted, and that were sourced from the north by a fluvial-dominated (Red Desert Delta of Asquith, 1970 and Roehler, 1988) deltaic shoreline. There are two endmembers in terms of sandbody morphologies: 1) narrow and elongated, drum stick-like sandbodies built mostly by longshore accretion (Figure 5.18A), and 2) broad and extensive regressive belt of sandstone with a more balanced longshore accretion to seaward progradation rate (Figure 5.18C).

The base of the Upper Almond is marked by the thickest and most laterally extensive coaly layer which is equivalent to the oldest shoreline turnaround 200 km eastward. Within the study area, transgressive events flooded across successive BSUs and shifted the sand deposition westward in 4 to 35 Km steps. Each BSU is 6 to 12 metres thick, displays a variable southward narrowing morphology in map view and is bounded above and below by relatively thin, 0.5-2m thick shaly or coaly layers which were locally removed by the transgressive wave ravinement processes.

The long term evolution of the entire succession of BSUs shows that the older sandbodies (i.e., Echo Springs) were built mostly by longshore accretion in a high accommodation environment, developed wide, eastward-extending lagoons and stepped longer westward distances. The younger BSUs tend to display more seaward progradation and are highly aggradational. Lagoons are filled up by bay-head deltas and replaced by coastal plain deposits (basal West Wamsutter). These observations indicate that in the younger half of the Upper Almond succession there was a quasi-equilibrium between accommodation and sediment supply, in contrast to the older half of the succession where dis-equilibrium between supply and accommodation caused long regressions and long transgression to alternate.

The clear overall long-term alternation of westward coastal retrogradation and shorter lived eastward progradation (with additional southward lateral accretion) indicates that hybrid punctuated transgression is the most appropriate model for creating and preserving Upper Almond sandbodies.

# CHAPTER 6: CONCLUSIONS

Detailed conclusions are presented in each chapter; here I summarize the main contributions of my dissertation. The linkage between depositional facies, petrophysics rock types, and petrographic observations (framework composition, types/amount of cement, and porosity type) should be fully understood to predict drivers of reservoir deliverability. In the case of the Almond Formation, a permeability model taking advantage of such a linkage shows the best correlation against dynamic data. While this analysis is recommended in conventional reservoirs, it is absolutely necessary in tight-gas sandstones where complex porosity-permeability relationships are expected. In the case of the Almond Formation, a 10% porosity reservoir could exhibit a range of four orders of magnitude for absolute permeability.

Primary drainage and imbibition saturation-height models can be successful implemented in rocks with complex pore structure. A novel method which combines mercury extrusion capillary pressure and counter current imbibition is used to build imbibition functions. Most of the Almond interval can be characterized by primary drainage models having variable fluids level. However, some Upper Almond bars exhibit anomalous high water saturation values that can be fitted with imbibition models. These reservoirs might have leaked hydrocarbon through nearby outcrops.

A high-resolution chronostratigraphic study of an overall transgressive coastline, documented with over 1,450 wells with high quality petrophysical logs over an area of 6,200 km$^2$, defines the fundamental geobodies in the transect as a series of 15 elongate sandstone units stacked into 6 reservoirs. Mapping of the lateral extent and vertical stacking of the individual sandbodies shows that there was a spectacular and westward rising of back-stepping barrier spits, sourced by long-shore currents mobilizing sand from a delta to the north. The westward transgressive-stepping across and into a structurally-generated embayment progressively dampened wave energy with each backstep. Morphologically, there were two endmember sandbody types: 1) narrow, drum stick-like sandbodies built mostly by longshore accretion, i.e. true barrier bars, and 2) broader and more extensive regressive belts of sandstone that resemble strandplains. The former display typically longer backsteps across lagoonal areas whereas the latter show a more aggradational stacking arrangement which evidences a quasi-balance between accommodation and sediment supply. The clear alternation of long-term coastal retrogradation and short lived barrier spit development by longshore accretion and seaward progradation makes the "hybrid punctuated" transgression the most appropriate model for creating and preserving Upper Almond sandbodies.

# Appendix

This section includes enlarged cross sections and maps displayed in Chapter 5 of this dissertation.

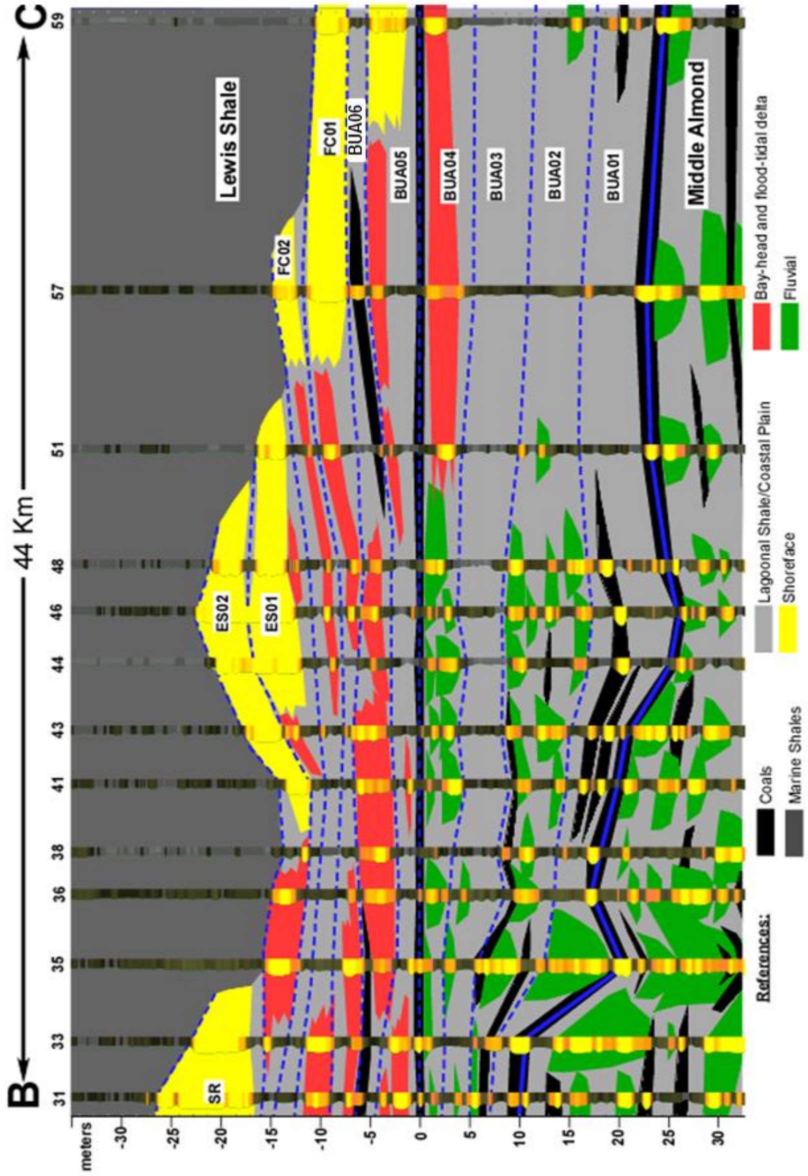

Enlarged Figure 5.11. Cross sections including eastern sandbodies.

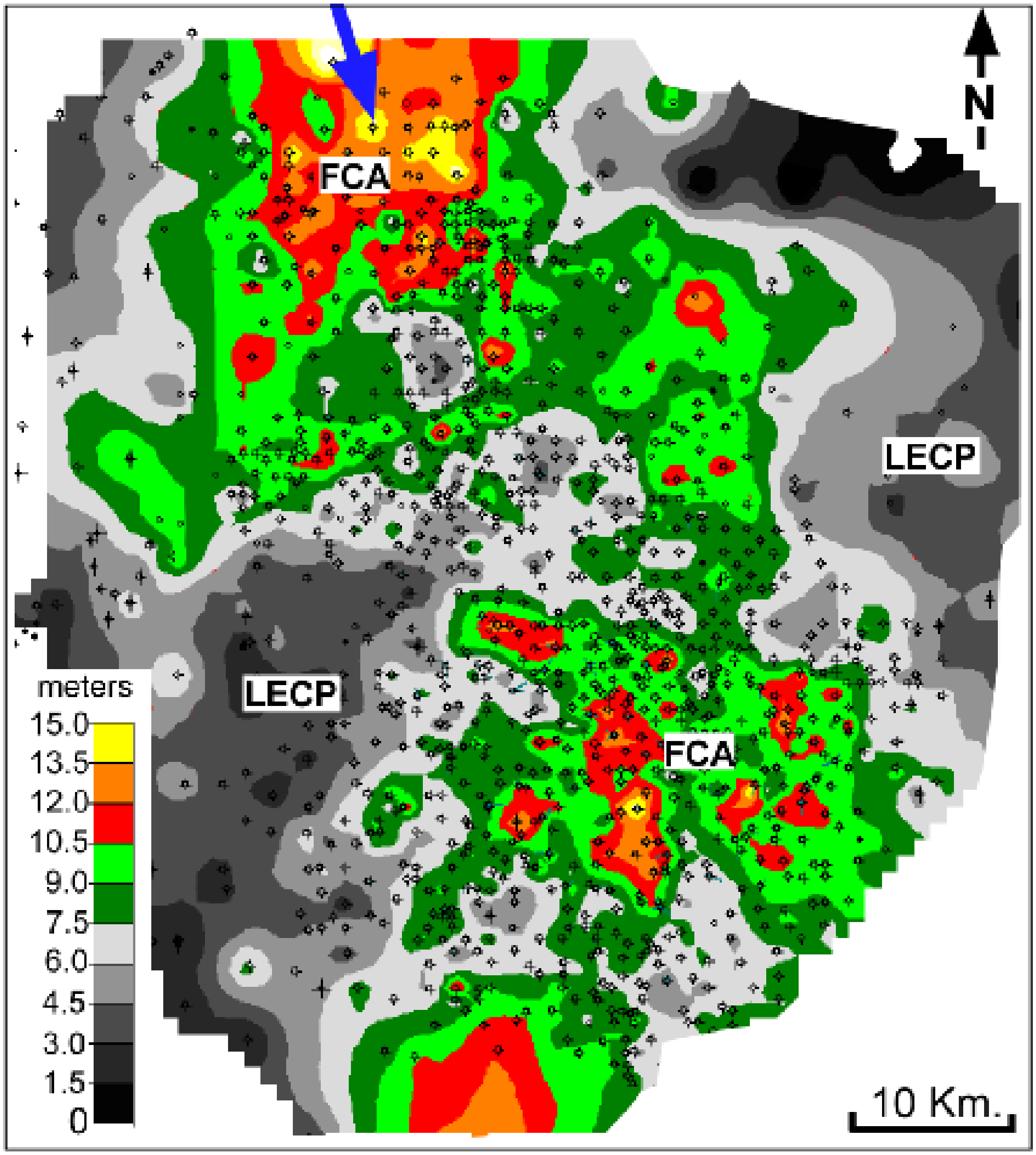

Enlarged Figure 5.12A. Sandstone thickness map of the BUA01, BUA02 and BUA03 intervals.

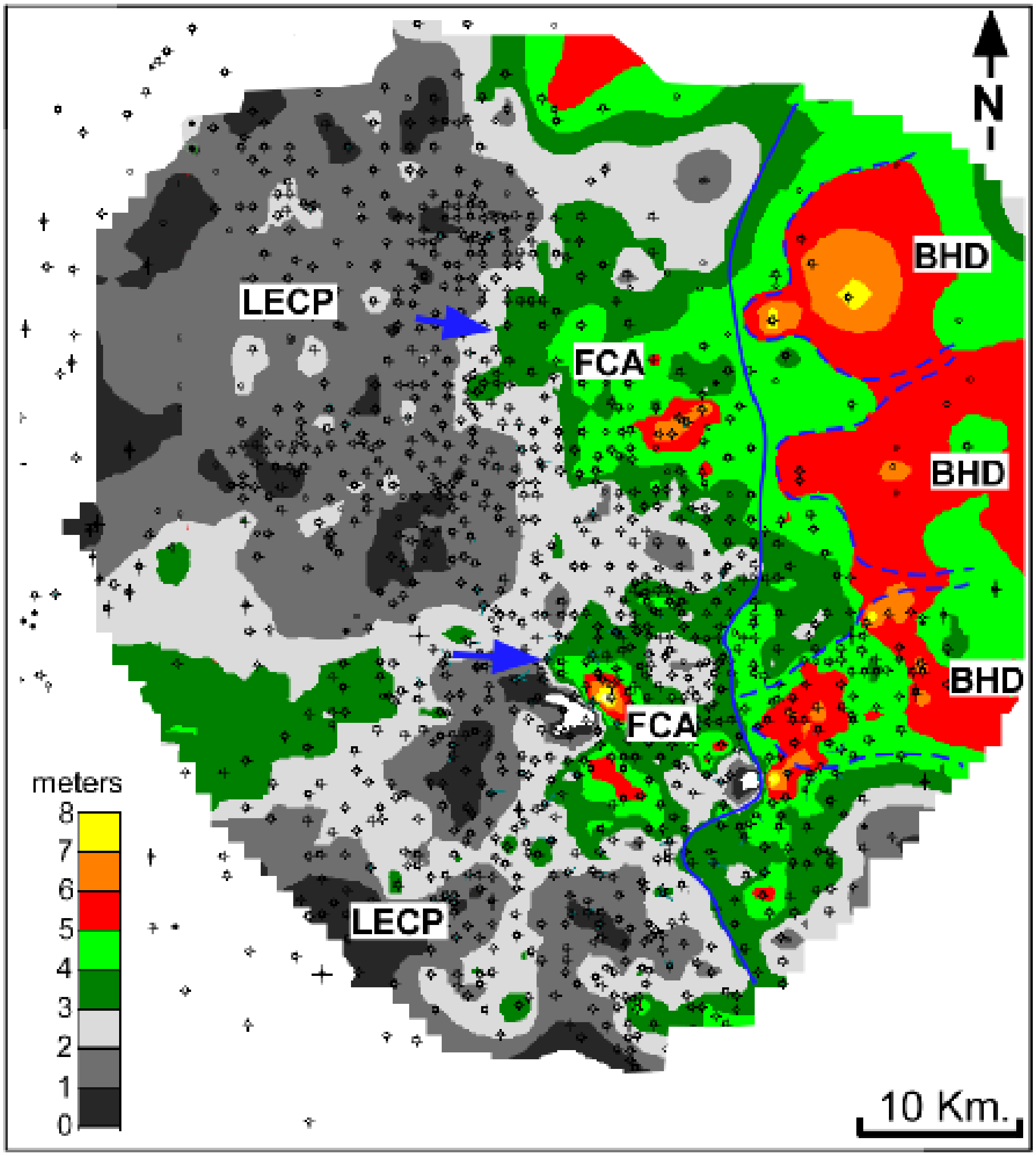

Enlarged Figure 5.12B. Sandstone thickness map of the Basal Upper Almond 04 interval (BUA04).

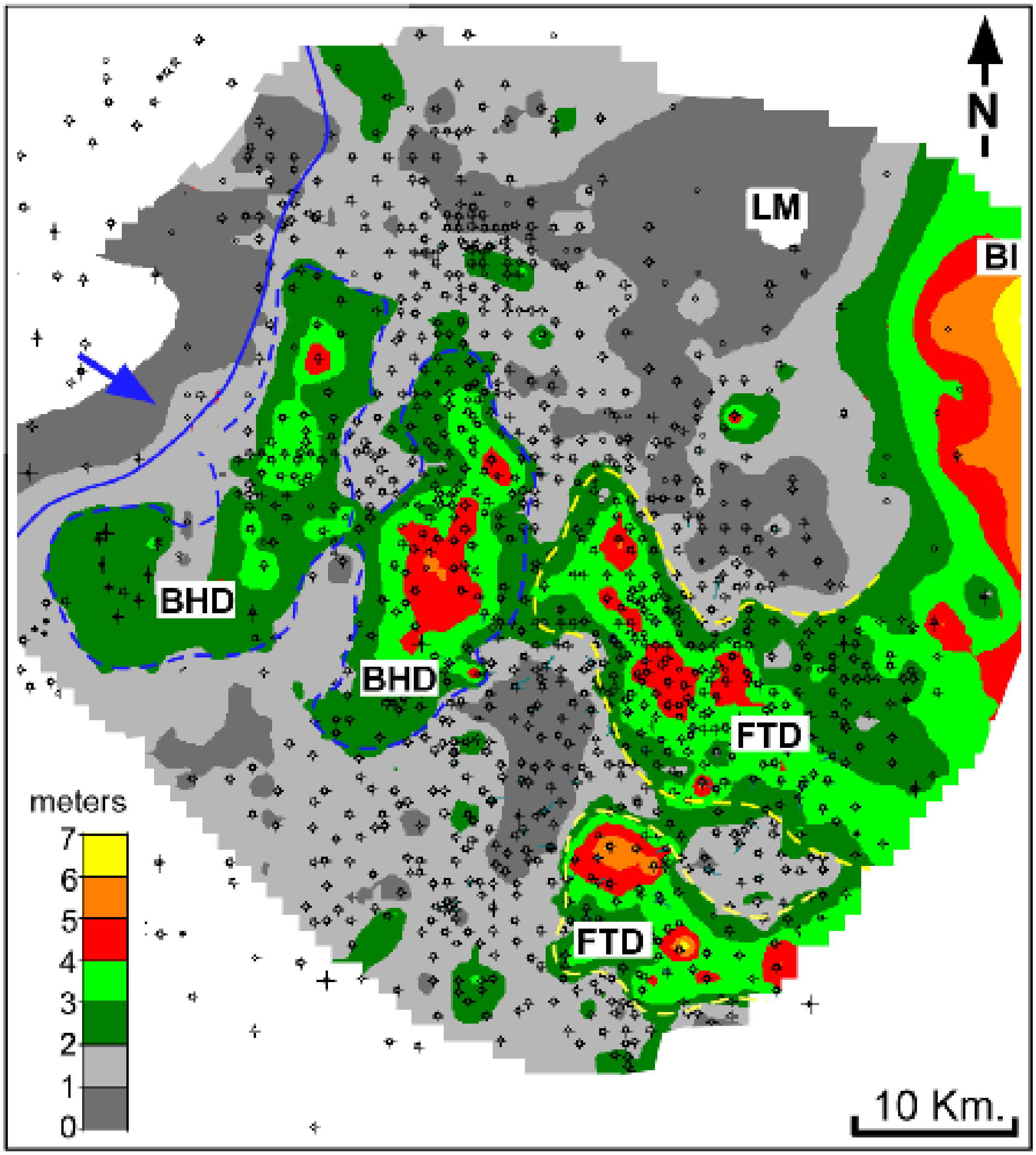

Enlarged Figure 5.12C. Sandstone thickness map of the Basal Upper Almond 05 interval (BUA05).

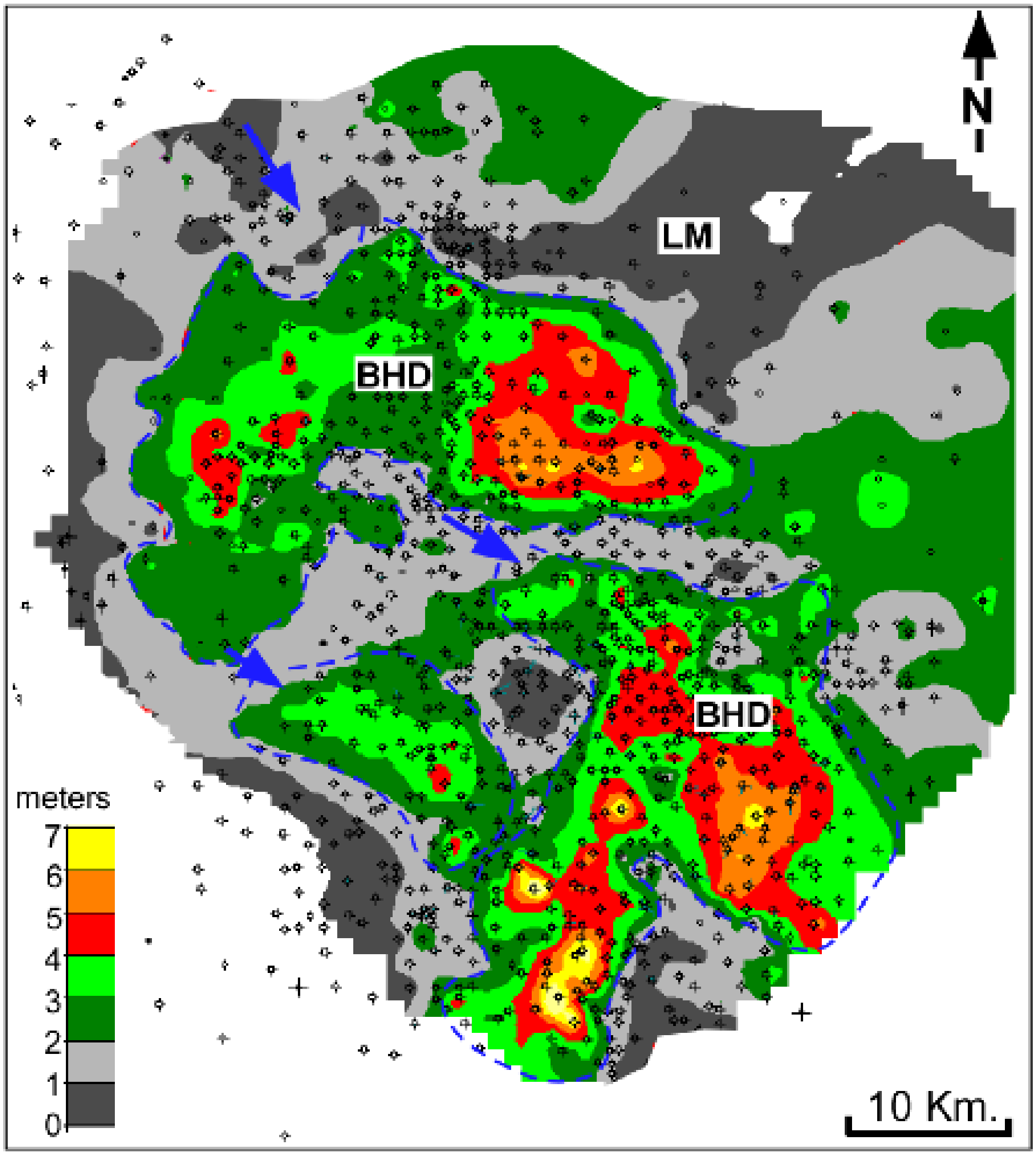

Enlarged Figure 5.12D. Sandstone thickness map of the Basal Upper Almond 06 interval (BUA06).

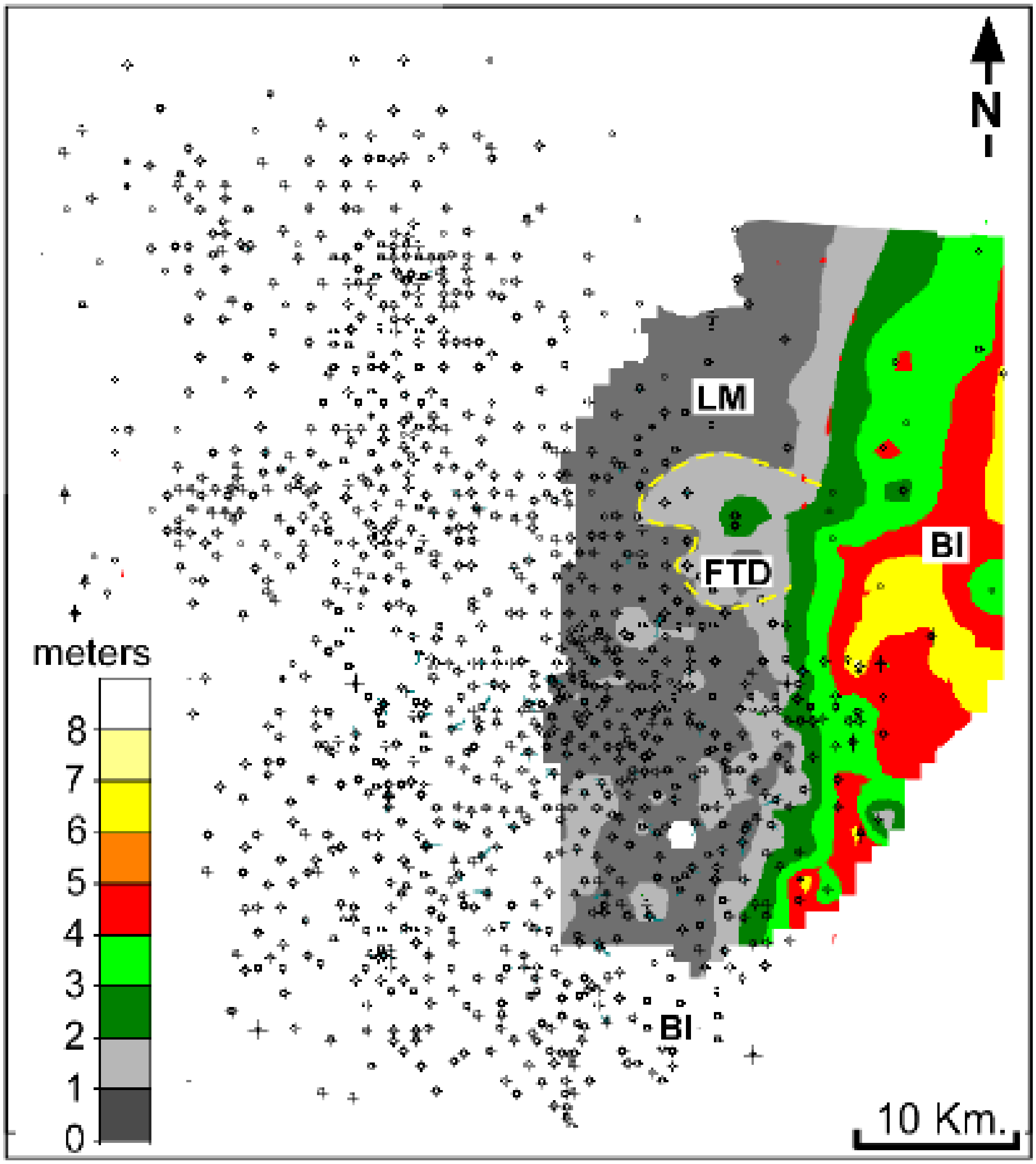

Enlarged Figure 5.13A. Sandstone thickness map of the Fillmore Creek 01 interval (FC01).

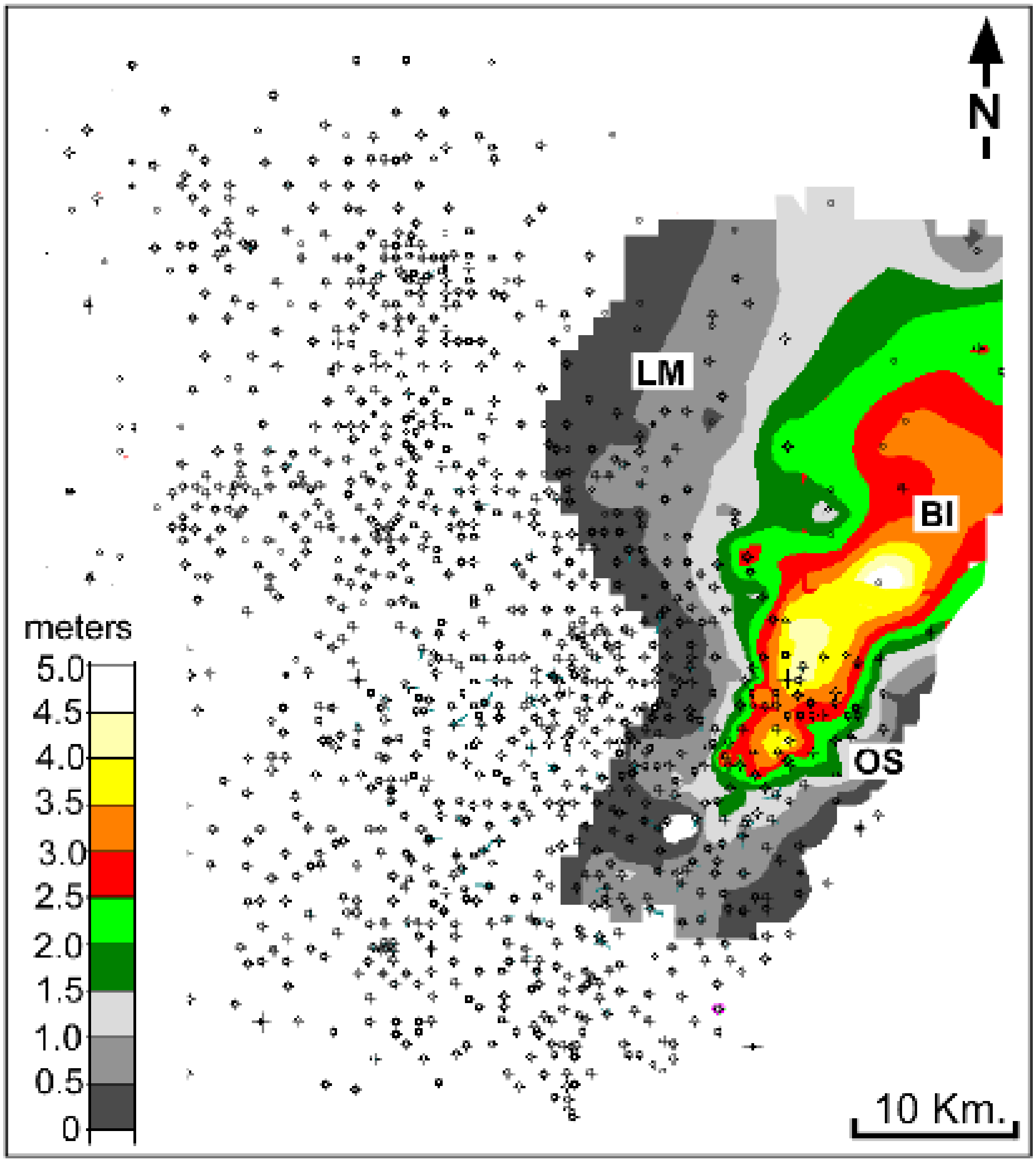

Enlarged Figure 5.13B. Sandstone thickness map of the Fillmore Creek 02 interval (FC02).

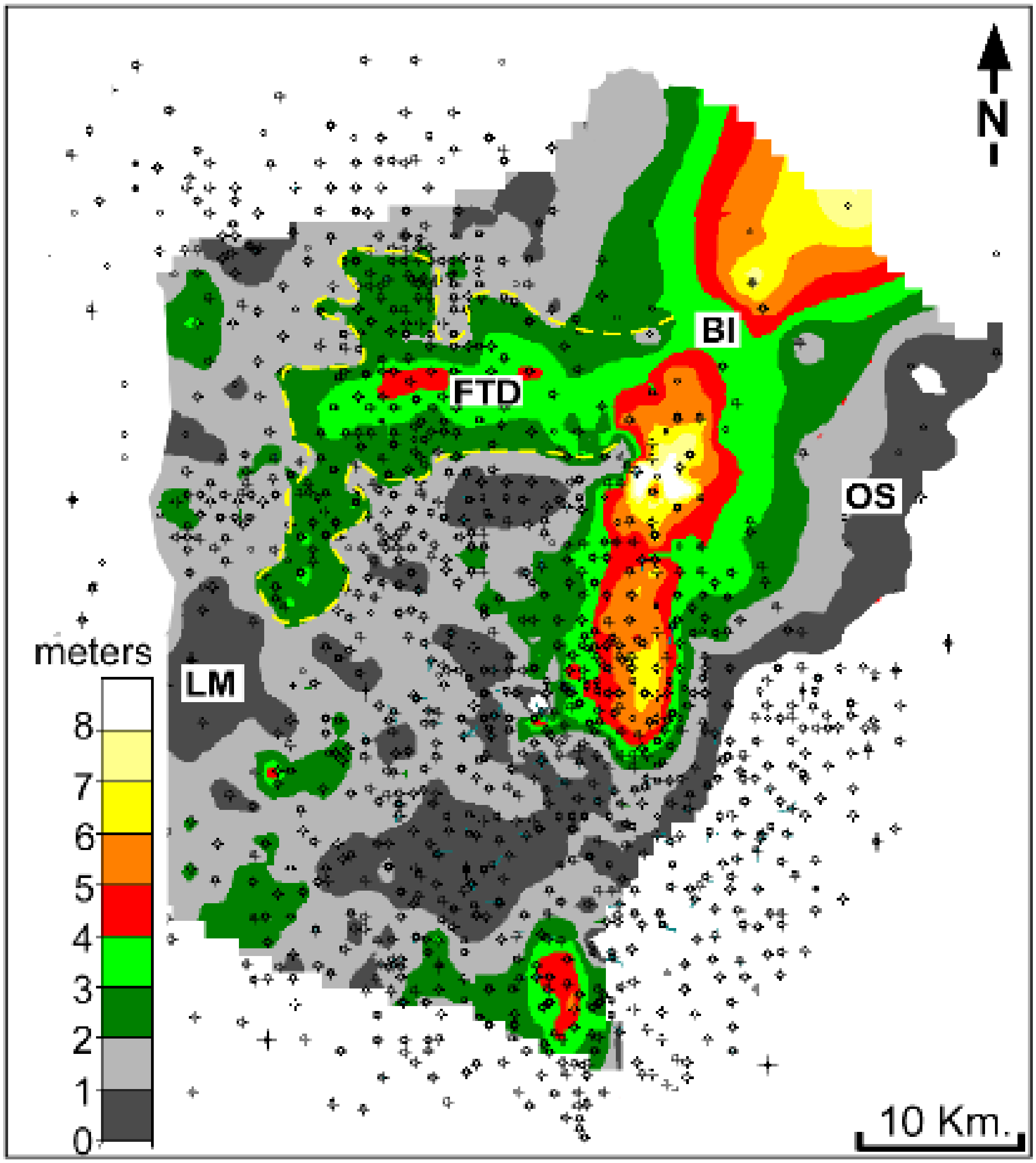

Enlarged Figure 5.13C. Sandstone thickness map of the Echo Springs 01 interval (ES01).

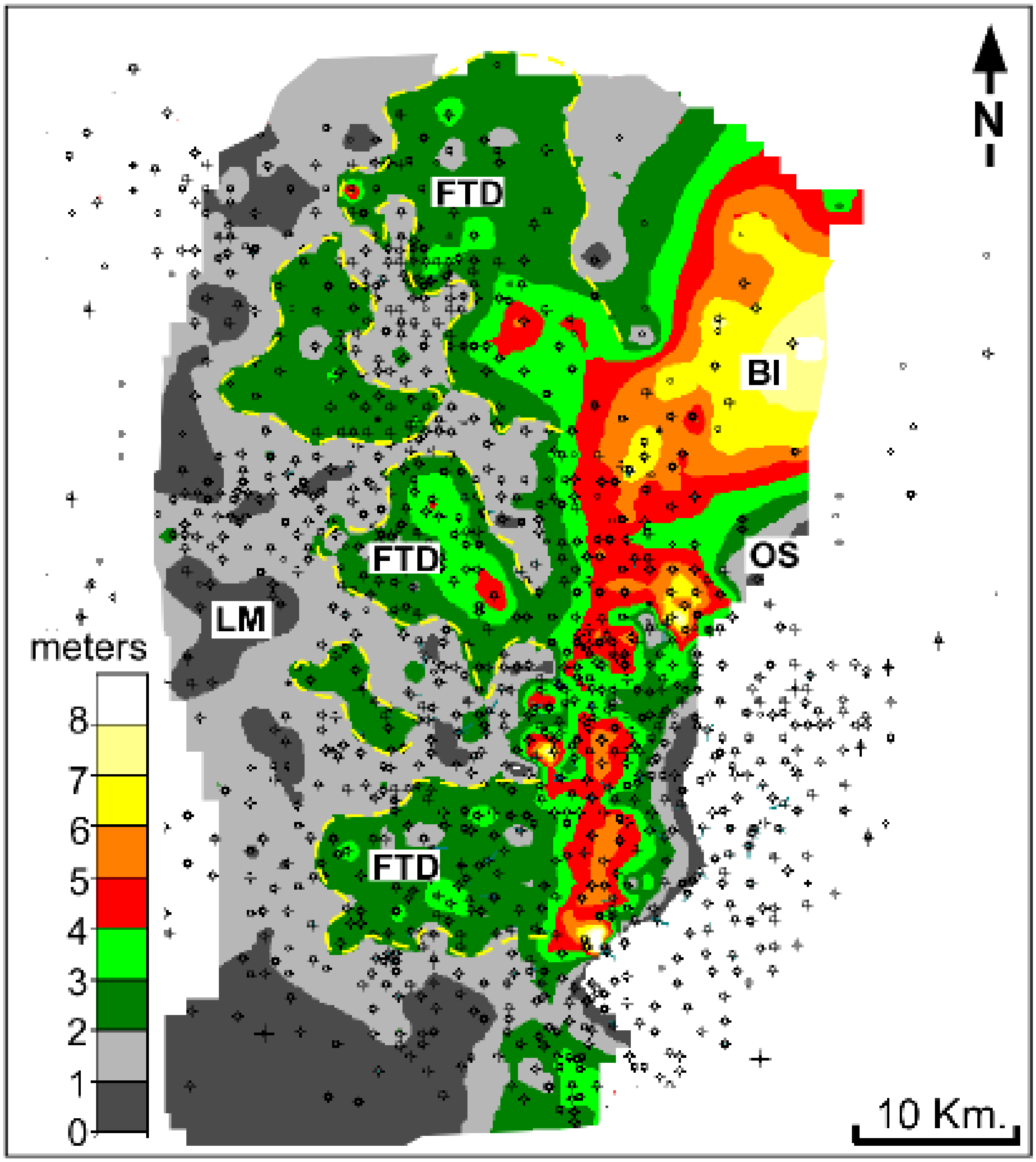

Enlarged Figure 5.13D. Sandstone thickness map of the Echo Springs 02 interval (ES02).

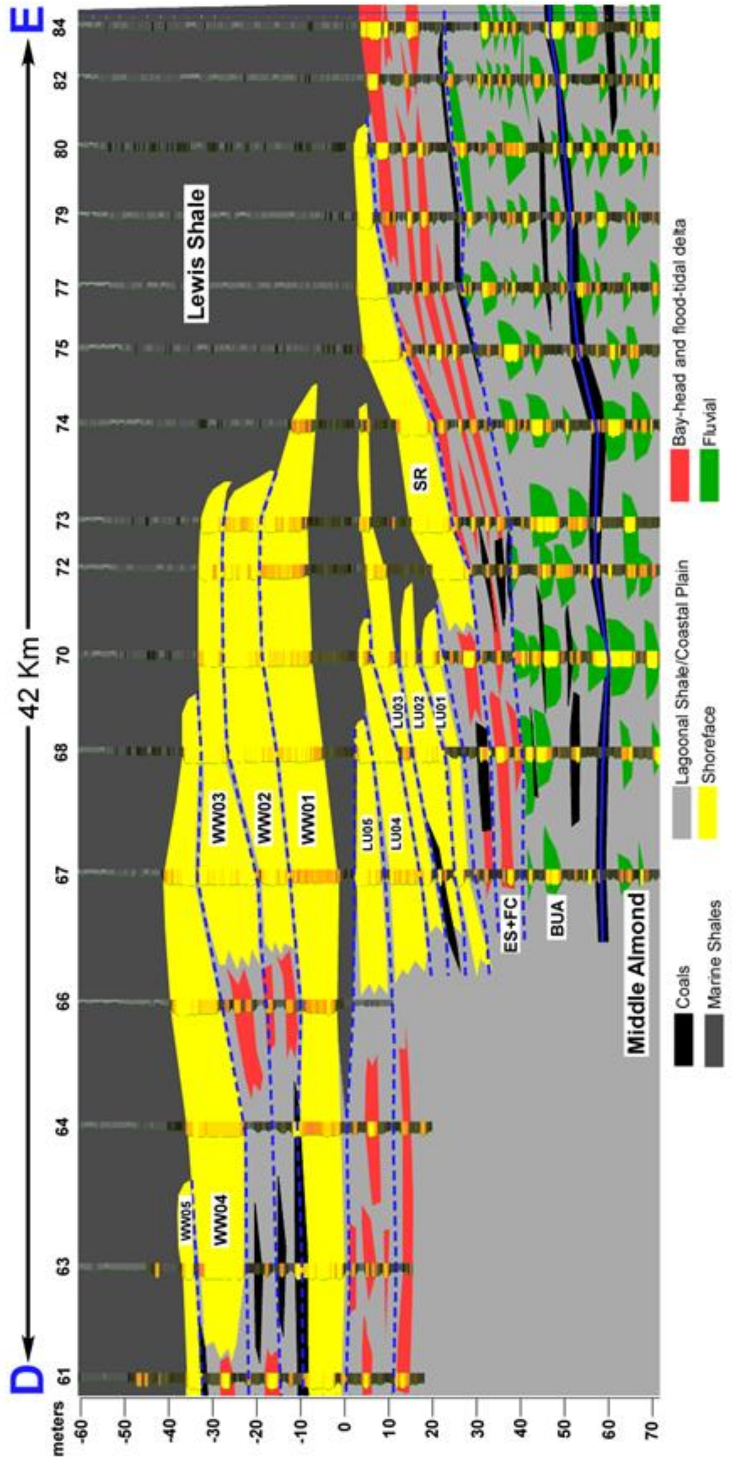

Enlarged Figure 5.14. Cross section including western sandbodies.

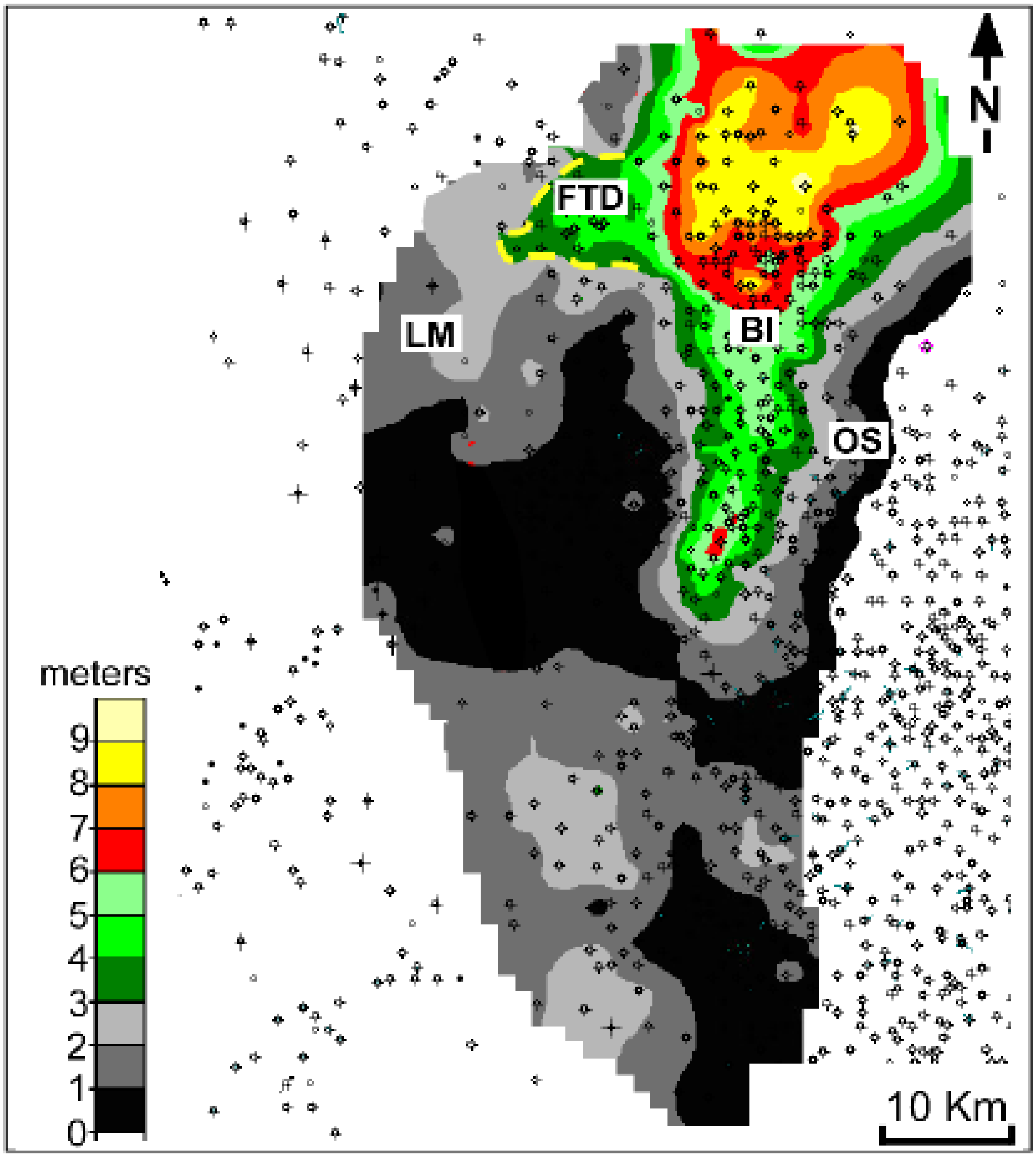

Enlarged Figure 5.15A. Sandstone thickness map of the Siberia Ridge 01 interval (SR01).

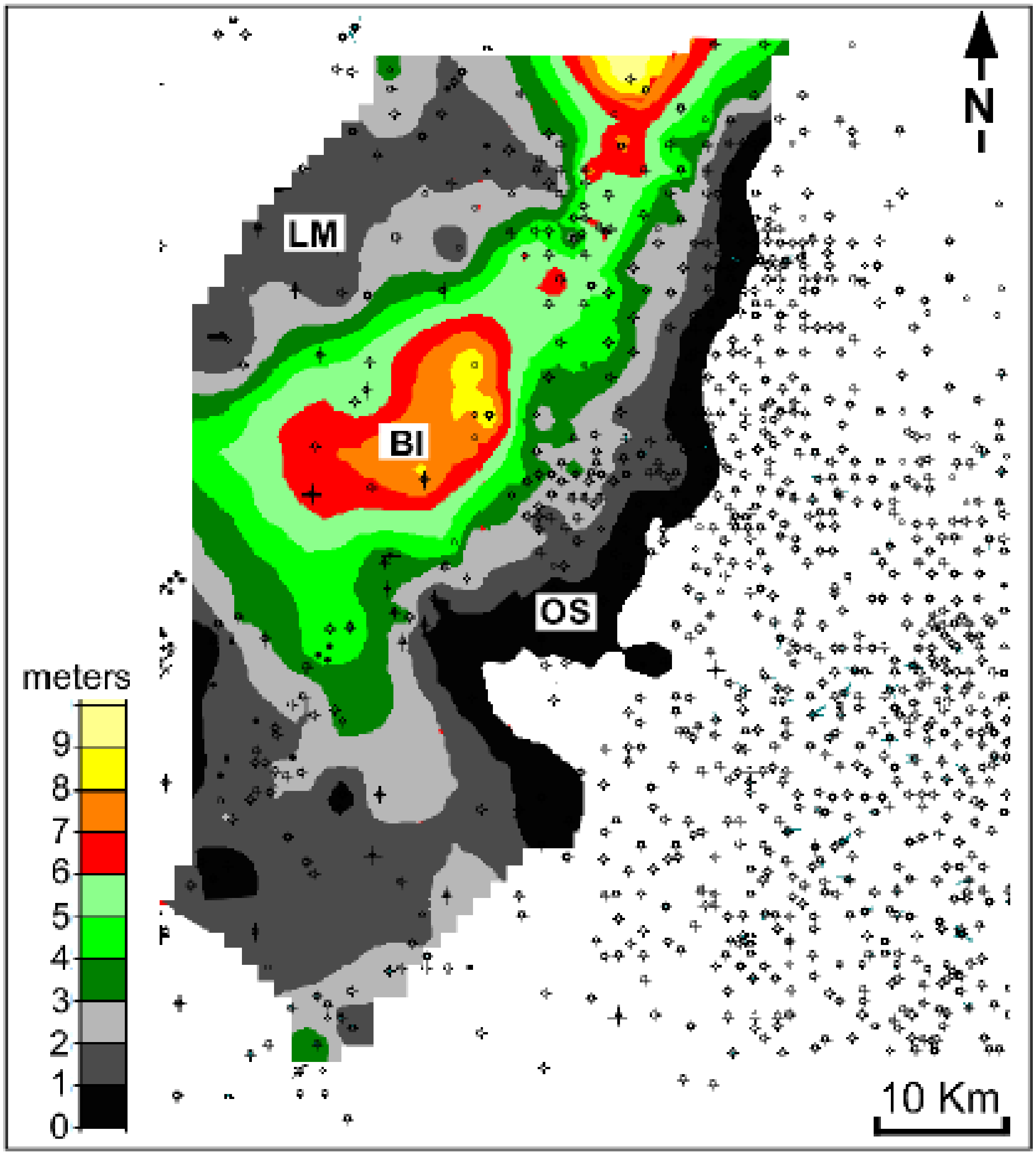

Enlarged Figure 5.15B. Sandstone thickness map of the Luman 02 interval (LU02).

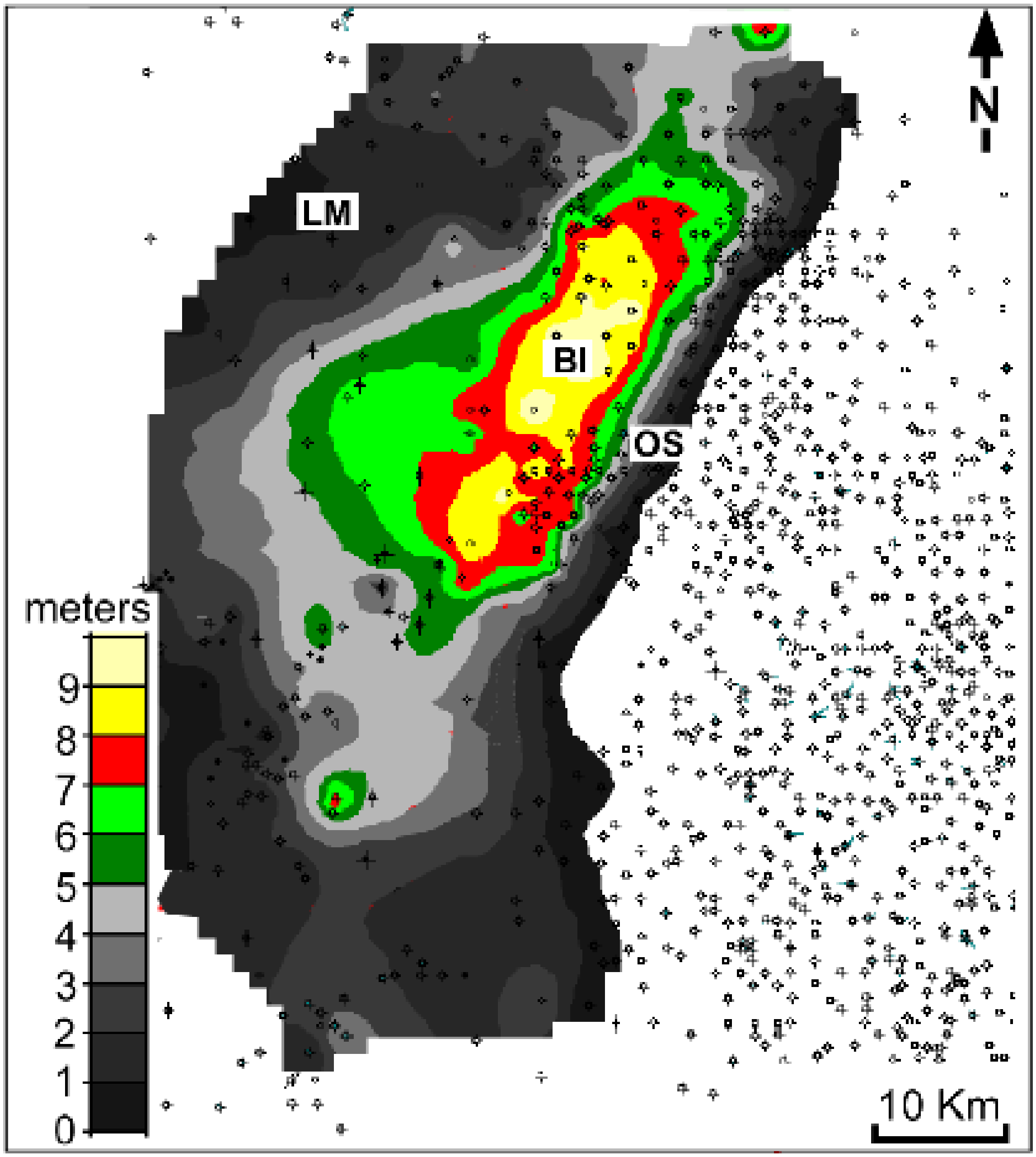

Enlarged Figure 5.15C. Sandstone thickness map of the Luman 03 interval (LU03).

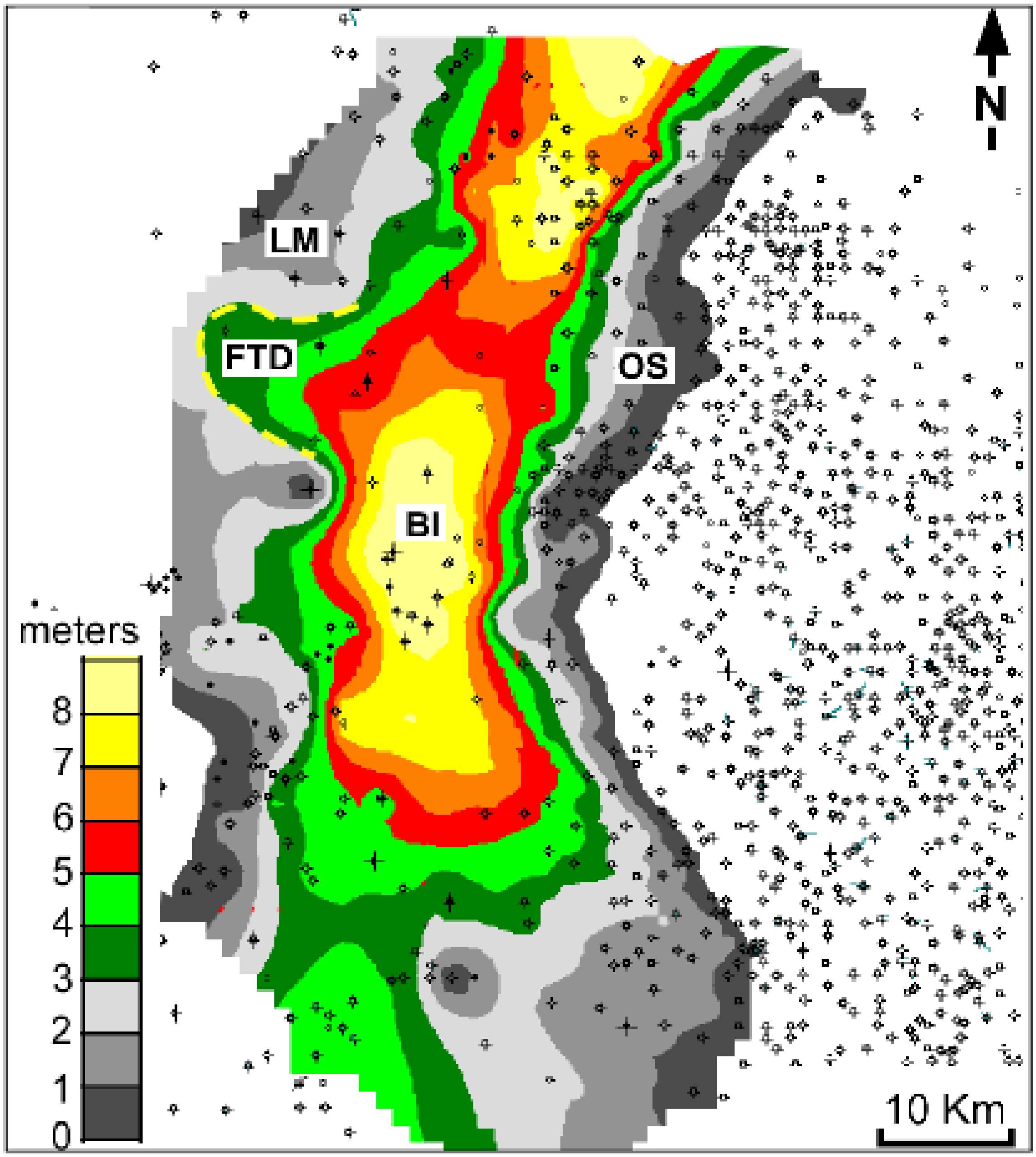

Enlarged Figure 5.15D. Sandstone thickness map of the Luman 04 interval (LU04).

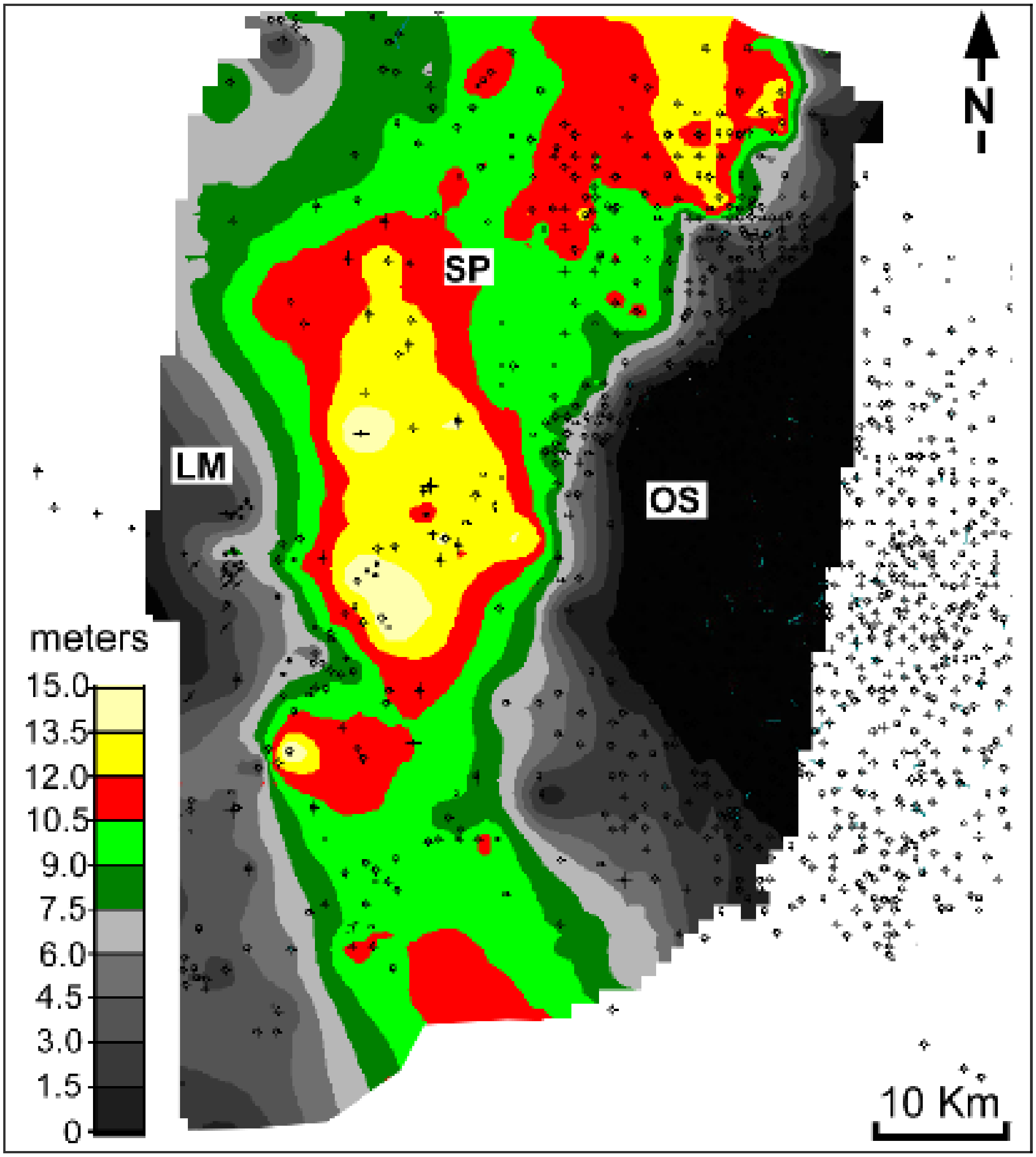

Enlarged Figure 5.16A. Sandstone thickness map of the West Wamsutter 01 interval (WW01).

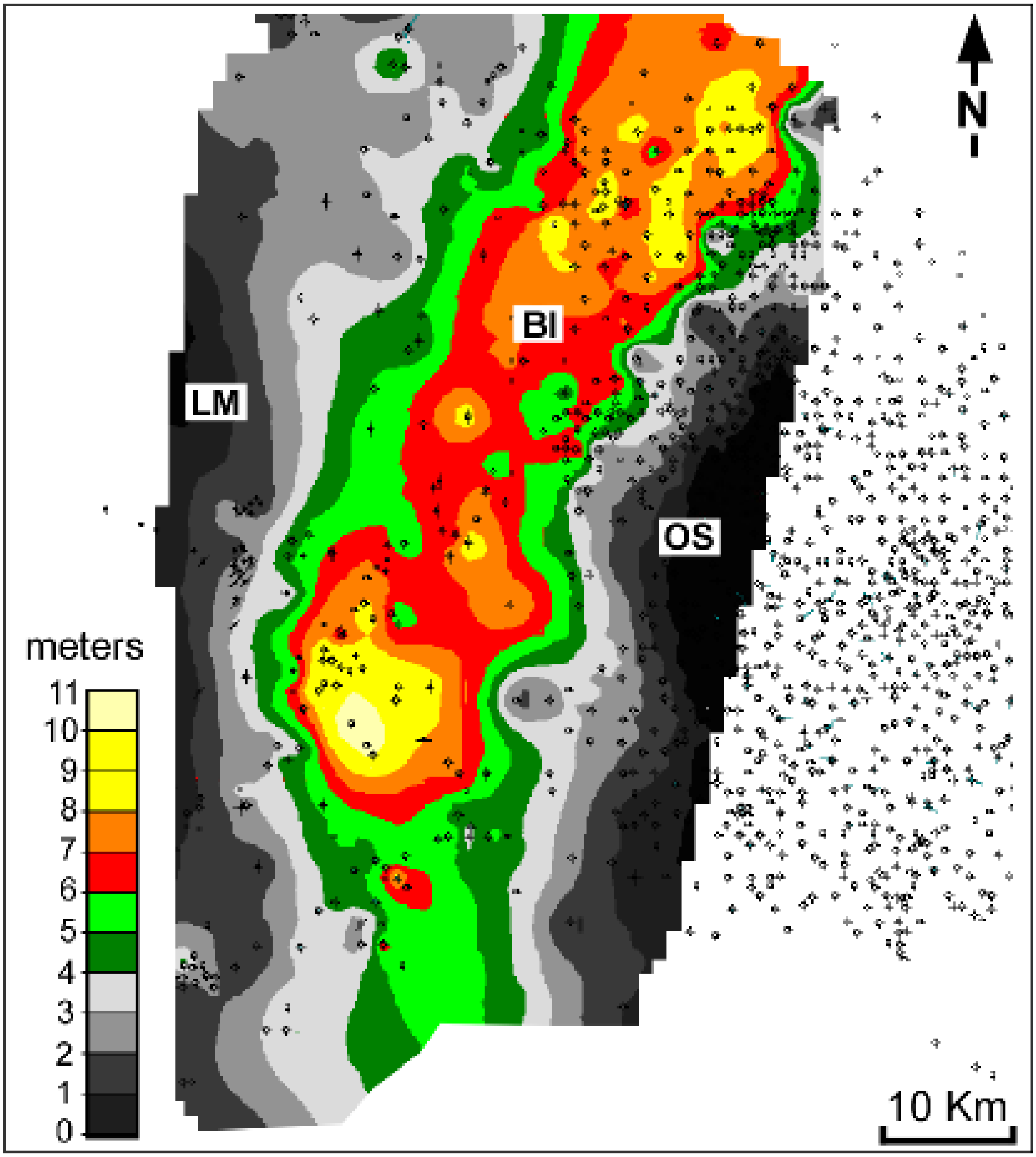

Enlarged Figure 5.16B. Sandstone thickness map of the West Wamsutter 02 interval (WW02).

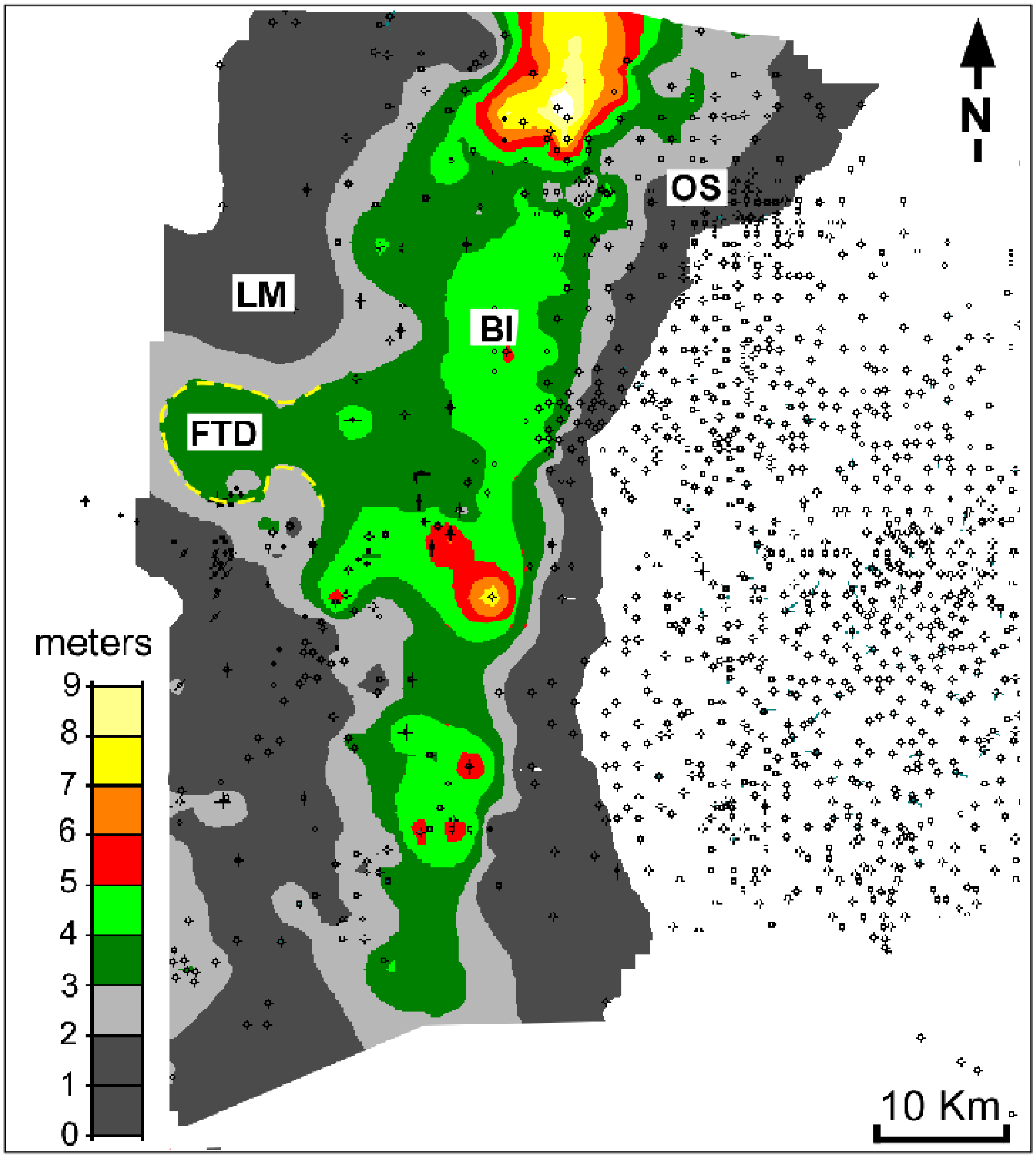

Enlarged Figure 5.16C. Sandstone thickness map of the West Wamsutter 03 interval (WW03).

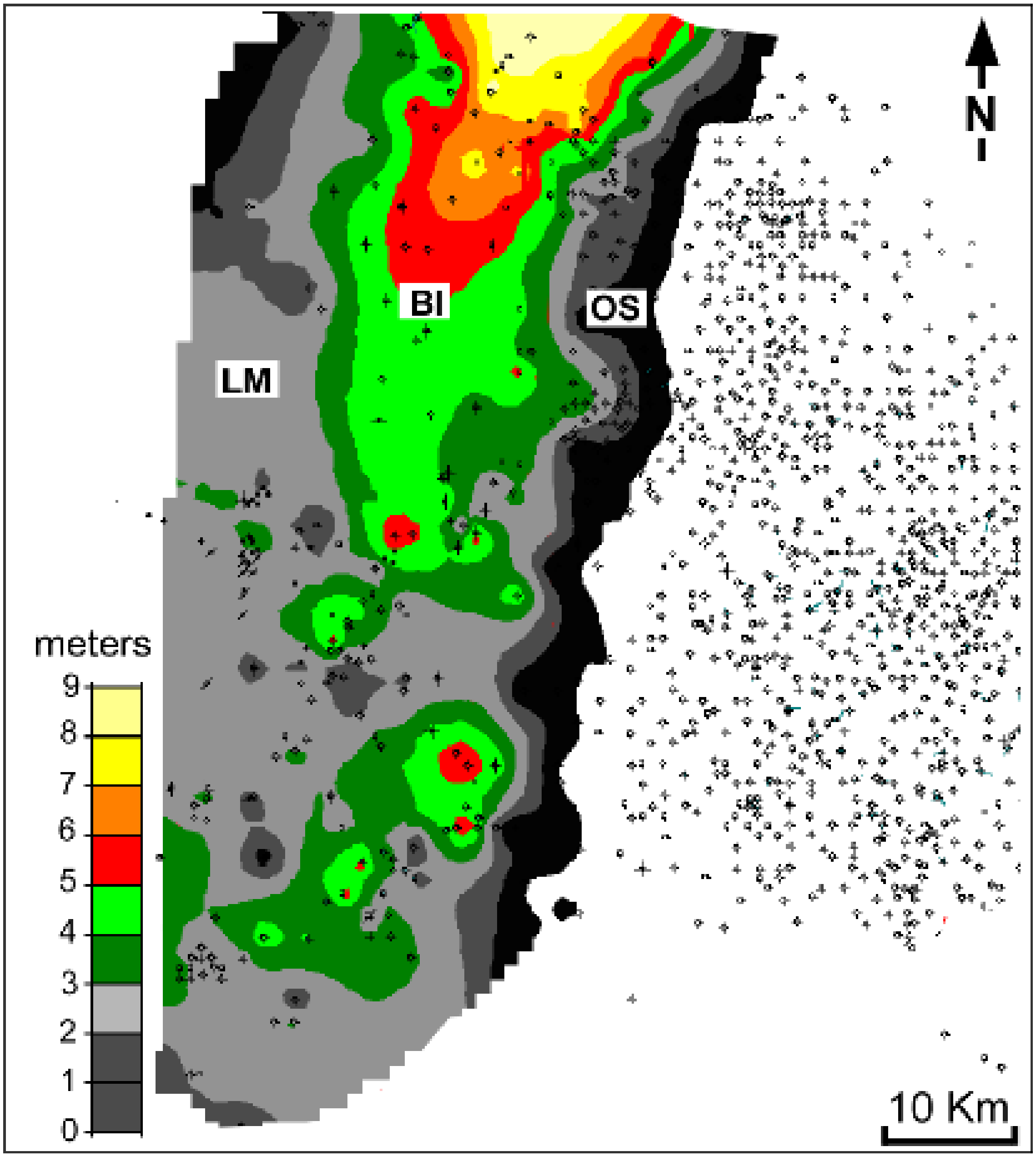

Enlarged Figure 5.16D. Sandstone thickness map of the West Wamsutter 04 interval (WW04).

# References

Adams, S., 2003, Modelling imbibition capillary pressure curves. Paper SPE-84298 presented at the SPE Annual technical Conference and Exhibition held in Denver, Colorado, USA, 5-8 October.

Ali, S. A., W. J. Clark, W. R. Moore and J. R. Dribus, 2010, Diagenesis and reservoir quality: Oilfield Review, 22, p. 14-27.

Amaefule, J.O., K. Wolfe, J. D. Walls, A. O. Ajufo, and E. Peterson, 1986, Laboratory determination of effective liquid permeability in low-quality reservoir rocks by the Pulse Decay Technique. Paper SPE 15149 presented at the SPE 56th California Regional Meeting, Oakland, California, 2-4 April, 1986. DOI: 10.2118/15149-MS.

Amaefule, J. O., M. Altunbay, D. Tiab, D. G. Kersey and D. K. Keelan, 1993, Enhanced reservoir description: using core and log data to identify hydraulic (flow) units and predict permeability in uncored intervals/wells: Presented at the SPE Annual Technical Conference and Exhibition.

Archie, G. E., 1952, Classification of carbonate reservoir rocks and petrophysical considerations: AAPG Bulletin, vol. 36, no. 2, p. 218–298.

Armitage, P.J., R.H. Worden, D.R. Faulkner, A.C. Aplin, A.R. Butcher, and J. Iliffe, 2010. Diagenetic and sedimentary controls on porosity in Lower Carboniferous fine-grained lithologies, Krechba field, Algeria: A petrological study of a caprock to a carbon capture site. Marine and Petroleum Geology, 27, p. 1395-1410.

Armitage, P.J., R.H. Worden, D.R. Faulkner, A.C. Aplin, A.R. Butcher, A.A. Espie, 2013. Mercia Mudstone Formation caprock to carbon capture and storage sites: petrology and petrophysical characteristics: Journal of the Geological Society, 170, p. 119–32.

Banfield, L.A., J. Vaitl, and W. A. Hill, 2008, The Wamsutter tight gas reservoir - the role of stratigraphy and sedimentology in a tight gas field study: Presented at the AAPG Rocky Mountain Section in Denver.

Beard, D.C., and P.K. Weyl, 1973, Influence of texture on porosity and permeability of unconsolidated sand: AAPG Bulletin 57, p. 349-369.

Beaumont, E. C., J. W. Shomaker and F. E. Kottlowski, 1971, Stratidynamics of coal deposition in southern Rocky mountain region, U. S. A., in Shomaker, J. W., Beaumont, E. C., and Kottlowski, E. F., eds., Strippable Low-Sulfur Coal Resources of the San Juan Basin in New Mexico and Colorado: New Mexico Bureau of Mines and Mineral Resources Memoir 25, p. 175-185.

Berg, R. R., 1986, Reservoir sandstones: Prentice-Hall Inc., New Jersey, p. 1-481.

Bloch, S., R. H. Lander and L. Bonnell, 2002, Anomalously high porosity and permeability in deeply buried sandstone reservoirs: origin and predictability: AAPG Bulletin 86, p. 301-328.

Blomenkamp, K., K. Burns, A. Duncan, and J. Hustedt, 2007, Structural and stratigraphic image interpretation of Mesaverde and Lewis Formations (Greater Green River Basin): Internal BP report.

Brake, A.C., 2013, Fracture optimization in a giant gas field, Wamsutter, Wyoming, USA. SPE 164029, SPE Middle East Unconventional Gas Conference and Exhibition. January 28-30, 2013, Muscat, Sultanate of Oman.

Brooks, R. M. and A. T. Corey, 1964, Hydraulic properties of porous media. Hydraulic Paper (3). Colorado State University, Fort Collins, Colorado, p. 1-30.

Bruun, P., 1962. Sea level rise as a cause of shore erosion. Journal of Waterways Harbour Division, American Society of Civil Engineers, Proceedings 88, p. 117–130.

Cadwallader, S., J. Wampler, T. Sun, H. Sebastian, M. Graff, I. Gil, H. Patel, G. D. Merletti, D. Spain, T. Lowrey, R. Miller, J. Hadden, and J. Swanson, 2015, An integrated dataset centered around distributed fiber optic monitoring — Key to the successful implementation of a geo-engineered completion optimization program in the Eagle Ford shale: Presented at the SPE Middle East Unconventional Gas Conference and Exhibition.

Carvajal, C. and R. Steel, 2012, Source-to-Sink Sediment Volumes within a Tectono-Stratigraphic Model for a Laramide Shelf-to-Deep-Water Basin: Methods and Results. Tectonics of Sedimentary Basins: Recent Advances, p. 131-151.

Cattaneo, A. and R. J. Steel, 2002, Transgressive deposits: a review of their variability. ELSEVIER paper. Earth-Science Reviews 62, p. 187 – 228.

Chierici, G.L., G. M. Ciucci, F. Eva, and G. Long, 1967, Effect of the overburden pressure on some petrophysical parameters of reservoir rocks. Proc. 7th World Petroleum Conference, Mexico City, p. 360-366.

Clavier, C., G. Coates, and J. Dumanoir, 1977, Theoretical and experimental bases for the Dual Water Model for interpretation of shaly sands, Paper SPE 6859, in 52nd Annual Technical Conference and Exhibition: Society of Professional Engineers.

Clifton, H. E., 2006, A Reexamination of Facies Models for Clastic Shorelines. SEPM (Society for Sedimentary Geology), ISBN 1-56576-121-9, p. 293–337.

Collison, J. D., 1969, The sedimentology of the Grindslow Shales and the Kinderscout Grit: a deltaic complex in the Namurian of northern England: Journal of Sedimentary Petrology, 39, p. 194-221.

Cross, T. A., 2012, Controls on coal distribution in transgressive-regressive cycles, Upper Cretaceous, Western Interior, U.S.A. In: Sea-Level Changes – An Integrated Approach, SEPM Special Publication No42, p. 371-380.

Dacy, J. M., 2010, Core tests for relative permeability of unconventional gas reservoirs. Paper SPE-135427 presented at the SPE Annual Technical Conference and Exhibition held in Florence, Italy, 19-22 September.

Dalrymple, R. W., B. A. Zaitlin and R. Boyd, 1992, Estuarine facies models: conceptual basis and stratigraphic implications. Journal of Sedimentary Petrology 62, p. 1130-1146.

Dawson, W.J., G. D. Merletti, D. R. Spain, A. Zett, R. Clark, J. Hamman, 2015, Integration of post-frac production logging data with pre-frac static petrophysical description enhances reservoir characterization: Presented at the SPWLA 56th Annual Symposium.

Dean E. E. and D. D. Stark, 1920, A convenient method for the determination of water in petroleum and other organic emulsions. The Journal of Industrial & Engineering Chemistry, 12(5), p. 486-490.

de Raaf, J. F. M., H. G. Reading and R. G. Walker, 1965, Cyclic sedimentation in the Upper Carboniferous of North Devon, England: Sedimentology, 4, p. 1-52.

Devine, P.E., 1991. Transgressive origin of channeled estuarine deposits in the Point Lookout Sandstone, Northwestern New Mexico: a Model for Upper Cretaceous, cyclic regressive parasequences of the U.S. Western Interior. American Association of Petroleum Geologists Bulletin 75, p. 1039– 1063.

Devlin, W.J., K.W. Rudolph, C.A. Shaw, and K.D. Ehman, 1993, The effect of tectonic and eustatic cycles on accommodation and sequence stratigraphic framework in the Upper Cretaceous foreland basin of southwestern Wyoming, in H.W. Posamentier, C.P. Summerhayes, B.U. Haq, and G.P. Allen, eds., Sequence stratigraphy and facies associations: International Association of Sedimentologists Special Publication 18, Boston, Blackwell Scientific Publications, p. 501–520.

Dickinson, W. R., M. A. Klute, M. J. Hayes, S. U. Janecke, E. R. Lundin, M. A. McKittrick and M. D. Olivares, 1988, Paleogeographic and paleotectonic setting of Laramie sedimentary basins in the central Rocky Mountain region. Geological Society of America Bulletin (7), p. 1013-1039.

Erslev, E. A., 1993, Thrusts, Back-Thrusts, and Detachment of Rocky Mountain Foreland Arches, in C. J. Schmidt, R. B. Chase, and E. A. Erslev, eds., Laramide Basement Deformation in the Rocky Mountain Foreland of the Western United States: Geological Society of America Special Paper 280, p. 339–358.

Fassett, J. E. and J. S. Hinds, 1971, Geology and fuel resources of the Fruitland Formation and Kirtland Shale of the San Juan Basin, New Mexico and Colorado: U. S. Geological Survey Professional Paper 676, 76p.

Fisher, W. L. and L. F. Jr. Brown, 1984, Clastic depositional system - a genetic approach to facies analysis: Bureau of Economic Geology, The University of Texas at Austin.

Flores, R.M., 1978, Barrier and Back-Barrier Environments of Deposition of the Upper Cretaceous Almond Formation, Rock Springs Uplift, Wyoming: The Mountain Geologist, v. 25, p. 57–65.

Flores, R. M., 2003, Paleocene Paleogeographic, Paleotectonic, and Paleoclimatic Patterns of the Northern Rocky Mountains and Great Plains Region, in R. G. Raynolds and R. M. Flores, eds., Cenozoic systems of the Rocky Mountain Region: Denver Colorado, Rocky Mountain Section SEPM, p. 63–106.

Gilbert, G.K., 1885. The topographic features of lake shores. United States Geological Survey Annual Report, p. 69– 123.

Gill, J. R., E. A. Merewether and W. A. Cobban, 1970, Stratigraphy and nomenclature of some Upper Cretaceous and Lower Tertiary rocks in South-Central Wyoming. Geological Survey Professional Paper 667.

Gill, J. R. and W. A. Cobbam, 1973, Stratigraphy and geologic history of the Montana Group and equivalent rocks, Montana, Wyoming, and North and South Dakota. Professional Paper, 37. Washington, DC, U.S. Geological Survey.

Gradstein, F. M., J. G. Ogg, M. Schmitz and G. Ogg, 2012, The Geologic Time Scale 2012. Published by Elsevier B.V.

Gunter, G.W., J. M. Finneran, D. J. Hartmann, and J. D. Miller, 1997, Early determination of reservoir flow units using an integrated petrophysical method. SPE 38679, Society of Petroleum Engineers.

Gunter, G. W., D. R. Spain, E. J. Viro, J. B. Thomas, G. Potter, and J. Williams, 2014, Winland pore throat prediction method – a proper retrospect: new examples from carbonates and complex systems: Presented at the SPWLA 55th Annual Logging Symposium.

Hartmann, D. J. and E. A. Beaumont, 1999, Predicting reservoir system quality and performance, in Exploring for Oil and Gas Traps, Edward A. Beaumont and Norman H. Foster, eds., Treatise of Petroleum Geology, Handbook of Petroleum Geology.

Helland-Hansen, W. and O. J. Martinsen, 1996, Shoreline trajectories and sequences: description of variable depositional-dip scenarios. Journal of Sedimentary Research 66, p. 670-688.

Hendricks, M. L., 1983, Depositional environments of the Rock Springs Formation, East Flank Rock Springs Uplift, Sweetwater County, Wyoming: unpub. doctoral thesis, Colorado School of Mines, 213p.

Hendricks, M., 2009, Ravinement surface control on hydrocarbon accumulation in transgressive systems tracks: Almond Formation, Green River Basin, Wyoming. Unconformity Controls 1994 Symposium, The Rocky Mountain Association of Geologists.

Heward, A.P., 1981. A Review of wave-dominated clastic shoreline deposits. Earth-Science Reviews 17, p. 223– 276.

Holditch, S.A., 2006, Tight gas sands: Journal of Petroleum Technology, 58, p. 86-93.

Horn, B.W. and R. A. Schrooten, 2005, Development of the Echo Spring-Standard Draw Field Area: using technology to enhance an infill program, Washakie Basin, Wyoming: Gas in the Rockies, D. Anderson et al., eds. Denver, Colo.: Rocky Mountain Association of Geologists.

Jacka, A.D., 1965, Depositional Dynamics of the Almond Formation, Rock Springs Uplift, Wyoming: Wyoming Geological Association, 19th Field Conference Guidebook, p. 81–100.

Jackson, R. G. II, 1976, Depositional model of point bars in the lower Wabash River: Journal of Sedimentary Geology, 46, p. 579-594.

Jackson, S.R. and V. Rawn-Schatzinger, 1993, Data from selected Almond Formation Outcrops, Sweetwater County Wyoming: Topical Report, U.S. Department of Energy, 76 p.

Jennings, H.Y., Jr. and G. H. Newman, 1971, The effect of temperature and pressure on the interfacial tension of water against methane-normal decane mixtures, Soc. Pet. Eng. J. (June 1971), p. 171-175.

Jerauld, G. R., 1996. Gas-Oil relative Permeability of Prudhoe Bay. Paper SPE-35718 presented at the Western Regional Meeting, Anchorage, Alaska, 22-24 May. DOI:10.2118/35718-MS.

Johnson, D.W., 1919. Shore Processes and Shoreline Development. Wiley, New York. 584 p.

Juhasz, I., 1979. The central role of Qv and formation-water salinity in the evaluation of shaly formations. Paper presented at the SPWLA Twentieth Annual Logging Symposium, June 3-6.

Kieft, R. L., G.J .Hampson, C. A. Jackson and E. Larsen, 2011, Stratigraphic architecture of a net-transgressive marginal- to shallow-marine succession: Upper Almond Formation, Rock Springs Uplift, Wyoming, U.S.A.: Journal of Sedimentary Research 81, p. 513-533.

Kolodzie, S.J., 1980, Analysis of pore throat size and use of Waxman-Smits Equation to determine OOIP in Spindle Field, Colorado: Presented at SPE 55th Annual Fall Technical Conference and Exhibition.

Krystinik, L.F. and B. B. Dejarnett, 1995, Lateral Variability of Sequence Stratigraphic Framework in the Campanian and Early Maastrichtian of the Western Interior Seaway, in Van Wagoner, J.C., and Bertram, G.T., eds., Sequence Stratigraphy of Foreland Basin Deposits: Outcrop and Subsurface Examples from the Cretaceous of North America: American Association of Petroleum Geologists, Memoir 64, pp. 11–26.

Lageson, D. R., and J. G. Schmitt, 1994, The Sevier Orogenic Belt of the Western United States: Recent Advances in Understanding its Structural and Sedimentologic Framework, in M.V.Caputo, J. A. Peterson, and K. J. Franczyk, eds., Mesozoic systems of the Rocky Mountain Region: Denver, Colorado, Rocky Mountain Section SEPM, p. 27–64.

Land, C. S., 1968. Calculation of imbibition relative permeability for two- and three-phase flow from rock properties. SPE J. 8 (2): 146-156, Trans., AIME, 243. SPE-1942-PA. DOI:10.2118/1942-PA.

Larionov, V. V., 1969, Radiometry of boreholes (in Russian). Nedra, Moscow.

Lawrence, J. R., 2007, Depositional environment of the Upper Almond Formation in the Great Divide and Washakie basins, south-central Wyoming (Master's thesis). Faculty of the Department of Geosciences, University of Houston, 54p.

Lewis, J. L., 1961, The stratigraphy and depositional history of the Almond formation in the Great Divide basin, Sweetwater County, Wyoming: 16th Annual Field Conference Guidebook, p. 87-95.

Lieber, R. and M. Miller, 2009, The Wamsutter tight gas reservoir – making an unconventional reservoir conventional. Presented at the SPWLA 50th Annual Logging Symposium.

Liu, S. F., D. Nummedal, P. G. Yin and H. J. Luo, 2005, Linkage of Sevier thrusting episodes and Late Cretaceous foreland basin megasequences across southern Wyoming (USA). Basin Res 17, p. 487-506.

Martin, P. and J. Dacy, 2004, Effective Qv by NMR core tests, Paper HH, in 45th Annual Logging Symposium Transactions: Society of Professional Well Log Analysts.

Martinsen, R. S. and G. Christensen, 1992, A stratigraphic and environmental study of the Almond Formation, Mesaverde Group, Greater Green River Basin, Wyoming: 43rd Annual Field Conference Guidebook, p. 171-190.

Martinsen, O. J., R. S. Martinsen and J. R. Steidtmann, 1993, Mesaverde Group (Upper Cretaceous), southern Wyoming; allostratigraphy versus sequence stratigraphy in a tectonically active area: AAPG Bulletin 77, p. 1351-1373.

Martinsen, R. S., G. E. Christensen and M. A. Olsen, 1995, Stratigraphy and Lithofacies of the Almond Formation, Washakie and Great Divide Basins, Wyoming: Wyoming Geological Association Field Conference Guidebook, v. 1995, p. 297-310.

Martinsen, R. S., 2003, Syn-sedimentary tectonic and sediment supply influences on basin physiography and depositional regime of the western interior Cretaceous

Seaway, Wyoming. AAPG Search and Discovery Article #90013, AAPG annual meeting, Salt lake City, 2003.

McCabe, P. J. and J. T. Parish, 1992, Tectonic and climatic controls on the distribution and quality of Cretaceous coals. In: McCabe, P. J. & Parrish, J. T., (eds) Controls on the Distribution and Quality of Cretaceous Coals. Geological Society of America, Special Paper 267, p. 1-15.

McCubbin, D.G. and M. J. Brady, 1969, Depositional Environments of the Almond Reservoirs, Patrick Draw Field, Wyoming: The Mountain Geologist, v. 6, p. 3–26.

Merletti, G. D., R. A. Pour, and D. R. Spain, 2013, Calibration of static reservoir models with dynamic data for efficient tight-gas development (Wyoming, US). Paper SPE-164031MS presented at the SPE Middle East Unconventional Gas Conference and Exhibition held in Muscat, Oman, 28-30 January.

Merletti, G. D., D. R. Spain, R. Abdollah-Pour and A. Zett, 2014, Understanding depositional and diagenetic processes improve petrophysical rock typing workflows in tight gas reservoirs: Presented at the SPWLA 55th Annual Logging Symposium.

Merletti, G. M., P. Gramin, S. Salunke, J. Hamman, D. R. Spain, V. Shabro, P. Armitage, C. Torres-Verdin, G. Salter and J. Dacy, 2016, How pre-scale attributes may be used to derive robust drainage and imbibition water saturation models in complex tight-gas reservoirs. Petrophysics, Vol. 57, No 5, 18p.

Merletti, G. D., D. R. Spain, J. J. Melick, P. Armitage, J. Hamman, V. Shabro and P. Gramin, 2017, Integration of depositional, petrophysical and petrographic facies for predicting permeability in tight gas reservoirs. Interpretation, Vol. 5, No 2 (May 2017); p. 29-41.

Miall, A. D., 1985, Architectural-element analysis: a new method of facies analysis applied to fluvial deposits: Earth-Science Reviews, 22, p. 261-308.

Middleton, G. V., 1978, Facies, in Fairbridge, R. W. and Bourgeois, J., eds., Encyclopedia of sedimentology: Strousburg, Pennsylvania, Dowden, Hutchinson and Ross, p. 323-325.

Miller M. and K. Shanley, 2010, Petrophysics in tight gas reservoirs – key challenges still remain. The Leading Edge, Vol. 29, No. 12, p. 1464-1469.

Molenaar, C.M., 1983, Major depositional cycles and regional correlations of Upper Cretaceous rocks, Southern Colorado Plateau and Adjacent Areas, in Reynolds, M.W., and Dolly, E.D., eds., Palaeogeography of West-Central United States: SEPM, Rocky Mountain Section, p. 201–223.

Montgomery, S. L., 1996, Brady Unit, Rock Springs Uplift, Wyoming: Migration and Structural History: AAPG Bulletin, v. 80, no. 10, p. 1535–1546.

Morgan, P., 2003, Colorado Plateau and southern Rocky Mountains Uplift and Erosion, in R. G. Raynolds and R. M. Flores, eds., Cenozoic systems of the Rocky Mountain Region: Denver Colorado, Rocky Mountain SEPM, p. 1–31.

Newsham, K. E and J. A. Rushing, 2001, An integrated work-flow process to characterize unconventional gas resources: part geological assessment and petrophysical evaluation: Presented at the SPE Annual Technical Conference and Exhibition.

Nummedal, D. and D. J. P. Swift, 1987, Transgressive stratigraphy at sequence-bounding unconformities: some principles derived from Holocene and Cretaceous example. In: Nummedal, D., Pilkey, O. H., Howard, S. D. (Eds.), Sea Level Fluctuation and Coastal Evolution. SEPM Special Publication, vol. 41, p. 241-260.

Osaba, J.S., Richardson, J.G., Kerver, J.G., Hafford, J.K., and Blair, P.M., 1951, Laboratory measurements of relative permeability. Trans., AIME 192, p. 47-56.

Otteman, A. S., and A. W. Snoke, 2005, Structural Analysis of a Laramide, Basement-Involved, Foreland Fault Zone, Rawlins Uplift, South-Central Wyoming: Rocky Mountain Geology, v. 40, no. 1, p. 65–89, doi:10.2113/40.1.65.

Pickell, J.J., B.F. Swanson, and W.B. Hickman, 1966, Application of air-mercury and oil-air capillary pressure data in the study of pore structure and fluid distribution. SPE J. 6 (1), p. 55-61. SPE-1227-PA. DOI10.2118/1227-PA.

Pittman, E.D. 1992. Relationship of porosity and permeability to various parameters derived from mercury injection capillary pressure curves for sandstones: AAPG Bulletin Vol. 76, No. 2, p. 191-198.

Quest, M. and M. M. Gatling, 2007, Advanced core analysis study in Sweetwater County, Wyoming. BP Internal Report (unpublished).

Reading, H. G., 1986, Sedimentary environment and facies. Oxford, Blackwell Scientific, 2nd edition, 704p.

Rigg, N. M., 2009, Regional mapping of genetic intervals in the Almond Formation, Greater Wasmutter Field, Southwest Wyoming: an iterative geostatistical approach to high-grading well locations and implications for reserves bookings: Search and Discovery Article #120016.

Roehler, H. W., 1988, The Pintail Coal Bed and Barrier Bar G – A model for coal of barrier bar-lagoon origin, Upper Cretaceous Almond Formation, Rock Springs Coal Field, Wyoming: U.S. Geological Survey Professional Paper 1398.

Roehler, H. W., 1990, Stratigraphy of the Mesaverde Group in the central and eastern Greater Green River basin, Wyoming, Colorado and Utah: U.S. Geological Survey Professional Paper 1508.

Rushing, J. A. and K.E. Newsham, 2001, An integrated work-flow process to characterize unconventional gas resources: part formation evaluation and reservoir modeling: Presented at the SPE Annual Technical Conference and Exhibition.

Rushing, J. A., K.E. Newsham, and T.A. Blasingame, 2008, Rock typing - keys to understanding productivity in tight gas sands: Presented at the SPE Unconventional Reservoirs Conference.

Rushing, J.A., Newsham, K.E., Van Fraassen, K.C., 2008. Laboratory Measurements of Gas-Water Interfacial Tension at HP/HT Reservoir Conditions. Paper SPE-114516 presented at the CIPC/SPE Gas Technology Symposium in Calgary, Alberta, Canada, 16-19 June.

Ryer, T. A., 1981, Deltaic coals of Ferron Sandstone member of Mancos Shale: Predictive model for Cretaceous coal-bearing strata of Western Interior: American Association of Petroleum Geologist Bulletin, v. 65, p. 2323-2340.

Ryer, T. A., 1984, Transgressive-regressive cycles and the occurrence of coal in some Upper Cretaceous strata of Utah, U. S. A., in Rahmani, R. A., and Flores, R. M., eds., Sedimentology of Coal-Bearing Sequences: International Association of Sedimentologists Special Publication 7: Blackwell Scientific Publications, Oxford, p. 217-227.

Sageman, B. B. and M. A. Arthur, 1994, Early Turonian paleogeographic/paleobathymetric map, Western Interior, U.S.. Mesozoic Systems of the Rocky Mountains Region, USA (Eds. M. V. Caputo, J. A. Peterson and K. J. Franczyk), p. 14.

Sanders, J. E., 1963, Effect of Sea-Level Rise on Established Barrier (abs.): Geol. Soc. America. Spec. Paper 73, p. 231.

Sanders, J. E. and N. Kumar, 1975, Evidence of shoreface retreat and in-place “drowning” during Holocene submergence of barrier, shelf off Fire Island, New York, Geological Society of America Bulletin 86, p. 65-76.

Schatzinger, R.A. and L. Tomutsa, 1999, Multiscale heterogeneity characterisation of tidal channel, tidal delta and foreshore facies, Almond Formation Outcrops, Rock Springs Uplift, Wyoming, in Schatzinger, R.A., and Jordan, J.F., eds., Reservoir Characterisation: American Association of Petroleum Geologists, Memoir 71, p. 45–56.

Sears, J. D., C. B. Hunt, and T. A. Hendricks, 1941, Transgressive and regressive Cretaceous deposits in southern San Juan Basin, New Mexico. United States Geological Survey, 193-F.

Sebastian, H., I. Gil, M. Graff, J. Wampler, G. D. Merletti, T. Sun, S. Cadwallader, H. Patel, D. Spain, K. Cawiezel, P. Smith, and R. Keck, 2015, 3-D hydraulic fracturing and reservoir flow modeling — Key to the successful implementation of a geo-engineered completion optimization program in the Eagle Ford shale: Presented at the Unconventional Resources Technology Conference.

Seth, K., Beales, V., Kawasaki, A., and Namba, T., 2013. Saturation Height Function in a Field Under Imbibition: A Case Study. Paper SPE-165880 presented at the SPE Asia Pacific Oil & Gas Conference and Exhibition held in Jakarta, Indonesia, 22-24 October.

Sheldon, H.A., J. Wheeler, R.H. Worden, and M.J. Cheadle, 2003. An analysis of the roles of stress, temperature, and pH in chemical compaction of sandstones: Journal of Sedimentary Research 73, p. 64-71.

Smith, L. K., 1998, Formation water chemistry as a tool for studying compartmentalization: example from the Almond Formation. In Petrogenesis and Petrophysics of Selected Sandstone Reservoirs of the Rocky Mountain Region, ed. Roger M. Slatt. Proceedings of 1998 RMAG Symposium, p. 185-204.

Snedden, J.W. and Dalrymple, R.W., 1999. Modern shelf sand ridges: from historical perspective to a unified hydrodynamic and evolutionary model. In: Bergman, K.M.,

Snedden, J.W. (Eds.), Isolated Shallow Marine Sand Bodies: Sequence Stratigraphic Analysis and Sedimentological Interpretation. SEPM Special Publication, vol. 64, p. 13– 28.

Spain, D.R., Merletti, G.D., Webster, M., Kaye, L., 2013. The Importance of Saturation History to Tight Gas Deliverability. Paper SPE 163958-MS presented at the SPE Middle East Unconventional Gas Conference, Muscat, Oman, 29–30 January.

Spain, D. R., R. Naidu, W. Dawson, G. D. Merletti, R. Kumar and D. Y. Guo, 2015, Integrated workflow for selecting hydraulic fracture initiation points in the Khazzan giant tight gas field, Sultanate of Oman: Presented at the Abu Dhabi International Petroleum Exhibition and Conference.

Steel, R. J., Rasmussen, H., Eide, S., Neuman, B., Siggerud, E.I.H., 2000. Anatomy of High-Sediment-Supply, Transgressive Tracts in the Vilomara Composite Sequence, Sant Llorenc del Munt, Ebro basin, NE Spain. Sedimentary Geology 138, p. 125– 142.

Steel, R. J., P. Plink-Bjorklund and J. L. Aschoff, 2012, Tidal deposits of the Campanian Western Interior Seaway, Wyoming, Utah and Colorado, USA. In: Principles of Tidal Sedimentology (Eds R. A. Davis Jr and R. W. Dalrymple). Springer, The Netherlands, p. 437-471.

Stearns, D. W., W. R. Sacrison, and R. C. Hanson, 1975, Structural History of Southwestern Wyoming as Evidenced from Outcrop and Seismic, in D.W. Bolyard, ed., Deep Drilling Frontiers of the Central Rocky Mountains: Denver, Colorado, Rocky Mountain Association of Geologists, p. 9–20.

Straley, C., D. Rossini, H. Vinegar, P. Tutunjian, and C. Morris, 1994, Core analysis by low field NMR, paper SCA-9404, in Proceedings of the International Symposium of the Society of Core Analysts, p. 43–56.

Sturm, S. D, L. W. Evans, B. F. Keusch, and W. J. Clark, 2001, Almond Formation reservoir characterization and sweet spot analysis in Siberia Ridge Field, Wyoming. Gas in the Rockies. D. Anderson et al., eds. Denver, Colorado: Rocky Mountain Association of Geologists, p. 145-170.

Sun, T., C. Mardi, G. D. Merletti, H. Patel, S. Cadwallader, M. Graff, J. Wampler, I. Gil, H. Sebastian, D. R. Spain and O. Aguirre, 2015, Advanced petrophysical, geological, geophysical and geomechanical reservoir characterization – Key to the successful implementation of a geo-engineered completion optimization program in the Eagle Ford Shale: Presented at the Houston Geological Society Mudrock Conference.

Swift, D.J.P., 1968. Coastal erosion and transgressive stratigraphy. Journal of Geology 76, p. 444–456.

Thomeer, J. H. M., 1960. Introduction of a pore geometrical factor defined by the capillary pressure curve. Paper presented at 34th Annual Fall Meeting of SPE, October 4-7, 1959. AIME Technical Note 2057.

Tobin, R.C., T. McClain, R. B. Lieber, A. L. Ozkan, L. A. Banfield, A. M. Marchand and L. McRae, 2010, Reservoir quality modelling of tight-gas sands in Wamsutter Field: integration of diagenesis, petroleum systems and production data. AAPG Bulletin 94, p. 1229-1266.

Tye, R.S., J. S. Hewlett, P. R. Thompson, and D. K. Goodman, 1993, Integrated stratigraphic and depositional facies analysis of parasequences in a transgressive systems tract, San Joaquin Basin, California. In: Weimer, P., Posamentier, H.W. (Eds.), Siliciclastic Sequence Stratigraphy: Recent Developments and Applications. American Association of Petroleum Geologists Memoir, vol. 58, p. 99–133.

Van Horn, M.D., 1979. Stratigraphy of the Almond Formation, East-Central Flank of the Rock Springs Uplift, Sweetwater County, Wyoming: A Mesotidal Shoreline Model for the Late Cretaceous [M.S. Thesis]: Colorado School of Mines, 150 p.

VerPloeg, A. J., R. H. DeBruin, R. L. Oliver and M. Clark, 1983, Almond and Frontier tight gas sand cross sections, Greater Green River Basin, Wyoming. Geological Survey of Wyoming, Open File Report 83-S, 31p.

Weimer, R. J., 1960, Upper Cretaceous stratigraphy, Rocky Mountain area. American Association of Petroleum Geologists Bulletin, v.44, p.1-20.

Weimer, R.J., 1965, Stratigraphy and petroleum occurrences, Almond and Lewis Formations (Upper Cretaceous), Wamsutter Arch, Wyoming: Wyoming Geological Association, 19th Field Conference, Guidebook, p. 65–81.

Weimer, R.J., 1966, Time-stratigraphic analysis and petroleum accumulation, Patrick Draw Field, Wyoming: American Association of Petroleum Geologists, Bulletin, v. 50, p. 2150–2175.

Weimer, R. J., J. D. Howard and D. R. Lindsay, 1982, Tidal flats and associated tidal channels. In: Scholle, P. A. and Spearing, D. (eds) Sandstone Depositional Environments. American Association of Petroleum Geologists, Memoirs, 31, p. 191-245.

Winland, H. D., 1976, Unpublished Report: Evaluation of gas slippage and pore aperture size in carbonate and sandstone reservoirs: Amoco Production Company Research Department Report No. F76-G-5.

Worden, R. H. and Burley, S. D.: Sandstone Diagenesis: The Evolution of Sand to Stone, in Burley SD and Worden RH (eds): Sandstone Diagenesis: Recent and Ancient. Malden, Massachusetts, USA: Wiley-Blackwell Publishing, International Association of Sedimentologists Reprint Series, vol. 4 (2003), p. 3-44.

Zett, A., M. Webster, D. R. Spain, D. Surles and C. Colbert, 2012, Application of new generation multi detector pulsed neutron technology in petrophysical surveillance: Presented at SPWLA 53rd Annual Logging Symposium.

# Vita

German Diego Merletti was born in 1971, in the town of Cordoba (Argentina), as the first son of Mercedes Teresa Salvay and Jorge Alberto Merletti. German attended Elementary School at the “Juan Zorrilla de San Martin” and High School at the “Instituto Jose Pena”. German went on studying Geological Sciences at the National University of Cordoba. He covered a variety of petrophysical and geophysical roles with Repsol-YPF for 8 years in Argentina and the last 11 years with BP in Houston. German is a Field Study Petrophysicist and his current role with the Unconventional Reservoirs Technology team includes developing and implementing new workflows for characterizing tight-gas reservoirs in North America and the Middle East.

Permanent email address: gmerletti@hotmail.com
Permanent address: 13318 Story Glen Dr., Cypress, TX-77429
This dissertation was typed by German Diego Merletti.